Author:
Titheradge, Daniel

Title:
Quantifying the neurophysiological effects of 5-HT2A receptor activation on cortico-limbic and cortico-striatal network dynamics in rats

Quantifying the neurophysiological effects of 5-HT_{2A} receptor activation on cortico-limbic and cortico-striatal network dynamics in rats

Daniel Andrew Hetrell Titheradge

A dissertation submitted to the University of Bristol in accordance with the requirements for award of the degree of Master of Research in the Faculty of Science

Department of Physiology Pharmacology and Neuroscience

January 2021

Word Count: 29922 words

[Blank Page]

Abstract

5-Hydroxytryptamine 2A (5-HT_{2A}) receptor activation may contribute to the psychotomimetic and/or antidepressant effects of psychedelic drugs. 5-HT_{2A} agonists induce broadband changes in neural population activity, including high frequency oscillations (HFO) spanning diverse brain regions, however, the mechanisms and relevance of these oscillations remain unclear. I therefore quantified the effects of a selective 5-HT_{2A} agonist 25I-NBOH (25I) on the behaviour and neurophysiology of freely-behaving adult rats.

Local field potentials (LFP) were recorded from rats with electrodes arrays implanted in either cortico-limbic (prefrontal cortex, hippocampus, amygdala; n=5) or cortico-striatal (prefrontal cortex, hippocampus, nucleus accumbens; n=4) circuits. I developed an analysis pipeline encompassing video tracking of behaviour, spectral analysis, functional connectivity, and dynamic causal modelling (DCM).

25I induced visible behavioural changes, though quantification was limited by video resolution and sample size. Spectral analysis confirmed the emergence of HFO throughout cortico-limbic and cortico-striatal circuits, except in hippocampus. Functional connectivity analysis identified increased coupling between the amygdala and prefrontal cortex and implicated the nucleus accumbens as a likely source of HFO. Unexpectedly, changes in undirected (Fourier coherence) and directed (Granger causality) measures of functional connectivity were dissociable, highlighting different facets of these analyses and their interpretation.

DCM was used to model 25I's effects on the cortico-limbic circuit and identified (1) increases in top-down control of amygdala by prefrontal cortex, which may contribute to the antidepressant and anxiolytic effects of psychedelic drugs, and (2) disrupted top-down cortico-hippocampal connections, which may reflect psychotomimetic effects of $5HT_{2A}$-agonists. DCM also indicated that the effects of 25I on deep pyramidal neurons in the prefrontal cortex contributed to HFO.

This integrated pipeline enabled greater insights into the effects of 5-HT_{2A} agonism on cortico-limbic and cortico-striatal dynamics than achievable using individual analyses, exemplifying how computational measures and models allow cellular- and synaptic-resolution inferences from translational measures of neural population activity.

[Blank Page]

Dedication and acknowledgements

I would like to thank Professor Matt Jones for his supervision of this project and for his guidance throughout the year alongside everyone else in the Jones lab. I would also like to thank Dr Rosalyn Moran for her supervision and guidance in relation to the effective connectivity analysis presented in Chapter 5. I am extremely grateful to Dr Flavie Kersanté for undertaking the original experiments and collecting the data used in this thesis, and to Dr Alice Fodder who performed the surgery on some of the animals.

This work was funded by the Medical Research Council (MRC) through their funding of my post as an MRC Addictions Research Clinical Fellow (MARC). I would also like to thank Professor Matt Hickman, and Professor Anne Lingford-Hughes for giving me the opportunity to undertake this research and for providing supervision to me as a MARC clinical fellow.

Thanks also to my family, partner, and friends for enduring long conversations on neural oscillations, functional connectivity, and dynamic causal modelling.

[Blank Page]

Author’s declaration

I declare that the work in this dissertation was carried out in accordance with the requirements of the University's *Regulations and Code of Practice for Research Degree Programmes* and that it has not been submitted for any other academic award. Except where indicated by specific reference in the text, the work is the candidate's own work. Work done in collaboration with, or with the assistance of, others, is indicated as such. Any views expressed in the dissertation are those of the author.

SIGNED: ..... DATE: 8th January 2021

[Blank Page]

Table of Contents

Chapter 1. Introduction 1

1.1. The serotonin system 1

1.2. The 5-HT_{2A} receptor 1

1.3. Clinical relevance of the 5-HT_{2A} receptor 3

1.4. Neurophysiology 4

1.5. Background to the thesis 7

1.6. Aims of the thesis 7

Chapter 2. Experimental design 9

2.1. Overview of study design 9

2.2. Experimental methods 9

2.2.1. Ethical approval 9

2.2.2. Surgical procedures 10

2.2.3. Recording sites 11

2.2.4. Drugs 12

2.2.5. Electrophysiological recording 12

2.2.6. Confirmation of electrode placement 14

2.2.7. Data selection for analysis in subsequent chapters 17

Chapter 3. Suppression of locomotion and exploration by systemic activation of 5-HT_{2A} receptors 18

3.1. Introduction 18

3.2. Methods: Effects of 5-HT_{2A} drugs on behaviour 20

3.2.1. Processing of location data 21

3.2.2. Calculation of movement speed 22

3.2.3. Time spent in central zone of open field 22

3.2.4. Statistical analysis 23

3.3. Results 23

3.3.1. Movement speed decreased across both experimental conditions over the recording sessions 23
3.3.2. 25I causes visible changes in locomotion pattern 25
3.4. Discussion 28
3.4.1. Key findings 28
3.4.2. Comparison with existing literature 28
3.4.3. Limitations 29
3.4.4. Further work 29
Chapter 4. The neurophysiological effects of 5-HT_{2A} activation on cortico-limbic and cortico-striatal network dynamics 31
4.1. Introduction 31
4.1.1. Spectral analysis of neural population activity 31
4.1.2. Known spectral effects of 5-HT_{2A} agonists 32
4.1.3. What is functional connectivity? 34
4.1.4. Known effects of 5-HT_{2A} on functional connectivity 37
4.1.5. Aims of this chapter 38
4.2. Methods 38
4.2.1. Software 38
4.2.2. Pre-processing 38
4.2.3. Spectral analysis 42
4.2.4. Functional connectivity measures 43
4.2.5. Statistics 44
4.3. Results 47
4.3.1. Local field potentials 47
4.3.2. Spectral analysis 50
4.3.3. Increases in HFO power in cortico-limbic and cortico-striatal circuits is persistent; at other frequencies power shows a biphasic response 56
4.3.4. Time-domain functional connectivity: 58
4.3.5. Frequency domain functional connectivity 63
4.3.6. Baseline coherence provides anatomical insights 63

4.3.7. 25I causes specific changes in coherence occur across the cortico-hippocampal, cortico-limbic, and cortico-striatal circuits 67

4.3.8. Baseline Granger causality suggests a physiological role for HFO in the cortico-limbic circuit and affirms known roles of theta and gamma oscillations in cortico-hippocampal circuitry 67

4.3.9. 25I increases activation of a cortico-limbic loop between prefrontal cortex and BLA. 72

4.3.10. Granger causality analysis supports a directed flow of HFO from the NAC to the prefrontal cortex 73

4.3.11. 25I increases cortico-limbic and cortico-hippocampal communication 73

4.3.12. 25I increases cortico-striatal and prefrontal functional connectivity across a wide range of frequencies 76

4.3.13. Undirected and directed functional connectivity measures in the frequency domain showed dissociable patterns of drug-induced changes 77

4.4. Discussion 79

4.4.1. Key findings 79

4.4.2. Increases in HFO power in the nucleus accumbens, prefrontal cortex and basolateral amygdala extend known findings in the literature 80

4.4.3. Time domain functional connectivity has a clear role in functional connectivity analysis 81

4.4.4. Frequency domain functional connectivity is informative in baseline and control conditions as well as under the effects of 25I 81

4.4.5. 25I causes marked changes in the functional connectivity of the cortico-limbic, cortico-striatal, and cortico-hippocampal circuits with NAC driving changes in HFO activity 82

4.4.6. Changes in undirected and directed functional connectivity measures do not routinely show strong positive associations 83

4.4.7. Limitations of the study 83

4.4.8. Further work 84

Chapter 5. Systemic 5-HT_{2A} activation modulates effective connectivity in the cortico-limbic network 86

5.1. Introduction 86

5.2. Methods 87
5.2.1. Neural mass models 88
5.2.2. Anatomical models 89
5.2.3. Patterns of modulation 94
5.2.4. Frequency ranges for DCM models 94
5.2.5. Analysis pipeline 94
5.2.6. Testing anatomical hypotheses 96
5.2.7. Determination of leading models 97
5.2.8. Analysis of extrinsic connectivity in leading models 97
5.3. Results 98
5.3.1. LFP models more effective at low frequencies, CMM_NMDA models at high frequencies 98
5.3.2. The anatomical structure of effective connectivity models varies over the frequency spectra 98
5.3.3. Low frequency DCM model 100
5.3.4. Middle frequency DCM model 104
5.3.5. High frequency DCM model 108
5.4. Discussion 112
5.4.1. Implications for future research 112
5.4.2. The effective architecture of neural circuits varies with frequency 112
5.4.3. 5-HT_{2A} agonism increases top-down control of amygdala activity by prefrontal cortex 113
5.4.4. 5-HT_{2A} agonists disrupt the hierarchical organisation of the cortico-hippocampal circuit 113
5.4.5. Comparison with existing literature yields mechanistic insights 114
5.4.6. Limitations 115
5.4.7. Further work 115
Chapter 6. Discussion 118
6.1. Key findings 118

6.2. Further characterisation is needed of the pharmacokinetics and pharmacodynamics of 25I 118

6.3. Appraisal of the analysis pipeline 119

6.3.1. Refinement of behavioural analysis 119

6.3.2. Refinement of approaches to time series data 120

6.4. Future directions 120

6.5. Conclusions 121

References 123

List of tables

Table 2.1:	Coordinates used for electrode placement in the cortico-limbic experiments	Page 11
Table 2.2:	Coordinates used for electrode placement in the cortico-striatal experiments	Page 12
Table 3.1:	Movement speed by experiment, time point and drug	Page 25
Table 3.2:	Percentage of time spent in central zone of open field arena	Page 26
Table 4.1:	Frequency bands used for spectral analysis	Page 32
Table 4.2:	Summary of functional connectivity metrics	Page 36
Table 4.3:	Number of epochs remaining by animal and epoch after removal of epochs containing artefacts	Page 39
Table 4.4:	Chronux parameters used for analysis	Page 43
Table 4.5:	Summary of significant changes in spectral power	Page 79
Table 4.6:	Summary of significant changes in undirected temporal domain functional connectivity (correlation)	Page 79
Table 4.7:	Summary of significant changes in undirected frequency domain functional connectivity (coherence)	Page 80
Table 5.1:	Characteristics of neural mass models	Page 88

List of figures

Figure 1.1:	Diagram of the serotonin system and sites of action of common antidepressants	Page 2
Figure 1.2:	Diagram of the cortico-limbic and cortico-striatal circuits	Page 6
Figure 2.1:	Diagram of recording electrode array	Page 11
Figure 2.2:	Summary of study design	Page 14
Figure 2.3:	Location of electrodes in cortico-limbic experiments	Page 15
Figure 2.4:	Location of electrodes in cortico-striatal experiment	Page 16
Figure 3.1:	Raw and enhanced video images from a contemporaneous control experiment to demonstrate the experimental setup	Page 21
Figure 3.2:	Diagram of normalised arena and central zone	Page 22
Figure 3.3:	Graphs of movement speed over the duration of the recording period for 25I and control conditions	Page 24
Figure 3.4:	Change in movement speed across conditions	Page 25
Figure 3.5:	Heatmaps to show locations of rats over time for 25I and control conditions	Page 27
Figure 3.6:	Change in time spent in central area of arena	Page 26
Figure 4.1:	Overview of analysis pipeline for electrophysiology and functional connectivity	Page 41
Figure 4.5:	Representative LFP traces from a single animal in the cortico-limbic experiment	Page 48
Figure 4.6:	Representative LFP traces from a single animal in the cortico-striatal experiment	Page 49
Figure 4.7:	Representative spectrograms from a single animal in the cortico-limbic study	Page 51
Figure 4.8:	Representative spectrograms from a single animal in the cortico-striatal experiment	Page 52
Figure 4.9:	Power spectra by time point and region for cortico-limbic experiment	Page 54
Figure 4.10:	Power spectra by time point and region for cortico-striatal experiment	Page 55
Figure 4.11:	Percentage change in band-limited spectral power by region	Page 57
Figure 4.12:	Changes in temporal domain functional connectivity from baseline to the early post-drug period	Page 59
Figure 4.13:	Changes in temporal domain functional connectivity from baseline to the late post-drug period	Page 61
Figure 4.14:	Correlation between the change in undirected and directed temporal domain functional connectivity	Page 62

Figure 4.15:	Cortico-limbic coherence by region pair and frequency	Page 64
Figure 4.16:	Cortico-striatal coherence by region pair and frequency	Page 66
Figure 4.17:	Cortico-limbic spectral Granger causality by region pair and frequency in the control condition	Page 68
Figure 4.18:	Cortico-limbic spectral Granger causality by region pair and frequency in the 25I condition	Page 69
Figure 4.19:	Cortico-striatal spectral Granger causality by region pair and frequency in the control condition	Page 70
Figure 4.20:	Cortico-striatal spectral Granger causality by region pair and frequency in the 25I condition	Page 71
Figure 4.21:	Changes in frequency domain functional connectivity from baseline to the early post-drug period	Page 74
Figure 4.22:	Changes in frequency domain functional connectivity from baseline to the late post-drug period	Page 75
Figure 4.23:	Correlation between the change in undirected and directed frequency domain functional connectivity	Page 78
Figure 5.1:	Overview of connections in ERP and LFP neural mass models	Page 89
Figure 5.2:	Graphical depiction of anatomical models for hypothesis testing	Page 91
Figure 5.3:	Structure of DCM analysis	Page 95
Figure 5.4:	Family-wise comparison of the exceedance probability for neural mass and anatomical models for each frequency range	Page 99
Figure 5.5:	Leading low frequency (2-12Hz) model fits by condition and timepoint	Page 101
Figure 5.6:	Effects of 25I on extrinsic connectivity for the leading low frequency (2-12Hz) model	Page 103
Figure 5.7:	Leading middle frequency (12-48Hz) model fits by condition and timepoint	Page 105
Figure 5.8:	Effects of 25I on extrinsic connectivity for the leading middle frequency (12-48Hz) model	Page 107
Figure 5.9:	Leading high frequency (52-170Hz) model fits by condition and timepoint	Page 109
Figure 5.10:	Effects of 25I on extrinsic AMPA mediated connectivity for the leading high frequency (52-170Hz) model	Page 111
Figure 5.11:	Nucleus Accumbens as a functional analogue to striatum	Page 117

List of abbreviations

25I	2-[[2-(4-iodo-2,5-dimethoxyphenyl)ethylamino]methyl]phenol (25I NBOH; CIMBI-27)
5-HT	5-hydroxytryptamine (serotonin)
5-HT1A	5-HT 1A receptor
5-HT2A	5-HT 2A receptor
AMPA	α-amino-3-hydroxy-5-methyl-4-isoxazolepropionic acid
ANOVA	analysis of variance
ASC	Altered states of consciousness rating scale
BLA	Basolateral amygdala
BOLD	Blood-oxygen-level-dependent
CNS	Central Nervous System
CSD	Cross spectral density
DCA1	Dorsal CA1 region of hippocampus
DCM	Dynamic causal modelling
DMSO	Dimethyl sulfoxide
DMT	N,N-Dimethyltryptamine
DOI	2,5-Dimethoxy-4-iodoamphetamine
EEG	Electroencephalogram
EIB	Electrode interface board
FC	Functional connectivity
fMRI	functional magnetic resonance imaging
GC	Granger causality
GPCR	G protein coupled receptor
GPe	Globus pallidus externa;
GPi	Globus pallidus interna;
HFO	High frequency oscillations
HTR	Head twitch response
II	Inhibitory interneurons
IL	Infralimbic cortex
LED	Light emitting diode
LFP	Local field potential
LSD	lysergic acid diethylamide
MAO	Monoamine oxidase
MAOI	Monoamine oxidase inhibitor
MDMA	3,4-Methylenedioxymethamphetamine

MEG	Magnetoencephalogram
MRI	Magnetic resonance imaging
MVGC	Multivariate Granger causality
NAC	Nucleus accumbens core
NAS	Nucleus accumbens shell
NMDA	N-methyl-D-aspartate
PEB	Parametric empirical bayes
PET	Positron emission tomography
PLC	Phospholipase C
PRL	Prelimbic cortex
PTSD	Post-traumatic stress disorder
Pyr	Pyramidal neurons
ROI	Region of interest
SD	Standard deviation
SERT	Serotonin transporter
SPM	Statistical parametric mapping
SS	Spiny stellate cells
SSRI	Selective serotonin reuptake inhibitor
STN	Subthalamic nucleus
VAR	Vector autoregression
VCA1	Ventral CA1 region of hippocampus
VP	Ventral Pallidum

Chapter 1. Introduction

1.1. The serotonin system

5-hydroxytryptamine (5-HT), also known as serotonin, is a key excitatory neurotransmitter throughout the animal kingdom. The roles of 5-HT in the modulation of behaviour appear to be evolutionarily conserved from invertebrates to mammalian species (Bacqué-Cazenave et al., 2020). 5-HT does not pass the blood brain barrier, requiring synthesis in specialised neurons in the brain. Serotonin is synthesised in the raphe nuclei in the midline of the brainstem which send long range projections throughout the central nervous system (CNS) (Hornung, 2003, Vertes, 1991). Serotonin is released into the synaptic cleft where it modulates neurotransmitter release and synaptic transmission before being broken down by monoamine oxidase, or actively transported back into pre-synaptic terminals.

In humans 5-HT is of particular interest due to its implication in mood disorder, with drugs targeting the serotonergic system key treatments for depression. Early antidepressants acted as Monoamine Oxidase Inhibitors (MAOI) reducing the breakdown of 5-HT, dopamine and noradrenaline (Figure 1.1). The most commonly prescribed antidepressants are Selective Serotonin Reuptake Inhibitors (SSRIs)(Heald et al., 2020). Acutely SSRIs increase the level of synaptic 5-HT by blocking the Serotonin Transporter (SERT) responsible for removal of 5-HT from the synaptic cleft (Figure 1.1), however, the mechanism of long term action is likely through effects on receptor expression and neuroplasticity (Vahid-Ansari et al., 2019).

1.2. The 5-HT_{2A} receptor

5-HT has both systemic and CNS effects and acts on a wide variety of receptors that are primarily G protein coupled receptors (GPCR) (Berger et al., 2009). GPCRs span the intracellular membrane and activate intracellular signalling cascades in response to the binding of extracellular ligands (Rosenbaum et al., 2009).

The mammalian central nervous system contains 14 subtypes of serotonin receptors that have both inhibitory and excitatory effects on neuronal transmitter (Barnes and Sharp, 1999). The 5-HT_{2A} receptor is a GPCR coupled to $G_{q/11}$ that results in intracellular activation of phospholipase C (PLC) on ligand binding (López-Giménez and González-Maeso, 2018, Millan et al., 2008). This leads to generation of inositol phosphate derivatives and related compounds, intracellular Calcium release, and downstream changes in gene expression (López-Giménez and González-Maeso, 2018, Millan et al., 2008). The 5-HT_{2A} receptor can

also activate other intracellular signalling cascades including activation of phospholipase A_2, activation of nitric oxide synthase, and direct effects on ion channels (Millan et al., 2008). The binding of different ligands of the 5-HT_{2A} receptor has been shown to result in different patterns of intracellular signalling with different ligands showing unique transcriptomes in the sensory cortex of mice (González-Maeso et al., 2003).

Figure 1.1: Diagram of the serotonin system and sites of action of common antidepressants

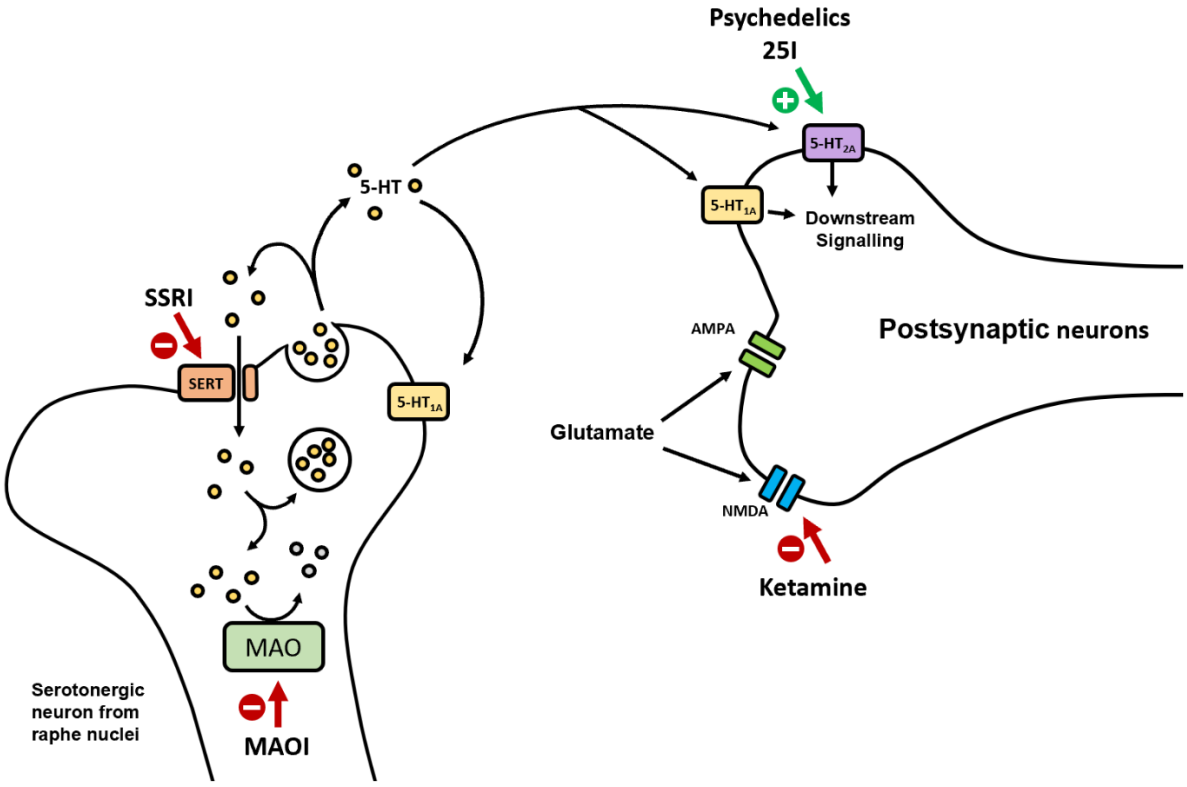

For description of serotoninergic pathway please refer to text in body of Section 1.1. Site of action of traditional antidepressants SSRIs, MAOIs highlighted alongside site of action of psychedelic drugs, 25I and ketamine. Note that 5-HT_{1A} receptors are expressed pre and postsynaptically. 25I, 25I-NBOH (selective 5-HT_{2A} agonist); 5-HT, 5-hydroxytryptamine; 5-HT_{1A}, 5-HT_{1A} receptor; 5-HT_{2A}, 5-HT_{2A} Receptor; AMPA, α-amino-3-hydroxy-5-methyl-4-isoxazolepropionic acid glutamate receptor; MAO, Monoamine Oxidase; MAOI, Monoamine Oxidase inhibitor; NMDA, N-methyl-D-aspartate glutamate receptor; SERT, serotonin reuptake transporter; SSRI, selective serotonin reuptake inhibitor.

The inhibitory action of 5-HT_{1A} and excitatory action of 5-HT_{2A} receptors are key pharmacological targets in the management of psychiatric disorder (Carhart-Harris and Nutt, 2017). SSRIs have been proposed to mediate their effects primarily through enhancement of post-synaptic 5-HT_{1A} receptor signalling reducing activation of the limbic system and increasing stress tolerance, whilst the 5-HT_{2A} receptor acts to modulate activity in higher brain regions resulting in increased plasticity and adaptability (Carhart-Harris and Nutt, 2017).

5-HT_{2A} immunoreactivity is associated with cortical pyramidal neurons and parvalbumin containing GABAergic interneurons (Willins et al., 1997) with activation of 5-HT_{2A} receptors leading to excitation of both pyramidal cells and interneurons in the cortex (Marek and Aghajanian, 1996). Analysis of 5-HT_{2A} receptor mRNA demonstrated broad cortical expression with very high levels of expression in the neocortex, and more variable expression in subcortical regions (Pompeiano et al., 1994). In humans the distribution of 5-HT receptors has been mapped across the brain using Positron Emission Tomography (PET) and Magnetic Resonance Imaging (MRI) with a variety of radio-ligands (Beliveau et al., 2017). Cortical regions demonstrate the highest density of 5-HT_{2A} receptors; with the nucleus accumbens, amygdala and hippocampus demonstrating similar levels of 5-HT_{2A} density, albeit at a lower level than in the cortical regions in line with findings from similar studies (Beliveau et al., 2017, Ettrup et al., 2014).

Historically rodent studies of the 5-HT_{2A} receptor have tended to use psychedelic drugs like lysergic acid diethylamide (LSD; a mixed 5-HT_2/5-HT_1 partial agonist) or 2,5-Dimethoxy-4-iodoamphetamine (DOI; a selective 5-$HT_{2A/B/C}$ agonist) which act as potent, but not selective agonists of the 5-HT_{2A} receptor (Passie et al., 2008, Canal and Morgan, 2012). The development of PET ligands for the 5-HT_{2A} receptor has led to highly selective agonists being developed that allow for more precise targeting of the 5-HT_{2A} receptor (Ettrup et al., 2011, Hansen et al., 2014).

1.3. Clinical relevance of the 5-HT_{2A} receptor

In recent years there have been publications of clinical trials using psychedelic drugs to treat anxiety and depression disorders, obsessive compulsive disorder and substance use disorders, with agents used including psilocybin, LSD, N,N-Dimethyltryptamine (DMT) and mescaline as reviewed by Andersen et al. (Andersen et al., 2020). Psilocybin is a naturally occurring prodrug that is metabolised by hepatic first pass metabolism into the active compound psilocin which acts as a non-selective 5-HT_{2A} partial agonist (Geiger et al., 2018). Psilocybin has been shown to be beneficial in open label studies for treatment resistant depression (TRD) (Carhart-Harris et al., 2016a) with benefits persisting at 6 months follow up

(Carhart-Harris et al., 2018a). Psilocybin has also been shown to work as a rapid acting antidepressant in patients with major depressive disorder in a randomised trial (Davis et al., 2020).

The 5-HT_{2A} receptor is the primary site of action for psychedelic drugs which act as agonists or partial agonists at the 5-HT_{2A} receptor, and acutely have profound effects on behaviour, consciousness, and perception (Nichols, 2004). The dose required to experience these subjective psychedelic effects is strongly correlated with the strength of the drugs' binding affinity for the 5-HT_{2A} receptor (Sadzot et al., 1989). The subjective intensity of psychedelic experiences with psilocybin have been demonstrated to correlate with plasma psilocin levels, and 5-HT_{2A} receptor occupancy as measured by displacement of a selective 5-HT_{2A} agonist [^{11}C] Cimbi-36 using Positron Emission Tomography (PET)(Madsen et al., 2019). It has not yet been demonstrated whether agonism at the 5-HT_{2A} receptor is sufficient to provide an antidepressant effect – although 5-HT_{2A} agonism is conclusively related to the subjective experiences of psychedelic drugs.

Alongside these potential positive impacts on mood, psychedelic drugs are also recognised to have psychotomimetic effects, with acute intoxication resulting in a mental state similar to that seen in acute psychosis (Carhart-Harris et al., 2016b). 5-HT_{2A} receptor action was shown to be required for the psychotomimetic effects of psilocybin in humans (Vollenweider et al., 1998). Therapeutically the treatments for psychotic illness and mood disorder converge upon the 5-HT_{2A} receptor with atypical antipsychotics acting as either 5-HT_{2A} antagonists or inverse agonists (Sullivan et al., 2015). Indeed, the data presented in this thesis was originally collected as part of a study on rodent models of psychosis, highlighting a further perspective on the importance of this receptor in psychiatric treatment.

1.4. Neurophysiology

The effects of a pharmacological agent on an animal can be described at a variety of levels, from behavioural changes to changes in individual receptors and gene expression. In Chapter 3 of this thesis, I summarise the literature on the behavioural changes caused by 5-HT_{2A} agonists in rodents and present my own analysis of the effects of 5-HT_{2A} agonism on the behaviour of freely behaving rats. For the remainder of this introduction, I focus on the describing the neurophysiology and neural circuits underpinning the analysis of the effects of 5-HT_{2A} agonism on neural activity and network dynamics presented in Chapter 4 and 5.

In human studies we can infer what is happening inside the brain in several ways including functional Magnetic Resonance Imaging (fMRI), electroencephalogram (EEG) and

magnetoencephalogram (MEG). In animal studies it is also possible to record electrical activity from implanted electrodes and measure either Local Field Potentials (LFP) or observe the spiking behaviour of individual neurons. The LFP signal is the summation of a wide range of neuronal processes including synaptic currents, action potentials, calcium spikes and intrinsic neuronal activity (Buzsáki et al., 2012). Neuronal systems have characteristic patterns of activity in specific states that result in the generation of oscillations at different frequencies that can be quantified using spectral analysis (see Chapter 4).

An understanding of the relative strengths of different oscillations in different states can be used to characterise the activity in different brain regions, and in turn can be used to make inferences about what is taking place inside the brain (Siegel et al., 2012). In some cases, the neural circuitry underlying the generation of oscillatory behaviour is known (Buzsáki, 2002, Buzsáki and Wang, 2012), although many areas require further study. Neural oscillations have varied physiological associations and roles within the brain, depending on the frequency and source, with putative roles in synchronisation, information transfer, and computation (Sirota et al., 2008, Fries, 2009). Importantly abnormal neuronal oscillations are implicated in the pathophysiology of psychiatric disease such as schizophrenia, where abnormalities in interneurons impair cortical gamma-frequency synchronisation disrupting the normal patterns of neuronal activation and information propagation (Lewis et al., 2005). Abnormalities in neuronal oscillation may also provide biomarkers for the diagnosis of psychiatric diseases such as depression and for assessment of the treatment response (Fitzgerald and Watson, 2018).

Within the brain neuronal populations are organised into highly interconnected networks with functional specialisation. In this thesis I focus on the effects of 5-HT_{2A} agonism on an interconnected network consisting of the cortico-limbic and cortico-striatal circuits. The cortico-limbic circuit consists of the prefrontal cortex, the amygdala and hippocampus, whilst the cortico-striatal circuit consists of the prefrontal cortex, nucleus acumbens and hippocampus, and forms the limbic loop of the basal ganglia. An overview of this network is illustrated in Figure 1.2 and described in more detail in subsequent chapters, particularly Chapter 5 (see Section 5.2).

Hyperactivity in the amygdala, accompanied by a loss of top-down modulation from the prefrontal cortex is a well-established component of the pathophysiology of PTSD and anxiety disorders (Martin et al., 2009). Substance use disorders are driven by a loss of top-down control by the prefrontal cortex over the striatum, alongside increased drive from the amygdala among other regions (Everitt and Robbins, 2016). The pathway between the hippocampus and prefrontal cortex is implicated in disorders as diverse as depression, schizophrenia and

post-traumatic stress disorder (PTSD) (Godsil et al., 2013). The hippocampus and prefrontal cortex are also key components of the default mode network (DMN), a target commonly identified as having reduced functional connectivity following administration of psychedelic drugs and antidepressants (Müller et al., 2020). Given the central role of the cortico-limbic system in psychiatric illness, the high expression of 5-HT_{2A} receptors in the prefrontal cortex and changes in the DMN the cortico-limbic system presents a likely site of action for the therapeutic effects of 5-HT_{2A} agonists.

Figure 1.2: Diagram of the cortico-limbic and cortico-striatal circuits

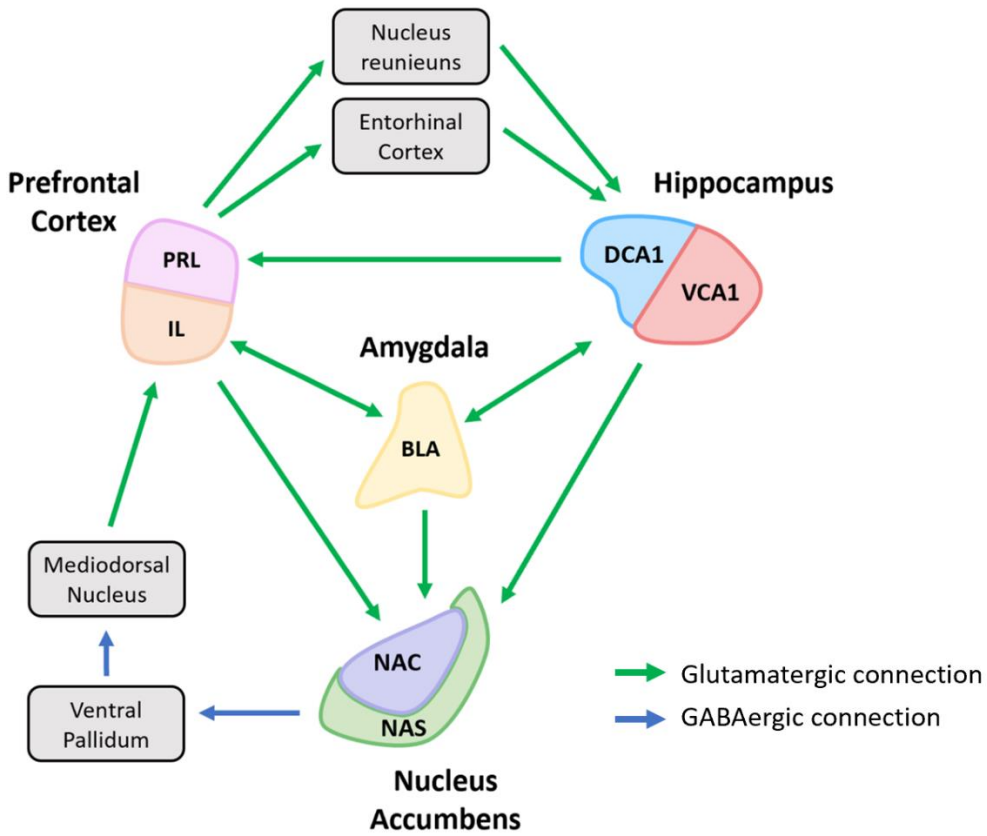

An overview of the cortico-limbic, cortico-striatal and cortico-hippocampal circuits. Sites used for implantation of recording electrodes (see Chapter 2) are highlighted in colour. Green arrows represent glutamatergic connections, blue arrows represent GABAergic connections. Inter-regional connections are shown with single arrows, although parallel pathways are present anatomically. In general connections between the cortico-limbic and cortico-striatal loops are stronger with DCA1 than VCA1. In the cortico-limbic circuit PRL innervates NAC more strongly than NAS, while IL innervates NAS more strongly than NAC. The circuit from the nucleus accumbens to the prefrontal cortex via the ventral pallidum and the mediodorsal nucleus of the thalamus is described in Section 5.2 (page 87). The connection from the prefrontal cortex to the hippocampus via the nucleus reuniens and entrohinal cortex is described in the text in Section 5.2.2 (page 92). BLA, basolateral amygdala; DCA1, dorsal CA1; IL, infralimbic cortex; NAC, nucleus accumbens core; NAS, nucleus accumbens shell; PRL, prelimbic cortex; VCA1 ventral CA1.

1.5. Background to the thesis

In preliminary work in the Jones lab, it was identified that 5-HT_{2A} agonists including psilocybin and more selective agonists appeared to induce marked changes in the power spectra recorded in the prefrontal cortex, basolateral amygdala and nucleus accumbens. These changes included the emergence of distinct bands of non-physiological High Frequency Oscillations (HFO) shortly after treatment. Similar patterns of HFO were first reported in the nucleus accumbens of rats following subanaesthetic ketamine treatment (Hunt et al., 2006). Subsequent work by the same group demonstrated that HFO was also induced in the Nucleus Accumbens by 5-HT_{2A} agonists alongside a reduction in low gamma power and increases in high gamma oscillations (Goda et al., 2013).

Ketamine primarily acts as an NMDA receptor antagonist and at subanaesthetic doses is also associated with marked changes in consciousness (Mueller et al., 2018). Ketamine is increasingly being used as an antidepressant due to its fast onset and effectiveness in treatment resistant depression (Park et al., 2019), with changes in gamma oscillations proposed as a potential mediator of the antidepressant effects of ketamine in humans (Nugent et al., 2019). Given the shared action of both 5-HT_{2A} agonists and NMDA antagonists as antidepressants, and the similar pattern of HFO induced by both drug classes in the cortico-limbic system, it is plausible that the emergence of HFO may contribute to the antidepressant effects of 5-HT_{2A} agonists.

1.6. Aims of the thesis

Given the emerging therapeutic roles of 5-HT_{2A} agonists as antidepressants and the established role of 5-HT_{2A} antagonists as antipsychotic medications, a greater understanding of the actions of the role of this receptor is likely to be beneficial. Much of the human neurophysiological data on 5-HT_{2A} agonists comes from fMRI and MEG studies and highlights the effects of these drugs in changing patterns of functional connectivity and network communication within the brain. Human studies are constrained by the limitations of non-invasive recording with fMRI having poor temporal resolution and MEG limited to recording near the surface of the cortex.

In this thesis I explore the effects of a highly selective 5-HT_{2A} agonist, 25I-NBOH (25I) (Ettrup et al., 2011, Hansen et al., 2014) upon the cortico-limbic and cortico-striatal systems in freely behaving rats using implanted electrodes to measure LFP. In the following chapters I describe the effect of 25I on behaviour, neurophysiology, functional connectivity and effective

connectivity with the aim of understanding of the effects of 5-HT_{2A} agonism on the cortico-limbic and cortico-striatal circuits.

The broader secondary aim of this thesis is to establish an analysis pipeline for (1) the quantification of distributed network activity and interactions and (2) inference of biophysical mechanisms, that can be more broadly applied to the analysis of pharmacological interventions.

Chapter 2. Experimental design

2.1. Overview of study design

Data for this project was collected in two sets of parallel experiments designed to quantify the effects of systemic 5-HT_{2A} activation on neural network activity in the cortico-limbic and cortico-striatal circuits of freely-behaving adult male rats. The original data was collected by Flavie Kersante in the Jones lab between 31st January 2014 and 2nd April 2015, during her postdoctoral research. Surgical procedures were undertaken by Flavie Kersante and Alice Fodder, a previous Ph.D. student in the group.

Neither the data nor the analyses presented in this MSc project have previously been published. The data had been informally explored in preliminary analyses, which informed the development of my own work. I replicated, extended, and developed the previous pilot study into the body of work presented in this thesis.

2.2. Experimental methods

This project explores the effects of a potent 5-HT_{2A} agonist, 25I-NBOH on the behaviour and neurophysiology of freely-behaving adult rats. Two sets of experiments were conducted using the equivalent methodology in two independent groups of animals. The experiments differed on the basis of the locations in which the recording electrodes were placed, with the cortico-limbic experiment centred on the basolateral amygdala (BLA) and the cortico-striatal experiment centred on the nucleus accumbens.

2.2.1. Ethical approval

All experiments and procedures were performed in accordance with the UK Animals Scientific Procedures Act (1986) and with the consent of the University of Bristol Animal Welfare and Ethical Review Board. The work was covered by a UK Home Office Project Licence held by Professor Matt Jones and adhered to the principles of the 3Rs (Replacement, Reduction and Refinement) throughout.

2.2.2. Surgical procedures

Similar methods have been described in detail elsewhere (Forsyth et al., 2012, Howe et al., 2020). Here, I include all details necessary to inform interpretation of my analyses in Chapters 3-5.

All rats were allowed to habituate to the University of Bristol Animal Services Unit for at least 1 week following delivery from Charles River, UK and Harlan, UK. Rats were then gently handled daily, habituating them to the experimenter, recording room and the single-housing necessary to avoid animals damaging cranial implants.

LFP electrodes consisted of 60µm diameter nichrome wires (gold-plated to impedances of 100-300KOhms at 1KHz) held in stereotactically aligned arrays and connected to EIB-36 Electrode Interface Boards (Neuralynx, MT, USA). These arrays were implanted under isoflurane recovery anaesthesia in aseptic conditions, with peri-operative analgesia (0.025 mg/kg buprenorphine, intraperitoneal [i.p.]) administered according to the advice of a Named Veterinary Surgeon. A diagram of the recording array is shown in Figure 2.1.

Once surgical anaesthesia had been achieved, craniotomies were drilled to allow placement of 4-6 anchor screws (stainless steel, 1.2mm diameter) around the perimeter of the dorsal skull. Screws overlying the cerebellum acted as ground/reference electrodes and were connected to the ground pin of the EIB36 using silver wire. Craniotomies of 1-2mm diameter were also drilled to allow insertion of LFP electrodes, using the stereotaxic coordinates detailed below. The dura mater was removed from the craniotomy surface prior to electrode insertion into the brain. Once all screws and electrodes were in place, the implant was permanently cemented to the skull using antibiotic-impregnated dental cement (gentamycin cement, DePuy) and the implant surrounded by a protective aluminium cone. Rats were then allowed to recover on a heated blanket and provided with highly palatable and nutritious diet gel.

For the week following surgery animals were weighed daily and food and water intake was monitored until recovery. Following surgery, the animals were individually housed in high-roofed cages with free access to food and water.

Figure 2.1: Diagram of recording electrode array

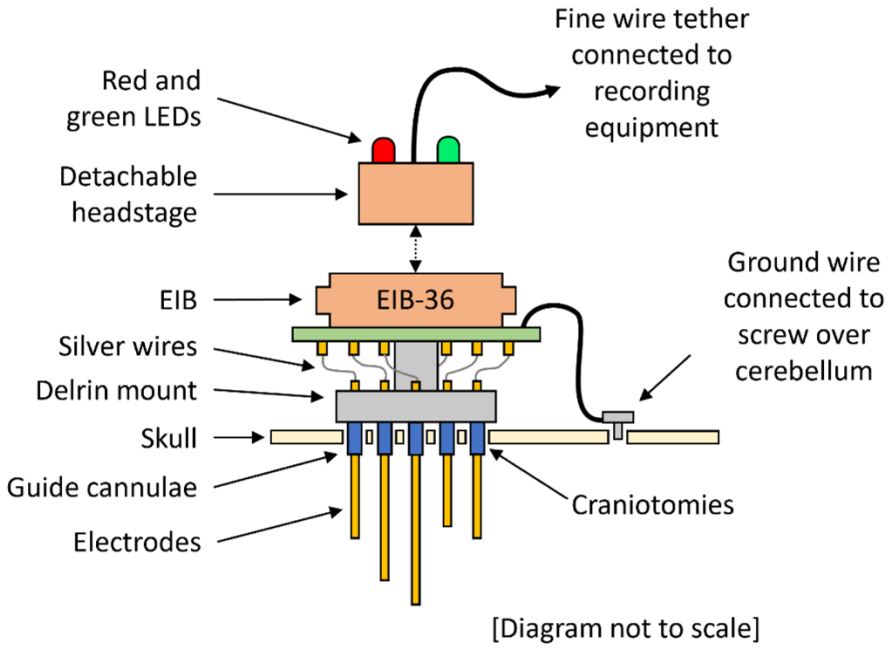

Electrodes made from 60µm diameter nichrome wires (gold-plated to impedances of 100-300KOhms at 1KHz) were held in a stereotactic array using a machined delrin (Bay plastics Ltd) mount, and 30-gauge guide cannulae (Coopers Needle Works). The length of electrodes was determined by the required dorsal-ventral length for each recording site (Tables 2.1 and 2.2). Electrodes passed through craniotomies of 1-2mm and were connected via silver wires to the electrode interface board (EIB). The ground wire of the EIB was connected to a screw overlying the cerebellum. The implant was permanently secured to the skull using antibiotic-impregnated dental cement (gentamycin cement, DePuy) and protected with an aluminium cone (not shown). For recording sessions, a detachable headstage was attached to the EIB which in turn was connected to the recording equipment via a counterbalanced fine wire tether. Red and green light emitting diodes (LEDs) on the headstage were used for video tracking.

2.2.3. Recording sites

The cortico-limbic experiment included five male Wistar rats (300-400g, Charles River, UK) with chronically implanted local field potential (LFP) electrodes inserted in the right basolateral amygdala (BLA), dorsal hippocampus CA1 (DCA1), infralimbic Cortex (IL) and prelimbic cortex (PRL). LFP recording electrodes were targeted using coordinates from the Paxinos and Watson stereotactic atlas (Paxinos and Watson, 2007). The stereotactic coordinates used for the cortico-limbic experiments are shown in Table 2.1.

Table 2.1: Coordinates used for electrode placement in the cortico-limbic experiments

Location	Anterior-posterior (mm)	Medial-lateral (mm)	Dorsal-ventral (mm)
Prelimbic cortex (PRL)	3.2	0.6	2.8
Infralimbic cortex (IL)	3.2	0.6	4.4
Dorsal hippocampus (DCA1)	-3.2	2.2	2.2
Basolateral amygdala (BLA)	-2.4	5	8.4

The cortico-striatal experiment consisted of four male Lister Hooded rats (400 - 420 g Harlan, UK) with chronically implanted LFP electrodes inserted in the right nucleus accumbens core (NAC), nucleus accumbens shell (NAS), prelimbic cortex (PRL), infralimbic cortex (IL), dorsal hippocampus CA1 (DCA1) and ventral hippocampus CA1 (VCA1). The stereotactic coordinates used for the cortico-striatal experiments are shown in Table 2.2.

Table 2.2: Coordinates used for electrode placement in the cortico-striatal experiments

Location	Anterior-Posterior (mm)	Medial-Lateral (mm)	Dorsal-Ventral (mm)
Prelimbic cortex (PRL)	3.2	0.6	3.35
Infralimbic cortex (IL)	3.2	0.6	4.35
Nucleus accumbens core (NAC)	1.6	1.2	6.7
Nucleus accumbens shell (NAS)	1.6	1.2	7.7
Dorsal hippocampus (DCA1)	-3.2	2.2	2.2
Ventral hippocampus (VCA1)	-6.3	5.5	4.1

2.2.4. Drugs

2-[[2-(4-iodo-2,5-dimethoxyphenyl)ethylamino]methyl]phenol, also known as 25I-NBOH (25I) and CIMBI-27 is a highly selective 5-HT_{2A} agonist and was synthesised in the laboratory of Dr Jesper Kristensen at the University of Copenhagen (Hansen et al., 2014). 25I was dissolved in double distilled water to a concentration of 2mg/ml. The vehicle injection was prepared from 10% Dimethyl Sulfoxide (DMSO), 20% Cremophor and 70% normal saline.

2.2.5. Electrophysiological recording

All electrophysiological recording took place in a 73.2cm diameter circular open field arena with 40cm high opaque walls and sawdust-covered floor (sawdust replaced between rats and recording sessions), placed on the floor of a behavioural testing room (see example video stills in Figure 3.1). Recordings took place during the day, *i.e*. the animals' light phase. The animals were handled daily for habituation to the experimenter, the room, the open field arena, and the recording equipment for a week prior to recording. The study design is summarised graphically in Figure 2.2.

The behavioural testing room was minimally lit with the lights in the recording room switched off from the start of the recording period. After a 30-minute period of habituation to the arena, animals were removed from the arena for an intraperitoneal injection of either active drug or a control injection. Recording continued for 40 to 90 minutes following the administration of the

injection. Animals only received further handling during this period if they required experimenter intervention for adjustment of recording equipment.

Control recording sessions, during which animals were injected with a either a vehicle injection (cortico-limbic experiments) or saline (cortico-striatal experiments), were completed a minimum of 10 weeks prior to the drug recording sessions (mean 115.8 days SD 95.1). Animals in the cortico-limbic experiments were given i.p. injections of either 2mg/kg 25I in the active drug session or an equal volume 1ml/kg vehicle injection in the control session. Animals in the cortico-striatal experiments were given i.p. injections of either 2mg/kg 25I in the active drug session or an equal volume 1ml/kg saline injection in the control session.

An overhead visible light camera was placed above the open field arena to monitor animal behaviour and was running throughout the recording sessions. Video was captured at a resolution of 720x576 pixels at 25 frames per second. The headstage used during recording sessions was fitted with green and red LEDs that were used to track head position and direction using the Neuralynx software (see Figure 2.1).

Recording from the LFP electrodes was performed using Digital Lynx hardware and Neuralynx Cheetah software. The LFP electrodes were connected to a headstage amplifier attached to the animal which was in turn connected to the recording hardware via a counterbalanced fine wire tether (see Figure 2.1). LFP signals were recorded relative to ground and sampled at 1017Hz in the BLA experiments and 1010Hz in the NAC experiments.

Video tracking and LFP data was recorded for a minimum of 12 minutes pre-injection and a minimum of 41 minutes post injection. Recording of LFP and video tracking data was continuous with the exception of brief periods at the time of injection and brief periods where there were problems with the recording equipment.

Figure 2.2: Summary of study design

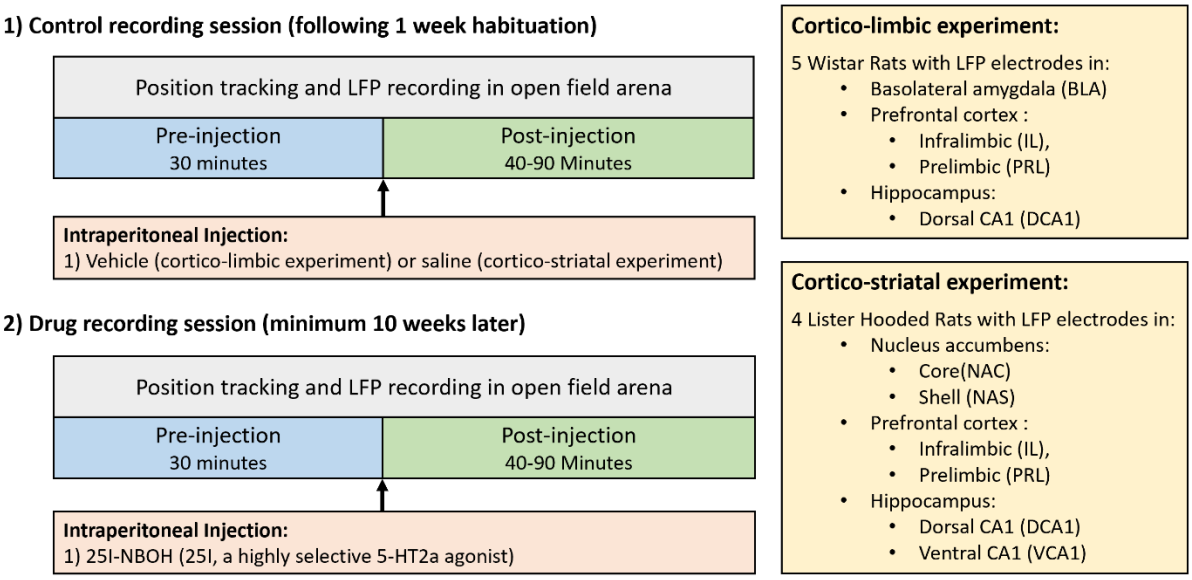

2.2.6. Confirmation of electrode placement

Following completion of experiments the animals were deeply anaesthetised with sodium pentobarbital until the limb reflex had ceased. In order to ascertain the exact location of the LFP electrodes, an electrolytic lesion was performed at each electrode site by passing a 30uA positive current through the recording electrode, with the ground terminal attached to the animal's ear. Animals were transcardially perfused with 0.9% saline, followed by 4% paraformaldehyde in phosphate buffered saline. Post-mortem, the brain from each animal was removed and cut into 50µm sections for light microscopy. Slides were stained with thionin blue and photographed under light microscopy. Where I was able to identify the position of the electrolytic lesion, I have mapped the electrode sites onto brain atlas sections in Figure 2.3 and Figure 2.4 respectively for the cortico-limbic and cortico-striatal experiments.

Figure 2.3: Location of electrodes in cortico-limbic experiments

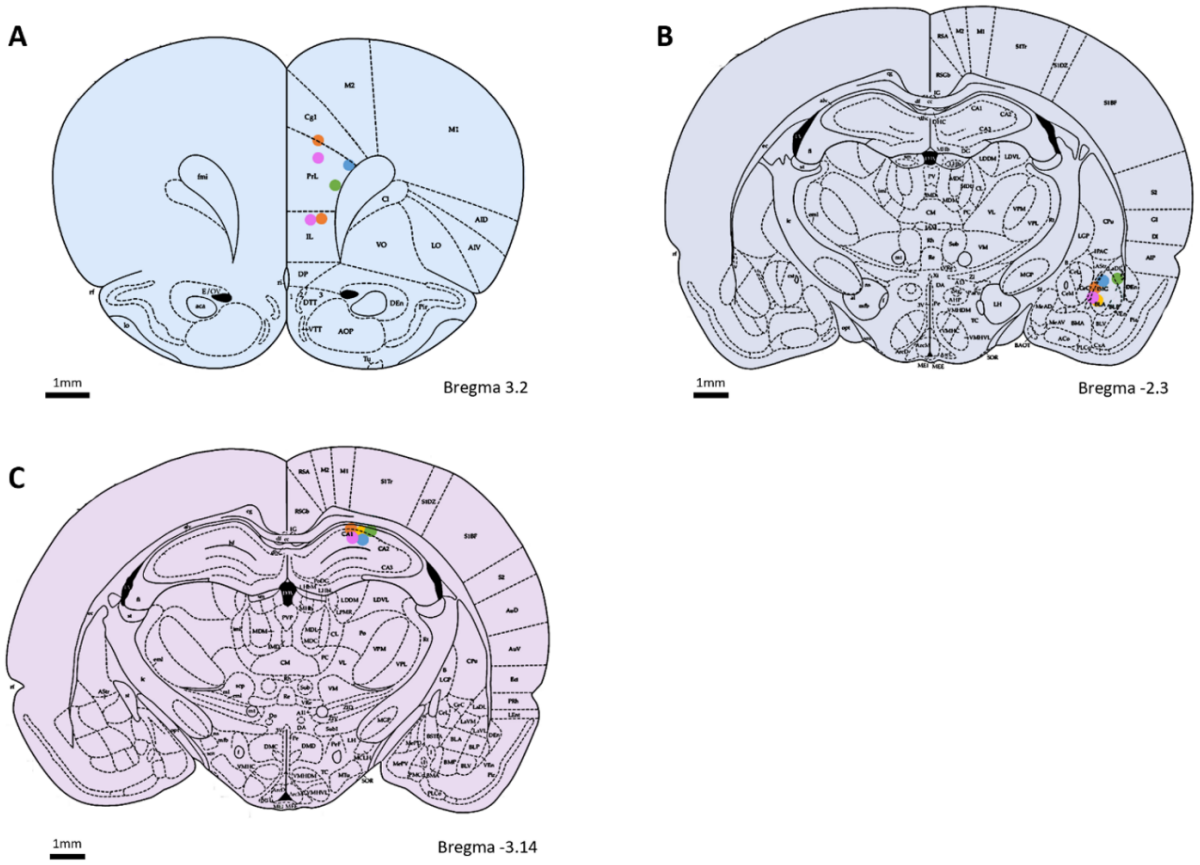

Electrode locations for the cortico-limbic experiment are shown on anatomical slides reproduced from the Paxinos and Watson stereotactic atlas (Paxinos and Watson, 2007). Locations are shown on the coronal section that was nearest to the stereotactic coordinates of the target. Where identifiable the electrode for each animal is represented by a coloured dot according to the legend. **A** Location of prefrontal electrodes; only some prefrontal electrode locations could be visualised. PRL electrodes within the bounds and along the dorsal border of PRL. IL electrodes are located ventrally within the bounds of IL. **B** Location of electrodes in BLA; electrodes mostly clustered at the medial border of BLA, with a single electrode at the lateral border. **C** Location of dorsal CA1 electrodes.

Legend

- Animal 1
- Animal 2
- Animal 3
- Animal 4
- Animal 5

Figure 2.4: Location of electrodes in cortico-striatal experiment

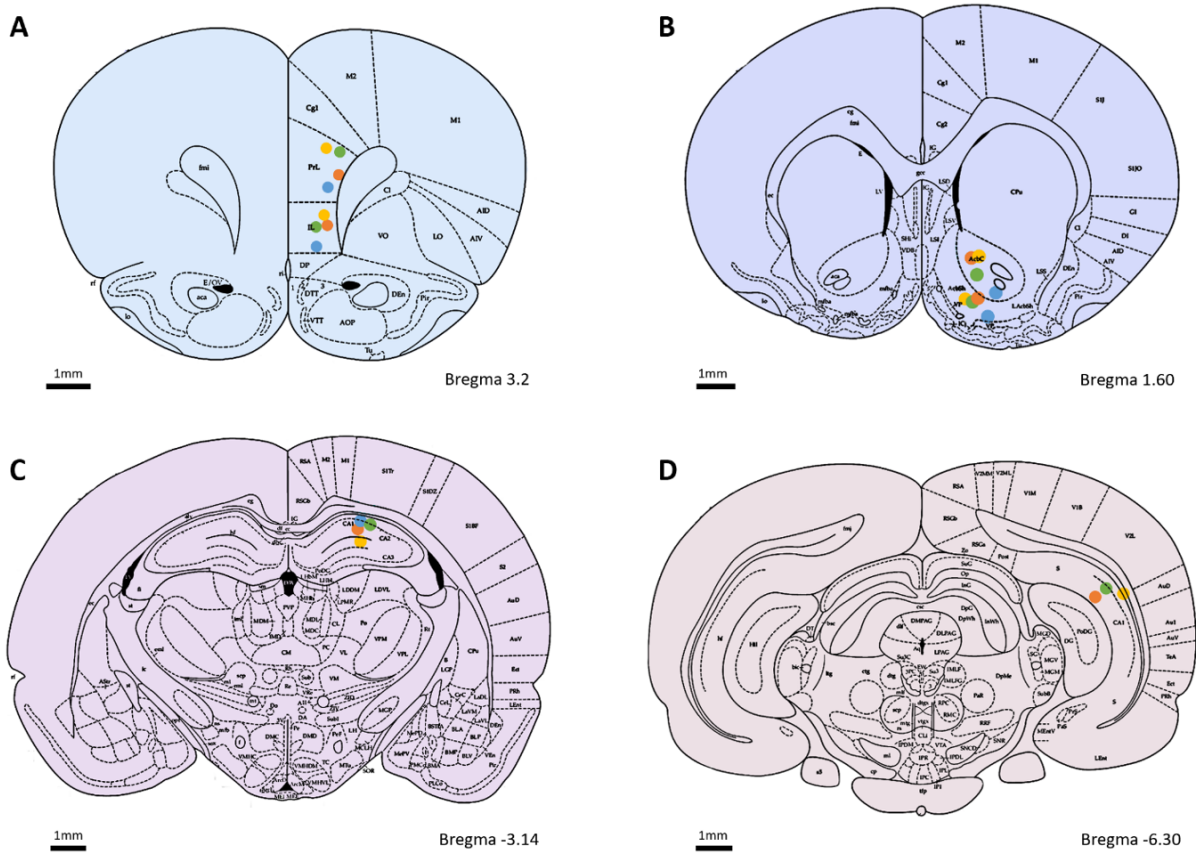

Electrode locations for the cortico-striatal experiment are shown on anatomical slides reproduced from the Paxinos and Watson stereotactic atlas (Paxinos and Watson, 2007). Locations are shown on the coronal section that was nearest to the stereotactic coordinates of the target. Where identifiable the electrode for each animal is represented by a coloured dot according to the legend. **A** Location of prefrontal electrodes. PRL electrodes located dorsally within the bounds of PRL and IL electrodes are located ventrally within bounds of II. **B** Location of nucleus accumbens electrodes. NAC electrodes are located dorsally within the bounds of the accumbens core and NAS electrodes are located ventrally within the bounds of the accumbens shell. **C** Location of DCA1 electrodes. **D** Location of ventral CA1 electrodes.

Legend

- Animal 1
- Animal 2
- Animal 3
- Animal 4

2.2.7. Data selection for analysis in subsequent chapters

For electrophysiological analysis, baseline, early post-drug and late post-drug periods were selected from periods where data was complete across all animals and without interruption. The baseline period of 5-10 minutes prior to the injection of drug or control was selected to provide the maximum period of acclimatisation, whilst avoiding potential disruption to behaviour in the recording room immediately prior to the injection. This baseline period is used in both the behavioural analysis in Chapter 3 and electrophysiological analysis in Chapters 4 and 5.

Preliminary analysis of spectrograms of the electrophysiological data suggested that the effects of 25I demonstrate significant changes over the timeframe captured in the recording sessions. For both the behavioural and electrophysiological analysis it was felt to be important to allow the animals sufficient time to recover from any stress related to the injection itself, without missing early effects of the drug. For the electrophysiological analysis, an early post-drug period from 5-10 minutes post injection was selected on this basis, with a late post-drug period of 35-40 minutes selected as the last period for which complete data was available across all animals in the study. For the behavioural analysis presented in Chapter 3, a single post-drug period was defined from 5-40 minutes, given the lower temporal resolution of the video tracking data.

Details of the analysis and methods specific to Chapters 3-5 is presented in Section 3.2, Section 4.2, and Section 5.2, respectively.

Chapter 3. Suppression of locomotion and exploration by systemic activation of 5-HT_{2A} receptors

3.1. Introduction

Psychedelic drugs are known to have marked effects on human consciousness. In human studies, these effects are most commonly characterised using the 11 factor Altered States of Consciousness (ASC) rating scale (Studerus et al., 2010). The ASC enables discrimination of the effects of psychedelic drugs from other psychotropic drugs and is intended to cover a broad range of altered states (Studerus et al., 2010). The ASC subscales include: experience of unity, spiritual experience, blissful state, insightfulness, disembodiment, impaired cognition and control, anxiety, complex imagery, elementary imagery, audio-visual synaesthesiae and changed meaning of perceptions (Studerus et al., 2010). For example, in a study of twenty healthy human participants given LSD, significant increases were found in all of the ASC subscales relative to placebo with the exception of anxiety which remained unchanged (Carhart-Harris et al., 2016c).

The complex nature of these changes in human consciousness presents challenges to the experimenter designing back-translational animal studies assessing behavioural change in response to psychedelics. Rats are capable of successfully discriminating 5-HT_{2A} agonists from saline and a variety of other psychoactive substances with discrimination tests used to screen substances for 5-HT_{2A} agonism in rats and mice (Appel et al., 2004). A few studies have been able to demonstrate complex shifts in perception, for example a study in rats demonstrated that DOI disrupts temporal discrimination in a 5-HT_{2A} receptor dependent manner (Asgari et al., 2006). A comprehensive evaluation of different rodent responses to 5-HT_{2A} drugs is presented in a review by Hanks (Hanks and González-Maeso, 2013).

The head twitch response (HTR) is commonly used as a rodent assay to test drugs for 5-HT_{2A} agonism and describes a rapid rotational head movement from side to side (Halberstadt and Geyer, 2013). The HTR is widely reproducible in mice and rats following administration of psychedelic drugs, and is believed to be 5-HT_{2A} dependent, as it is blocked by selective 5-HT_{2A} antagonists and is not present in 5-HT_{2A} receptor knockout mice (Canal and Morgan, 2012). Genetic dissection of the mechanism underlying how psychedelic drugs cause HTR in mice has shown that this is dependent on the expression of cortical 5-HT_{2A} receptors on glutamatergic neurons (González-Maeso et al., 2007). Coupled with earlier findings that direct injection of DOI into the medial prefrontal cortex results in dose-dependent expression of the

HTR, this suggests a key role for the prefrontal cortex in the expression of this behaviour (Willins and Meltzer, 1997).

The HTR can be easily observed from video (Canal and Morgan, 2012), however, the recording and rating of events is time intensive, although attempts have been made to automate measurement of the HTR using both magnetometer coils and high-speed video (Halberstadt and Geyer, 2013). The original video data was not available for the recording sessions analysed in this thesis, precluding manual scoring of the HTR from the video. Whilst automated analysis of high speed, high resolution video tracking data can be used to measure the HTR, the mean frequency of the HTR is approximately 90Hz and was therefore beyond the scope of the available tracking data for the present analysis (Halberstadt and Geyer, 2013). Whilst measurement of the HTR can be used to reliably identify whether a substance acts as a 5-HT_{2A} agonist or has psychedelic properties in humans it does not have a recognised analogue in human behaviour (Hanks and González-Maeso, 2013). Despite this, both HTR and subjective psychedelic effects in humans are induced by the same range of drugs, are both 5-HT_{2A} dependent, and both demonstrate rapid tolerance following repeated administration of psychedelics suggesting shared mechanisms (Buchborn et al., 2015).

Whilst evidence is building in support of psychedelic drugs having persistent antidepressant and anxiolytic effects, during acute treatment transient anxiety is recognised as a common side effect in human studies even when administered in a carefully controlled clinical setting (Andersen et al., 2020). In contrast to altered states of consciousness, this heightened anxiety may present opportunity for back-translation from animal models. In human studies, the acute effects of psychedelic drugs are often psychotomimetic, resulting in a mental state similar to that seen in acute psychosis. Healthy volunteers treated with LSD acutely experience large increases in scores on the psychotomimetic states inventory alongside more positive effects such as heightened mood (Carhart-Harris et al., 2016b). On follow up after acute administration, increased optimism and trait openness were measured, with no evidence of persistent changes in delusional thinking (Carhart-Harris et al., 2016b).

Recording sessions in the current study took place in a circular open field arena. Ambulation in an open field arena can be used to derive a wide range of metrics depending on the data collected and is commonly used to measure locomotion and anxiety-like behaviours in rodent studies (Seibenhener and Wooten, 2015). Using an automated behavioural pattern monitoring system comprised of open chamber with integrated nose pokes in the walls and floor, it has been shown that psychedelic drugs (DOI, LSD and others) result in decreased locomotor activity, decreased exploratory nose pokes and avoidance of the central portion of the chamber (Krebs-Thomson et al., 1998), all indicators of potentially increased anxiety. In

mice, transitions between anxiogenic central open field and the “safe” periphery are associated with well-mapped circuitry incorporating both amygdala and prefrontal cortex aligning with the recording sites used in this thesis (Likhtik et al., 2014, Padilla-Coreano et al., 2016).

In line with the existing literature, I hypothesised that 25I would result in a reduction of locomotor behaviour as measured by calculating movement speed. Given the acute psychotomimetic and anxiogenic effects of psychedelics I hypothesised that 25I would also result in a reduction in the time spent in the central zone of the open field.

3.2. Methods: Effects of 5-HT_{2A} drugs on behaviour

The data in this study was collected according to the approach described in Chapter 2. In brief animals were recorded during open field ambulation using an overhead visible light spectrum camera at 25fps frames per second at a resolution of 720x576 pixels. Neuralynx video tracking software was used to calculate and record the location and head direction of the animals in each frame of the video using the coordinates of red and green LEDs attached to the head stage. Video tracking data was available for the 25I injections for the cortico-limbic experiments, but not for the control injections. Video tracking data was available for both 25I and control injections in the cortico-striatal experiments.

Unfortunately, the original video footage was not available for any of the experimental sessions. Video footage from a contemporaneous control experiment using the same experimental apparatus and protocol was available from an animal from outside the present study. From analysis of this video recording, it was clear that it would not have been possible to resolve much more than was captured through the video tracking software due to recording with a visible light camera in a darkened room. An image from this video is shown in Figure 3.1 to illustrate the experimental setup.

Figure 3.1: Raw and enhanced video images from a contemporaneous control experiment to demonstrate the experimental setup

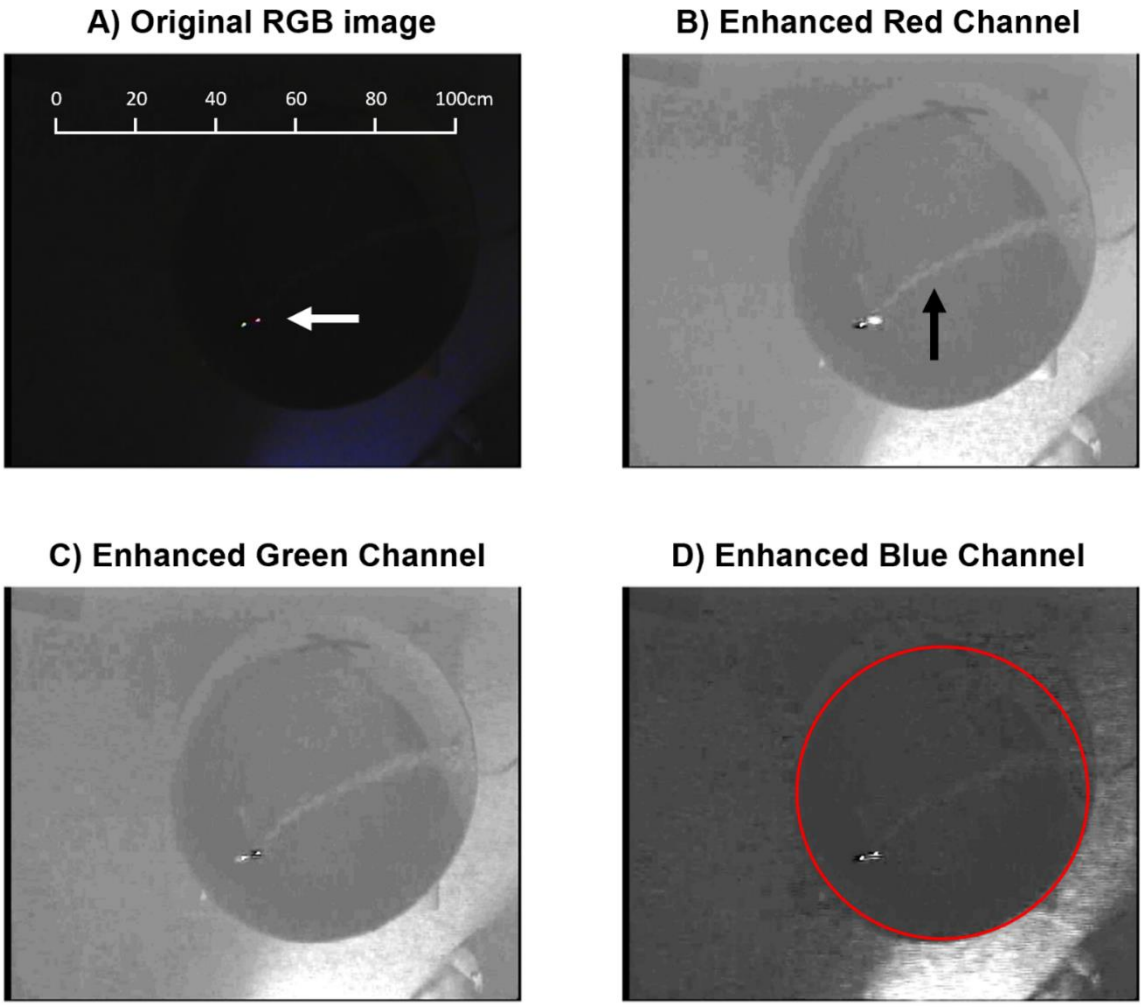

Although the original video from the experimental sessions was not available, recording from a contemporaneous set of experiments using the same apparatus and protocol was available. **A**: Raw video footage. The green and red LEDs (white arrow) on the head stage can be clearly seen on the otherwise dark image. The white scale bar at the top of the image shows the image scale for the four panels. **B-D**: show the red, green, and blue channels of the video respectively, with the red and green LEDs demonstrating greater intensity in their corresponding channels facilitating the tracking of head direction. In Panel B the black arrow marks the fine wire tether connecting the head stage to the recording equipment. In Panel D the red circle marks the boundary of the open field arena.

3.2.1. Processing of location data

To account for differences in camera position between experiments, the coordinates from the video tracking data were mapped to a 100x100 pixel grid using the boundary of the arena which was clearly visible from each set of tracking data. A circular mask of radius 50 pixels was applied (Shoelson, 2020), and missing location data was imputed with linear interpolation. For each frame of the video (25fps) the location of the animal was counted to generate a heatmap of each animal's location over the recording session.

3.2.2. Calculation of movement speed

Movement speed was calculated from the normalised location data. The animals' normalised location data was resampled to 1Hz and the movement speed was calculated at each time point using the distance travelled and the diameter of the open field arena (73.2cm). Speed data was filtered to account for when the animal was stationary, defined as movement of less than one normalised pixel per second, and to account for occasional tracking errors causing large spikes in the speed data (>60cm/s).

3.2.3. Time spent in central zone of open field

The central zone of the arena was defined as 40% of the open field arena by area in line with previously published studies using a circular open field (Likhtik et al., 2014). A circular mask was applied to the normalised location map with an area equal to 40.14% of the total number of pixels. The number of frames when the animal was in the central zone was counted and divided by the total number of datapoints recorded for that period to provide the percentage of time spent in the central area. The normalised grid and circular masks are show in Figure 3.2.

Figure 3.2: Diagram of normalised arena and central zone

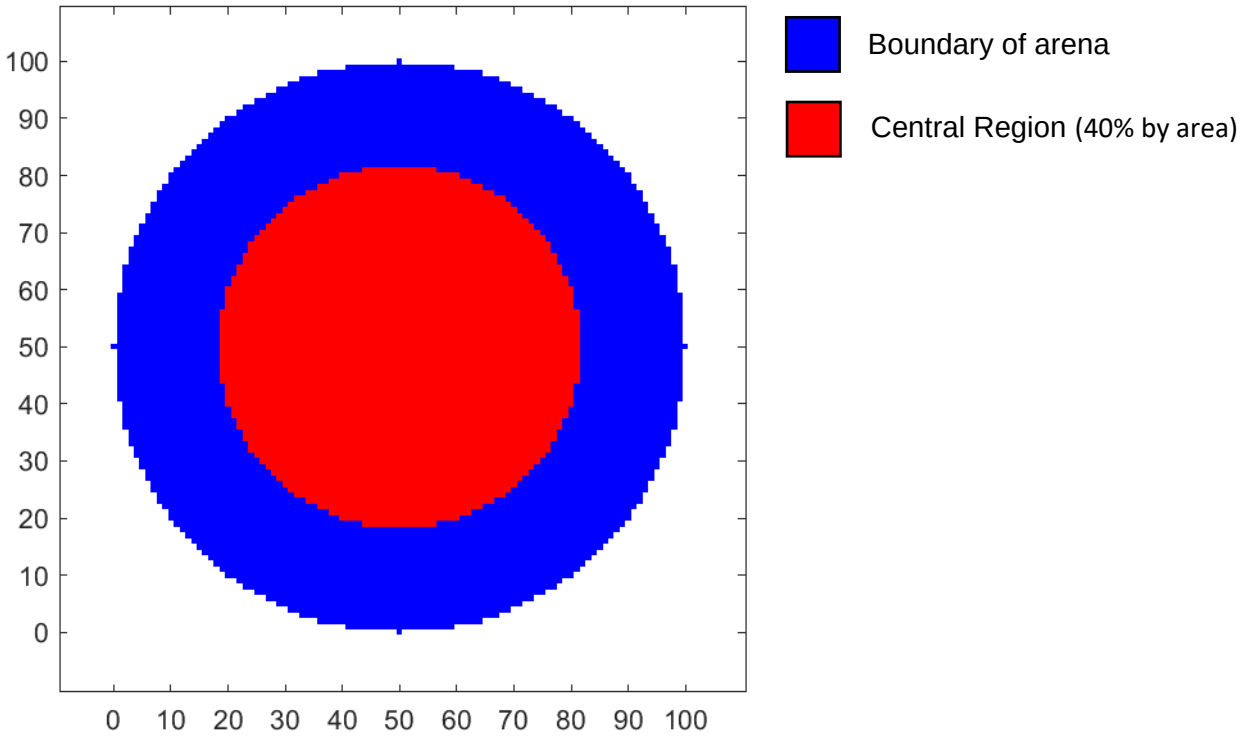

3.2.4. Statistical analysis

The effects of 25I on movement speed and open field ambulation relative to control were tested in the cortico-striatal rats (n=4) as control data was available. The mean movement speed and proportion of time spent in the central area of the open field for each rat were compared between 25I and control conditions across the baseline period (5-10 minutes prior to injection) and the post-drug period (5-40 minutes post injection). The periods used for comparison are illustrated graphically in Figure 3.3. Normality of mean data was checked for each condition and time period using the Shapiro-Wilks test. As no violations of normality were identified (defined as $p<0.05$ on the Shapiro-Wilks test) a repeated measures analysis of variance (ANOVA) was used to test whether 25I had a significant effect on movement speed or ambulation in the open field relative to control using the 'fitrm' and 'ranova' commands in MATLAB (Mathworks, Natick, MA) version 9.6.0.1072779 (R2019a). The Shapiro-Wilks test was performed using R statistical software version 3.5.3 with the 'shapiro-test' command (R Core Team, 2019).

3.3. Results

3.3.1. Movement speed decreased across both experimental conditions over the recording sessions

Figure 3.3 shows the movement speed against time for all recording sessions across both experiments. Changes in movement speed in the baseline and post-drug periods are summarised numerically in Table 3.1 and presented graphically using box plots in Figure 3.4. Whilst there were clear reductions in movement speed following injection of 25I in both groups, there were also reductions in movement speed following the control injections. Repeated measures ANOVA was performed on the data from the nucleus accumbens rats where 25I and control data was available; there was no significant effect of 25I relative to control on movement speed $F(1,6) = 0.04$, $p = 0.85$. These analyses indicate that 25I consistently reduced the movement speed of all rats, however, also demonstrated a tendency for animals to move less across the course of control recording session.

Figure 3.3: Graphs of movement speed over the duration of the recording period for 25I and control conditions

A: Data from cortico-limbic experiment in 25I condition

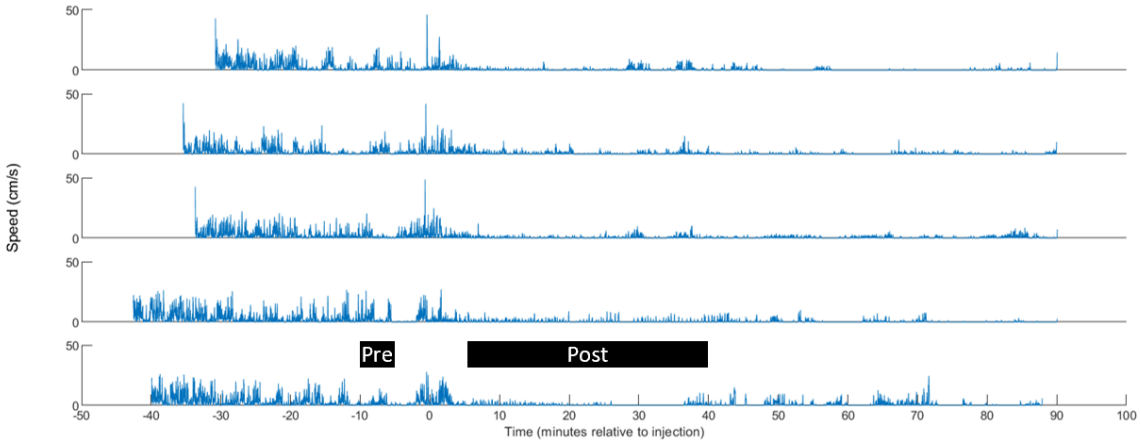

B_1: Data from cortico-striatal experiment in 25I condition

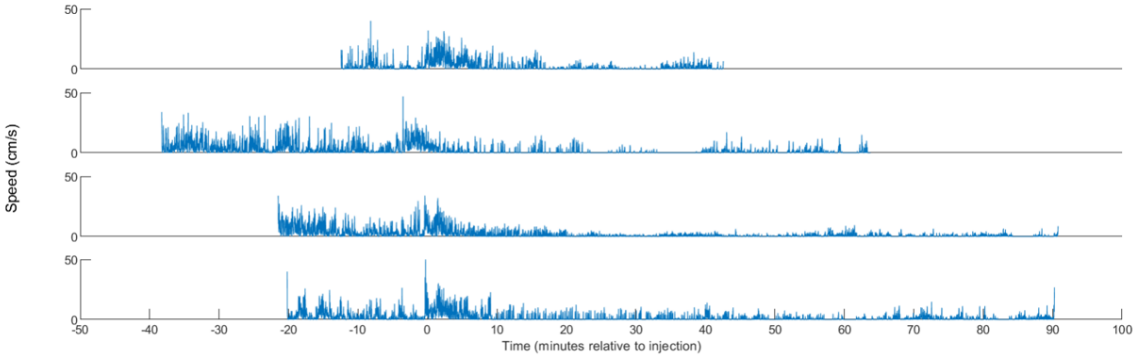

B_2: Data from cortico-striatal experiment in control condition

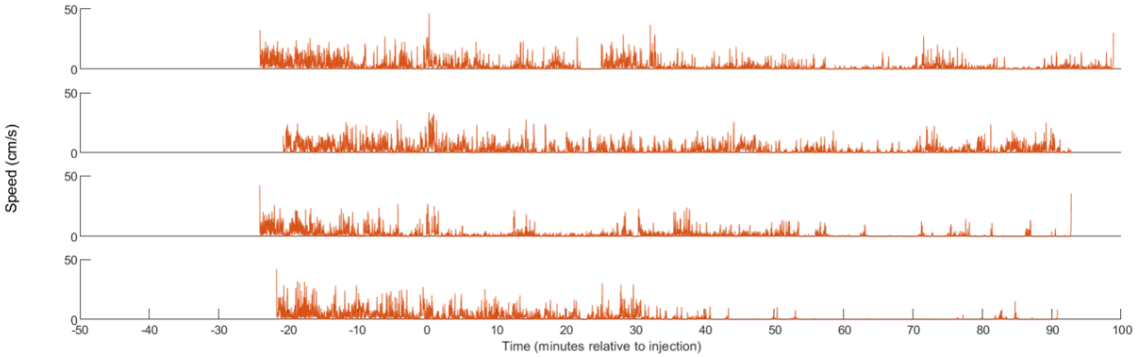

A: Movement speed plotted across the individual recording sessions for 5 rats in the cortico-limbic experiment. 25I was injected i.p. at a dose of 2mg/kg at Time 0. Time windows used for quantification of pre- and post-injection behaviours are marked by black horizontal bars in lower panel. **B:** Movement speed plotted across the individual recording sessions for 4 rats in the cortico-striatal experiment. **B_1:** In the 25I condition the drug was injected i.p. at a dose of 2mg/kg at time 0. **B_2:** In the control condition saline was injected i.p. 1ml/kg at time 0.

Table 3.1: Movement speed by experiment, time point and drug

Experimental Group	25I			Control		
	Baseline	Post-drug	Change	Baseline	Post-drug	Change
	Mean (SD) cm/s	Mean (SD) cm/s	Mean (SD) %	Mean (SD) cm/s	Mean (SD) cm/s	Mean (SD) %
Cortico-limbic (n=5)	1.9 (0.6)	0.5 (0.1)	-74.1 (8.2)	-	-	-
Cortico-striatal (n=4)	2.7 (0.4)	1.0(0.4)	-61.1 (13.5)	4.0 (1.5)	2.3 (0.6)	-38.3 (26.9)

Figure 3.4: Change in movement speed across conditions

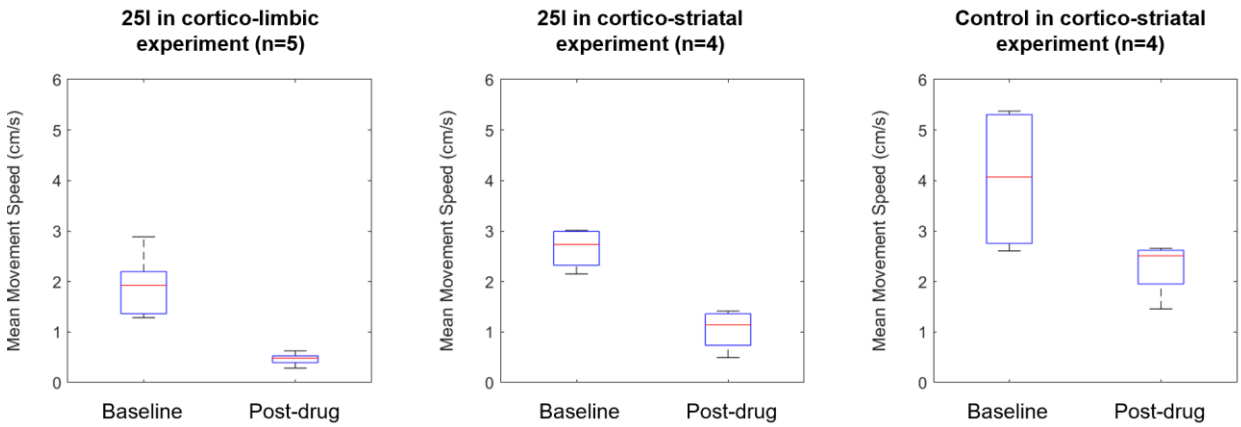

Red central lines indicate the median; upper and lower bounds of the box indicate 25th and 75th percentiles respectively. Whiskers show the range of the data excluding outliers defined as datapoints that are more than 1.5 times the interquartile range from the 25th or 75th percentiles. Red crosses indicate outlying data.

3.3.2. 25I causes visible changes in locomotion pattern

Figure 3.5 shows the location data for all recording sessions across both experiments in the form of a heatmaps depicting how frequently an animal was recorded at each location. This data was used to calculate the percentage of time the animal spent in the central zone of the open field as described in section 3.2.3. Changes in the percentage of time spent in the central zone of the open field arena for the baseline and post-drug periods are summarised numerically in Table 3.2 and graphically using box plots in Figure 3.6. Whilst there were reductions in the percentage of time spent in the central field following injection of 25I in both groups, there were also reductions following the control injections. Repeated measures ANOVA was performed on the data from the nucleus accumbens rats where 25I and control

data was available. Similarly to movement speed, there was no significant effect of 25I relative to control on percentage of time spent in the central area $F(1,6) = 1.94$, $p = 0.21$.

Whilst administration of 25I did not have a significant effect on the percentage of time spent in the central area, there were visible differences in the patterns of behaviour shown in Figure 3.5B. Comparison of the post-drug heatmaps for individual animals suggests that animals given a control injection appear to show broader exploration of the peripheral zone of the field relative to those given an injection of 25I and appear to be entering the central field more frequently.

Table 3.2: Percentage of time spent in central zone of open field arena

Experimental Group	25I			Control		
	Baseline	Post-drug	Change	Baseline	Post-Drug	Change
	Mean % (SD)	Mean % (SD)	Mean % (SD)	Mean % (SD)	Mean % (SD)	Mean % (SD)
Cortico-limbic (n=5)	20.1 (31.6)	4.6 (5.1)	-15.5 (34.5)	-	-	-
Cortico-striatal (n=4)	24.3 (6.3)	7.9 (3.5)	-16.4 (5.5)	22.8 (6.5)	14.1 (6.8)	-8.6 (9.8)

Figure 3.6: Change in time spent in central area of arena

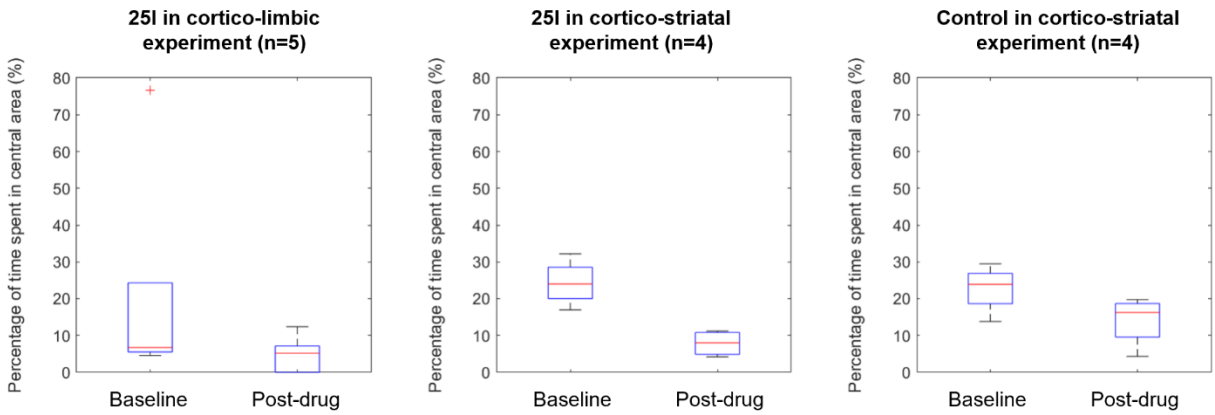

Red central lines indicate the median; upper and lower bounds of the box indicate 25th and 75th percentiles respectively. Whiskers show the range of the data excluding outliers defined as datapoints that are more than 1.5 times the interquartile range from the 25th or 75th percentiles. Red crosses indicate outlying data.

Figure 3.5: Heatmaps to show edge preference and location of rats over time for 25I and control conditions

Coordinates from video tracking data were mapped to a normalised grid representing the interior of the open field arena. For each frame of the video (25fps) the location of the animal was marked on the heatmap. The colours represent the number of times an animal was recorded at a given location during the time window according to the colour scale at the bottom of each panel. **A:** Heatmaps for the pre and post injection period in 25I condition from the cortico-limbic experiment (n=5). **B:** Heatmaps for the pre and post injection period in both control and 25I condition in the cortico-striatal experiment (n=4). Control data was only available for the animals in the cortico-striatal experiments. Please note when interpreting these figures that the pre-drug period was of 5 minutes duration and the post-drug period was 35 minutes duration.

A: Data from cortico-limbic experiment

25I : Baseline period (5 – 10 minutes pre-injection)

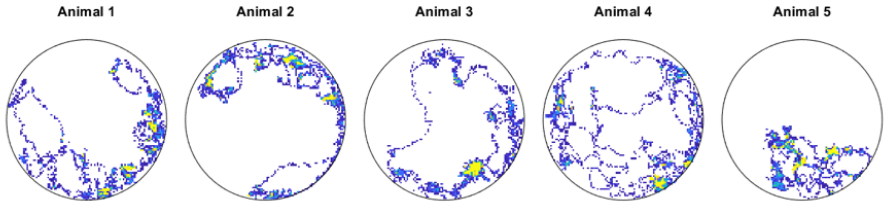

25I : Post-drug period (5 – 40 minutes post-injection)

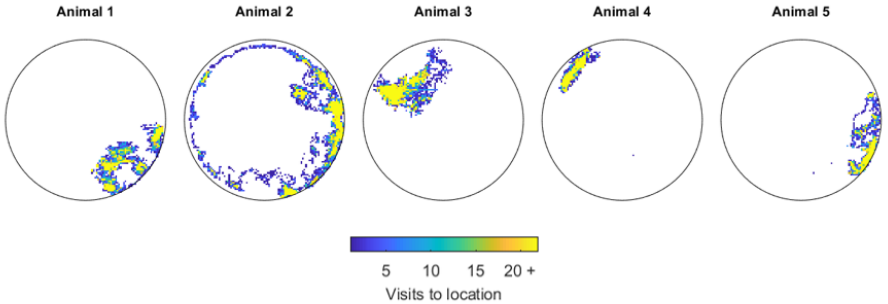

B: Data from cortico-striatal experiment

Saline : Baseline period (5 – 10 minutes pre-injection)

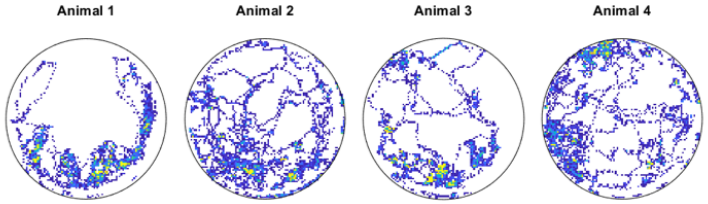

Saline : Post-drug period (5 – 40 minutes post-injection)

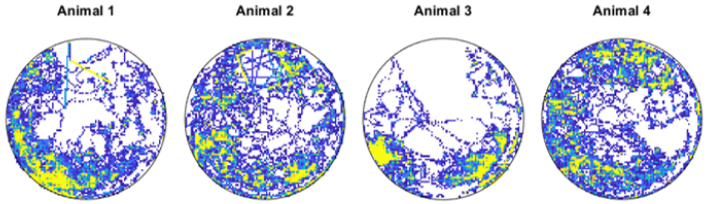

25I : Baseline period (5 – 10 minutes pre-injection)

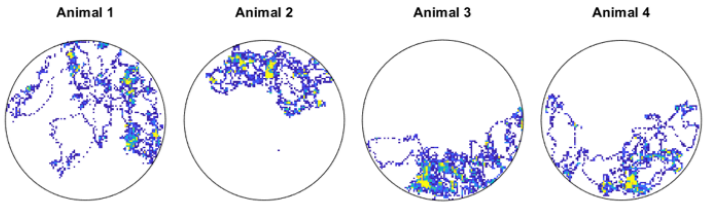

25I : Post-drug period (5 – 40 minutes post-injection)

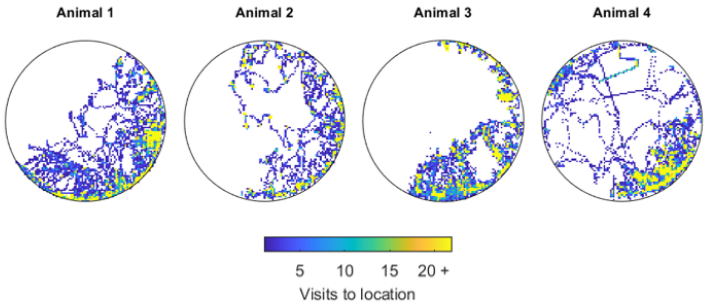

3.4. Discussion

3.4.1. Key findings

In the present analysis, 25I did not show a statistically significant effect on movement speed or the percentage spent in the central areas of the open field arena relative to control. Whilst there were clear reductions in both metrics following 25I injection, these effects were not significantly different from the changes following the control injection.

Visual inspection of the heatmaps for the post-drug period across the 25I and control conditions is suggestive of variation in the underlying behavioural patterns. Changes in the behavioural patterns generating the heatmaps in this study may prove discernible with more nuanced analysis of the behavioural data, and/or with more statistical power and larger group sizes.

3.4.2. Comparison with existing literature

To the best of my knowledge, the behavioural effects of 25I (a highly selective 5-HT_{2A} agonist) have not previously been described in freely behaving rats. Multiple studies have shown administration of psychedelic drugs (non-selective 5-HT_{2A} agonists) including DOI and LSD results in reduced locomotion behaviour in rats, and avoidance of novel and open areas (Adams and Geyer, 1985, Krebs-Thomson et al., 1998, Krebs and Geyer, 1994). Despite replication, these findings are not universally reported. A study testing the behavioural effects of LSD found short term increases in locomotor behaviour over the first 5 to 25 minutes, with this increase in locomotion blocked by pre-treatment with a selective 5-HT_{2A} antagonist (Ouagazzal et al., 2001). In a study using 2C-B (a psychedelic drug with mixed 5-HT_{2A} and 5-HT_{2c} activity) a biphasic effect was reported, with initial reductions in locomotion followed by subsequent increases in locomotion and activity (Páleníček et al., 2013). Avoidance of the central zone of an open field arena is commonly used as a measure of anxiety-related behaviour (Carola et al., 2002) and the avoidance of open areas seen with LSD would suggest increased levels of anxiety (Krebs-Thomson et al., 1998). Despite this, there appears to be variation in the response to psychedelic drugs depending on the measures of anxiety used, with some studies reporting report anxiolytic effects for agents including DOI (Nic Dhonnchadha et al., 2003, Hawkins et al., 2002). It is important to note that the pharmacodynamics and pharmacokinetics of 5-HT_{2A} agonists vary considerably complicating direct comparisons across studies.

3.4.3. Limitations

The work presented in this chapter was limited by two major issues: the small number of animals for which complete video tracking data was available and the limitations of coordinate-based head tracking data over high-resolution video. In comparison to the electrophysiological data presented in the subsequent chapters, the video tracking data is relatively low resolution without the availability of the original video footage. If I were to undertake further experiments using the present approach, I would ensure that video tracking is accompanied by recording with an infrared camera. The missing video tracking data for the control amygdala experiments impacted on the ability to conduct significance testing in that experimental group and meant that it was not possible to pool data to increase statistical power. Although the cortico-limbic and cortico-striatal experiments used different strains of rat (Wistar and Lister Hooded rats respectively) it may have been feasible to successfully pool the data by including the strain as a covariate in the statistical analysis.

The reduction in movement speed and the reduction of time spent in the central zone of the open field in the control group were not anticipated in advance and significantly reduced the power of the study to detect significant effects of 25I. Protocols to assess anxiety in open field exploration differ, with some studies brightly lighting the open field resulting in increased baseline anxiety (Likhtik et al., 2014), and other studies only recording behaviour when the animal is placed in the arena before habituation to the environment has occurred (Gould et al., 2009). Given the primary outcome of these experiments was to record the electrophysiological effects of 25I the focus was on ensuring that distress was kept to a minimum in order to record the physiological response of the animals to the drug without additional stress. As such, the animals were habituated to the open field daily for a week prior to recording and were habituated to the arena for 30 minutes prior to administration of intraperitoneal injections. This process of prolonged habituation may have resulted in attenuation of the behavioural effects of 25I but was essential to ensure the electrophysiological data presented in the subsequent chapters reflects the effect of 25I without the additional of additional stressors.

3.4.4. Further work

Analysis of exploration in an open field arena can be performed using many approaches and it may be that the metrics chosen of movement speed and time spent in the central zone were not sufficiently sensitive to detect the changes in behaviour. Alternative measures that could have been used include frequencies of entry into the central zone or edge zone or measuring entries into central zone followed by immediate return. The open field can also be divided up

into squares or segments to measure the number of segments entered in the either the central or edge zone (Carola et al., 2002). Other authors have introduced greater complexity into the open field itself, for example the addition of nose poke holes and additional sensors to characterise increasingly complex patterns of behaviour (Krebs-Thomson et al., 1998). On review of the data presented above I would consider the use of segment crossing and entry-based measures in future studies; however, these metrics are usually defined as the crossing of a boundary with all four paws which cannot be ascertained from head tracking data alone.

Many of the current approaches to analysis of open field behaviour also make use of ethological measures of behaviour including patterns of rearing, grooming, stretching, sniffing and defecation (Carola et al., 2002). Detection of these behaviours is possible with video analysis and has the potential to be automated for analysis of large datasets using tools such as DeepLabCut (Mathis et al., 2018). Given the broad and complex nature of the changes to human subjective experience reported with psychedelic drugs (Carhart-Harris et al., 2016c), it is likely that a combination of approaches to behavioural testing would be most appropriate to capture the effects of psychedelic drugs.

Recent developments in computational methods have allowed for the development of model-free approaches to the analysis of animal behaviour. One example of a model-free approach to behavioural analysis is MoSeq, which uses computational analysis of depth camera data to deconstruct complex patterns of animal behaviour into constituent motifs (Wiltschko et al., 2015). This approach has been used to link behavioural motifs identified by computational decoding of depth camera data, with the spiking patterns of neurons in the dorsolateral striatum and provide a potential bridge between behavioural and neural information (Markowitz et al., 2018). Given that psychedelic drugs appear to disrupt temporal perception (Asgari et al., 2006) and cause broad patterns of behavioural disorganisation (Krebs-Thomson et al., 1998) the exploration of behavioural changes from the perspective of motion sequencing may be of particular interest.

Chapter 4. The neurophysiological effects of 5-HT_{2A} activation on cortico-limbic and cortico-striatal network dynamics

4.1. Introduction

As outlined in Chapter 1, LFP signals recorded from implanted, intracranial microelectrodes provide insights into the coordinated activity of neuronal populations, and how this activity alters in response to experimental conditions. In this chapter, the effects of 25I on LFP in the prefrontal cortex, hippocampus, basolateral amygdala, and nucleus accumbens are quantified using spectral analysis and functional connectivity approaches.

4.1.1. Spectral analysis of neural population activity

Spectral analysis is an approach to describing a signal based on the decomposition of the full band signal into its amplitude for each of its constituent frequencies and, in neuroscience, is commonly applied to LFP, EEG and MEG signals. In this chapter I primarily use multi-taper spectral analysis for the calculation of spectral power. The theory, background and general approach of multi-taper spectral approaches in EEG is reviewed by Perau et al. and is equally applicable to LFP data (Prerau et al., 2016). There are alternatives to the multi-taper approach including auto-regressive models with each approach having proponents (Muthuswamy and Thakor, 1998). Indeed, the approach used to calculate Granger causality in this thesis (outlined in section 4.2.4) is based upon vector auto-regression (VAR) models.

Analysis of spectral power across frequency bands provides an approach to quantify changes in spectral power and describe the oscillatory patterns present in a region in different states. Oscillations in specific frequency bands are related to specific patterns of neuronal activation and inhibition (Buzsáki and Wang, 2012), and are associated with different neural states such as wakefulness and sleep (Prerau et al., 2016). Spectral signals are proposed to be more than the incidental product of underlying neural processes, and may be a key component of neural computation in their own right by enabling synchronisation of neural processes across neuronal populations and brain regions (Fries, 2009). A summary of the frequency bands used for the analysis in this chapter is shown in Table 4.1.

Table 4.1: Frequency bands used for spectral analysis

Band	Abbreviation	Frequency Range (Hz)	Primary physiological association
Delta	δ	1-4	Occur during waking; role in hippocampal and prefrontal synchronisation in rats (Fujisawa and Buzsáki, 2011)
Theta	θ	6-10	Predominant feature of network activity in the hippocampus during exploration and during alert states(Buzsáki, 2002); also frontal midline theta associated with working memory (Mitchell et al., 2008)
Beta	β	15-30	Role in rodents unclear; aberrant beta oscillations seen in Parkinson's disease (Little and Brown, 2014)
Low Gamma	γ_{Low}	30-48	Likely reflects synchronised neuronal computation (Fries, 2009)
High Gamma	γ_{High}	52-100	As above
High Frequency Oscillations	HFO	125-170	Hippocampal ripples (occur in brief bursts); cortical ripples recently identified (McKenzie et al., 2020); broader role unknown

4.1.2. Known spectral effects of 5-HT_{2A} agonists

The spectral effects of 5-HT_{2A} agonists have previously been measured on LFP in rats and mice (Wood et al., 2012, Goda et al., 2013, Dimpfel et al., 1989, Páleníček et al., 2013, Riga et al., 2018), on spiking patterns in neurons in rats (Puig et al., 2003, Puig et al., 2010, Celada et al., 2008) and in cortical slice physiology (Lambe and Aghajanian, 2007). In humans spectral effects have been measured in EEG (Riba et al., 2004, Timmermann et al., 2019) and MEG studies (Muthukumaraswamy et al., 2013, Carhart-Harris et al., 2016c),

An early comparison of the spectral changes seen with 5-HT_{2A} agonists compared psychedelic amphetamine derivatives (DOI and related compounds), with stimulatory amphetamine derivatives including 3,4-Methylenedioxymethamphetamine (MDMA) on their effects on spectral power in freely moving rats (Dimpfel et al., 1989). This study recorded LFP from frontal cortex, hippocampus, striatum and the reticular formation. The authors identified an increase of power in the alpha band (9.75-12.5Hz) that was particularly pronounced in the striatum, providing early evidence for the importance of the cortico-striatal circuit in the action of psychedelics. A role for the striatum has also been implicated in the work from the lab of Hunt, who identified HFO in the nucleus accumbens in response to subanaesthetic ketamine (Hunt et al., 2006). This work was subsequently extended by looking at the effects of LSD and DOI which demonstrated increased gamma (40-90Hz) oscillations and HFO in the rat nucleus accumbens (Goda et al., 2013), although the increases in HFO were less pronounced than seen with ketamine.

DOI administration results in mixed effects on the firing of projection neurons in the prefrontal cortex, with both increases and decreases in pyramidal projection neuron firing; and results in increased local 5-HT release and activation of dorsal raphe neurons (Puig et al., 2003). These findings have been reproduced in other studies, with disruption of the normal relationship between the discharge of pyramidal neurons and phase also reported (Celada et al., 2008). In rats DOI has been shown to cause a dose-dependent reduction in neuronal firing in the prefrontal cortex, with reduced spectral power in the low gamma frequencies and to a lesser extent in high gamma frequencies (Wood et al., 2012). There is evidence for reduced delta (0.3-4Hz) activity in prefrontal cortex in rats following DOI with reversal of this finding following treatment with the antipsychotic drugs, haloperidol and clozapine (Celada et al., 2008). Some studies have shown increases in oscillatory power in the prefrontal cortex, with wild- type mice showing increased theta and gamma power in the medial prefrontal cortex following 5-MeO-DMT (Riga et al., 2018). When DOI is applied to a bath containing coronal slices of the medial prefrontal cortex of young adult rats, there is an increase in the probability of recurrent network activity following an electrical stimulus or electrolyte manipulation, with self-oscillatory behaviour occurring in the gamma range at 30-80Hz (Lambe and Aghajanian, 2007).

In one human EEG study of intravenous DMT there were clear reductions in the alpha and beta bands throughout the study (Timmermann et al., 2019). The authors also looked at the time course and saw initial decreases in delta and theta bands for the first minute post DMT, with recovery of delta back to baseline and increases in theta from baseline after the first minute which correlated with subjective reports of the peak experience (Timmermann et al., 2019). A human EEG study using the traditional preparation of Ayahuasca, a herbal drink containing both DMT and monoamine oxidase inhibitors, demonstrated decreases in absolute

power across all frequency bands, with the most prominent reduction in theta, accompanied by relative increases in beta power (Riba et al., 2002).

In an MEG study in humans, psilocybin resulted in broadband reductions in spontaneous cortical oscillations up to 50Hz with large decreases noted in the default mode network (Muthukumaraswamy et al., 2013). These findings were extended by combination with MEG data on LSD and ketamine against both placebo and active control (Barnett et al., 2020). Psilocybin, LSD and ketamine showed decreases in power across all frequency bands, that were particularly pronounced in alpha and beta (Barnett et al., 2020). A study using an overlapping human MEG dataset employed multivariate machine learning classifiers to identify differences between the spectral effects of psilocybin, LSD, and ketamine and found reduced low beta power with all three drugs and decreases in low alpha and theta frequencies with psilocybin and LSD that were not seen with ketamine (Pallavicini et al., 2019).

Although the drugs, doses and conditions in the above studies vary widely, taken together the rodent data highlights increases in oscillatory power in the nucleus accumbens across multiple frequencies and likely reductions in power in the prefrontal cortex. The available human data is collected from EEG and MEG recordings, and as such is limited to reporting cortical activity. None of the human studies measure effects at high gamma or HFO frequencies, in part due to the limitations of current EEG and MEG techniques. The human data that is available consistently shows broadband decreases in cortical spectral power across a wide variety of 5-HT_{2A} agonists (Timmermann et al., 2019, Muthukumaraswamy et al., 2013, Barnett et al., 2020, Riba et al., 2002).

4.1.3. What is functional connectivity?

Spectral analysis of LFP signals can provide insight regarding rhythmic synaptic population activity at a local level; however, neuronal populations do not act in isolation. Examination of the associations between spectral processes in different brain regions can provide insights into the underlying computational processes (Siegel et al., 2012). Psychiatric diseases are increasingly being recognised as disorders of network dysconnectivity, whether through areas being too tightly coupled, or not coupled enough (Godsil et al., 2013, Friston et al., 2016, Kupferschmidt and Gordon, 2018). In this chapter the coordination between neuronal populations in the cortico-limbic and cortico-striatal pathways is explored using functional connectivity analysis.

Functional connectivity describes statistical relationships between neuronal signals recording at different locations in the brain (Bastos and Schoffelen, 2016). Functional connectivity analysis is commonly applied to fMRI, EEG, MEG and LFP data. There are many metrics that

have been used to calculate functional connectivity in neuroscience, each of which has advantages and disadvantages (Bastos and Schoffelen, 2016). Measures of functional connectivity alter with changes in network activity and these changes can be measured in response to a wide range of experimental paradigms.

Different measures of functional connectivity describe different kinds of statistical associations between neural data and can be used in combination to make inferences about network activity. Functional connectivity metrics can be divided into undirected and directed connectivity depending on whether the metric describes association or describes the direction of signal flow. Undirected measures of functional connectivity (such as correlation and coherence) are symmetrical, in that the relationship is the same whether calculated from A to B or from B to A. In contrast, directed measures of functional connectivity are non-symmetrical and provide different values for the relationship from A to B and from B to A.

Functional connectivity metrics can also be divided based on whether they describe data in the time-domain, or the frequency domain by taking into account the spectral composition of the signals. In this chapter I present both time and frequency domain analyses and compare the differences in the results generated by each approach.

The application of pairwise measures of functional connectivity can yield incorrect results when applied to an interconnected system (Kuś et al., 2004). The calculation of a pairwise functional connectivity measure between variables X and Y can lead to spurious relationships, where both variables are dependent upon a third variable Z (Barnett and Seth, 2014). Multivariate approaches to functional connectivity have been developed for use with multivariate datasets such as EEG or implanted electrodes, where comparisons will be made between recordings from multiple related regions (Barnett and Seth, 2014, Oostenveld et al., 2011, Rosenberg et al., 1998). A (non-exhaustive) summary of functional connectivity metrics covering those used in this chapter is shown in Table 4.2.

Table 4.2: Summary of functional connectivity metrics

Type of measure	Undirected FC		Directed FC	
	Bivariate	Multivariate	Bivariate	Multivariate
Time Domain	Correlation	Partial correlation	Unconditional time domain Granger causality	Conditional time domain Granger causality
Spectral Domain	Coherence	Partial coherence	Unconditional frequency domain Granger causality	Conditional frequency domain Granger causality

Undirected measures of functional connectivity

The simplest measure of functional connectivity is the correlation, with correlation coefficients describing the direction and strength of linear relationship between two variables. Correlation coefficients describe the relationship between two variables in the same way that a regression coefficient describes the relationship in a simple linear regression. The multivariate equivalent of correlation is the partial correlation. The partial correlation coefficient is equivalent to a regression coefficient from an adjusted linear regression and describes the strength of the relationship between two variables, whilst adjusting for the relationship with other variables that are included in the regression.

Where correlation gives a single value for the relationship between two timeseries in the time domain, coherence measures the relationship between two timeseries in the frequency domain and describes the phase relationship between constituent frequencies (Gardner, 1992). Coherence magnitude is valued between zero and one with one describing a perfect linear relationship between phase at a given frequency range and zero describing timeseries with no linear phase relationship. The phase of the coherence can be interpreted as the time lag between the two timeseries at a given frequency (Granger, 1969). As with partial correlation, the partial coherence can be calculated taking into account the relationships between multiple timeseries and minimises the impact of shared dependence upon other measured variables (Rosenberg et al., 1998).

Directed measures of functional connectivity

Granger causality (GC) was originally developed in economics as an approach to measure the temporal association between two time series (Granger, 1969) and measures the 'precedence' in time of one signal over another (Leamer, 1985). A signal (S_1) is said to Granger cause a signal (S_2) if the past values of S_1 and S_2 are better able to predict the future value of S_2 than the past values of S_2 alone. The development of the application of Granger causality in neuroscience is comprehensively reviewed by Seth (Seth et al., 2015). In this thesis I use the approach of Barnett and Seth which allows for calculation of multivariate pairwise conditional Granger causality in both the time and frequency domain (Barnett and Seth, 2014). Aside from Granger causality, a variety of other measures of directed functional connectivity are also available although are beyond the scope of this thesis (Bastos and Schoffelen, 2016).

4.1.4. Known effects of 5-HT_{2A} on functional connectivity

In rats, Granger causality has been used to demonstrate that HFO induced by ketamine appear to have a source in the olfactory bulb which drives the HFO seen in the nucleus accumbens (Hunt et al., 2019). The source of the HFO induced by 5-HT_{2A} agonists is yet to be reported, as is the downstream flow of HFO from the nucleus accumbens. In a study using the psychedelic drug 2C-B in rats, low doses caused global decreases in EEG coherence, while high doses showed dissociable effects by frequency with reductions in coherence in low frequencies and an increase in interhemispheric frontotemporal and frontoparietal coherence (Páleníček et al., 2013).

Much of the literature on the effects of 5-HT_{2A} agonists on functional connectivity comes from human studies using either MEG or fMRI. MEG studies are limited to providing insights about cortical connectivity, whilst fMRI studies are limited in the temporal resolution Blood-oxygen-level-dependent (BOLD) imaging can offer.

A comprehensive recent analysis of MEG data from human subjects treated with LSD, psilocybin, ketamine and active placebo has shown global decreases in cortical directed functional connectivity for LSD, psilocybin and ketamine. In the case of LSD, the authors of this study found an corresponding unexpected increase in undirected functional connectivity as measured with correlation and coherence (Barnett et al., 2020). Administration of psilocybin in a resting state fMRI study demonstrates marked reorganisation of network topology, with a shift from local intracortical functional connectivity under the placebo condition to long range intra-regional functional connectivity in the drug condition (Petri et al., 2014).

4.1.5. Aims of this chapter

In this chapter I test the hypotheses that 5-HT_{2A} receptor activation by 25I would result in increases in spectral power in the HFO and gamma band in the nucleus accumbens, amygdala and prefrontal cortex. I next test the hypothesis that 25I causes increases in both directed and undirected functional connectivity between regions using both time and frequency domain measures of functional connectivity. Finally, using band limited frequency domain Granger causality, I test the hypothesis that HFO were most likely to originate in a single region or regions from which they propagate throughout the cortico-striatal and cortico-limbic systems.

Alongside testing these hypotheses, a further aim was to develop a robust analysis pipeline for the characterisation of pharmacological changes in cortico-limbic, cortico-striatal and cortico-hippocampal, functional connectivity in rats as measured from implanted electrode arrays.

4.2. Methods

The data presented in this chapter was collected according to the general methods outlined in Chapter 2. An overview of the complete analysis pipeline is presented in Figure 4.1. This methods section describes the methods used for pre-processing of the LFP data, spectral analysis and functional connectivity analysis and the respective statistical analysis.

4.2.1. Software

The analysis presented in this section was implemented in MATLAB (Mathworks, Natick,MA) version 9.6.0.1072779 (R2019a) and R version 3.53 (R Core Team, 2019). A variety of toolboxes are available for the processing and analysis of LFP data (Unakafova and Gail, 2019). For the spectral and functional connectivity analysis presented in this thesis three MATLAB based toolboxes were used: Chronux (Bokil, 2008, Mitra Lab), Fieldtrip (Oostenveld et al., 2011) and the Multivariate Granger causality (MVGC) Toolbox (Barnett and Seth, 2014).

4.2.2. Pre-processing

Data was imported into MATLAB using the routines provided by the manufacturer of the data acquisition hardware (Neuralynx, USA). Electrophysiological data was centred on the injection time and divided into 5-minute epochs. Spectrograms were plotted of the full dataset for each animal, condition, and brain region to visualise the data prior to further analysis.

Further analysis was based upon 3 periods of interest as outlined in Section 2.2.6. These were a baseline period (5-10 minutes prior to the injection), an early post-drug period (5-10 minutes post injection) and a late post-drug period (35-40 minutes post injection). These time windows are highlighted graphically with red bars on the spectrogram for PRL in Figure 4.7.

Removal of artefacts

Within each of the periods of interest (baseline, early post-drug and late post-drug) the LFP data was divided into 2 second epochs and manually screened to remove epochs containing movement or recording artefacts. Artefacts were removed by visual inspection of LFP traces, total power, and power spectra data using a graphical user interface. The number of traces removed/kept are shown in Table 4.3.

For animals 2 and 4 in the cortico-striatal experiments there were high levels of artefact in the late post-drug period following 25I. Data from an adjacent 5-minute period where there were less artefacts present were therefore taken forward for analysis. For rat 2 this was from the period 40-45 minutes post-drug; and for rat 4 this was from the period from 30-35 minutes post-drug.

Table 4.3: Number of epochs remaining by animal and epoch after removal of epochs containing artefacts

Animal	Control			25I		
	Baseline	Early post-drug	Late post-drug	Baseline	Early post-drug	Late post-drug
Cortico-limbic 1	144	142	140	133	142	137
Cortico-limbic 2	132	135	122	148	146	148
Cortico-limbic 3	139	138	113	141	148	145
Cortico-limbic 4	118	120	99	141	130	140
Cortico-limbic 5	136	137	140	121	127	123
Cortico-striatal 1	89	102	137	101	130	133
Cortico-striatal 2	123	137	147	78	96	138
Cortico-striatal 3	133	128	136	131	140	120
Cortico-striatal 4	94	96	78	82	56	52

Downsampling

Data was downsampled to 400Hz for the calculation of power spectra, partial correlation, and partial coherence. Down sampling was performed using the 'spm_eeg_downsample' command from Statistical Parametric Mapping 12 (SPM12), a toolbox implemented in MATLAB and used primarily for the effective connectivity analysis presented in Chapter 5 (Moran et al., 2013).

Filtering of line noise

Filtering was performed to remove line noise prior to calculation of spectrograms, power spectra, partial correlation, and partial coherence. This was performed using a digital second order infinite impulse response (IIR) notch filter calculated with the 'iirnotch' command in MATLAB with a frequency of 50Hz and a Q factor of 70. This was applied to the data using zero-phase digital filtering with the 'filtfilt' command in MATLAB.

Figure 4.1: Overview of analysis pipeline for electrophysiology and functional connectivity

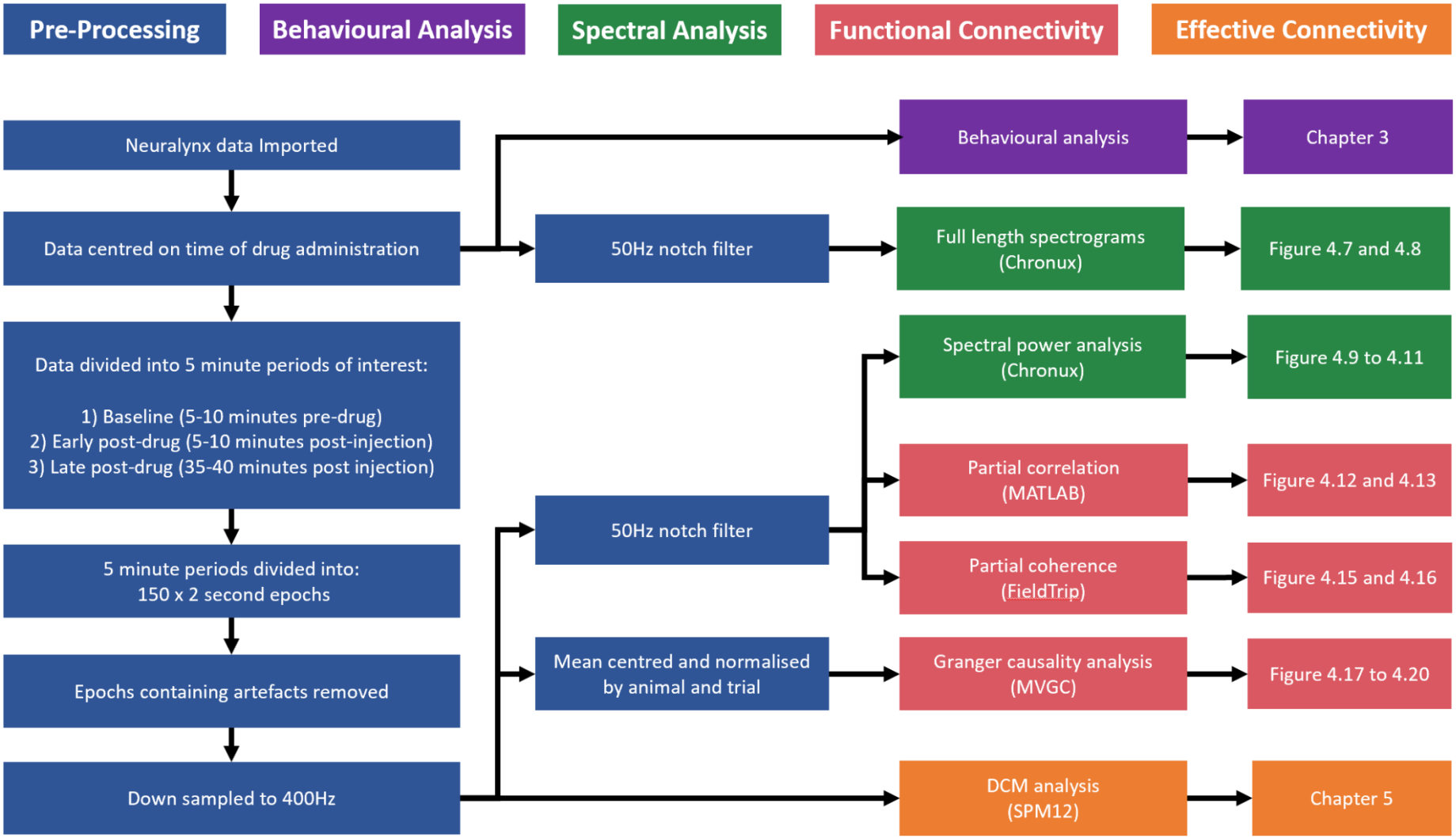

4.2.3. Spectral analysis

In this chapter spectral analysis was performed using Chronux version 2.12 v03 (Bokil, 2008, Mitra Lab). The Chronux toolbox uses multi-taper methods for calculation of spectrograms and power spectra. Using the multi-taper spectral approach in Chronux requires selection of the number of tapers based on the time-bandwidth product (Prerau et al., 2016). The parameters used for the Chronux routines are listed in Table 4.1. Standard plotting functions in MATLAB were used to visualise the outputs.

Multi-taper spectral analysis is based upon the premise that a stationary time domain signal can be decomposed into a series of sine waves at specific frequencies using the Fourier transformation (Prerau et al., 2016). For a time series to be stationary, the statistical properties of the time series must remain fixed over time, with shorter time windows increasing the likelihood of stationarity. Spectral estimates from discrete periods of data are prone to bias due to the truncation of the signal at beginning and end; to reduce this bias a tapering function can be applied to the data that tapers the signal at each end and reduces the magnitude of the bias. This approach was further developed by Thomson who introduced multi-taper spectral analysis (Thomson, 1982). Multi-taper spectral analysis employs a set of orthogonal tapers which are multiplied by the signal prior to Fourier transformation to provide independent spectral estimates from a single sample. The individual tapers are then averaged to give a single estimate of the spectrum with reduced variance and bias. Multi-taper methods are commonly employed in neuroscience as they enable accurate calculations of spectra from short periods of data. By applying these approaches to short windows of LFP data, the oscillatory activity from a region can be described over time using a spectrogram.

Spectrograms were calculated using the ‘mtspecgramc’ command for continuous data on the full length, full bandwidth recordings with a 50Hz notch filtering applied to remove line noise.

Power spectra were calculated for the baseline, early post-drug and late post-drug periods. Each period was divided into 2 second epochs and any epochs containing artefacts were removed. Data was down sampled to 400Hz and 50Hz notch filtering was applied. Power spectra were calculated using the ‘mtspectrumsegc’ command for continuous data and averaged across epochs for each animal and period. For graphical presentation power spectra were Z scored for each animal and condition across the three time points so that relative changes in power can be visualised across time. The mean power was calculated for each animal for each of the frequency bands of interest (Table 4.1) to statistically test for differences between 25I and control.

Table 4.4: Chronux parameters used for analysis

Parameter	Abbreviation	Spectrograms	Power Spectra
Tapers	Params.tapers	[1 5 1]	[1 5 1]
Sampling Frequency (Hz)	Params.Fs	Sample rate of recording (1010Hz or 1017Hz)	400
Frequency Range	Params.fpass	[0 200]	[0 200]
Padding	Params.pad	2	2
	Params.err	[ ]	[ ]
Trial Average	Params.trialave	0	0
Moving Window	W	[5 1]	1
Segment average	Params.SegAve	N/a	1

4.2.4. Functional connectivity measures

Undirected functional connectivity

Given the multivariate nature of the recorded data, partial correlation was used in place of correlation and partial coherence in place of coherence. Data was down sampled to 400Hz and notch filtered to remove line noise at 50Hz for calculation of undirected functional connectivity measures. Partial correlation was calculated using the 'partialcorr' command in MATLAB to calculate Pearson's correlation coefficient for each artefact-free epoch, with the mean taken across epochs for each animal, condition and time period.

Partial coherence was calculated using the 'ft_connectivityanalysis' command using FieldTrip (Oostenveld et al., 2011). A multi-taper fourier transform was calculated over artefact-free epochs for each region, animal, condition and time point using 'ft_freqanalysis' with the smoothing parameter 'cfg.tapsmofrq = 5'. The partial coherence was then calculated from the output of the fourier transformation adjusting for the effect of all other regions in the experimental preparation.

Directed functional connectivity

The Granger causality analysis presented in this chapter was performed with the Multivariate Granger causality (MVGC) toolbox version 1.0 (Barnett and Seth, 2014). The MVGC approach fits Vector Autoregression (VAR) models to the time series data with the VAR models in turn used to calculate the Granger causality. The fitting of the VAR models is key to obtaining accurate results with the MVGC. The selection of a model order that is too high can result in overfitting, while a model order that is too low results in underfitting. The model order was calculated for each animal, condition and time point using the command 'tsdata_to_infocrit' with the 'best' model order selected using the Akaike information criterion

(AIC). The VAR model was then calculated from the data based on the selected model order with the command 'tsdata_to_var'.

For each animal, condition and time period (baseline, early post-drug, late post-drug), epochs were entered as multiple trials for the calculation of the VAR model. The data used for the calculation of each VAR model was mean-centred and normalised by animal and time point and processed unfiltered in keeping with the guidance from the authors of the MVGC (Barnett and Seth, 2014, Barnett and Seth, 2011). Running the VAR model fitting procedure on two second epochs resulted in significant autocorrelation among the residuals from the VAR models with low model orders. To improve the fit of the VAR models these were calculated over ten second epochs which resulted in a higher model order and white residuals rather than autocorrelation. In the cortico-striatal experiment, animals two and four had high rates of artefacts in the data, meaning there were insufficient artefact-free epochs of ten seconds in the period of interest. For these animals, the length of the epoch used for the VAR calculation was reduced in 2 second intervals until a minimum of five continuously sampled artefact-free epochs length were available in the data which were then used to fit the VAR model. Of the 24 VAR models in the cortico-striatal experiment (one per animal, condition, and time point) three were fitted from eight second epochs, one from six second epochs and one from four second epochs. In the cortico-limbic experiment the VAR model orders ranged from 12 to 34, and the model order in the cortico-striatal models ranged from 9 to 21.

Once appropriate VAR models were obtained, the VAR models were converted to an autocovariance sequence using the command 'var_to_autocov'. The autocovariance sequence was used to calculate the spectral pairwise conditional Granger causality using the command 'autocov_to_spwcgc'. The spectral pairwise conditional Granger causality covers the full frequency range, however, can be integrated over a specific frequency range to provide band limited temporal Granger causality using the command 'smvgc_to_mvgc'. This was performed for each of the frequency bands of interest (Table 4.3) for comparison with undirected spectral FC measures and across the frequency range from 0-200Hz to provide a measure of temporal Granger causality.

4.2.5. Statistics

Comparison of measures between the 25I and control conditions

The significance of changes in spectral power, correlation, and coherence was tested by frequency band using the same approach for each variable. The change in each variable was calculated between baseline and the early post-drug period and between baseline and the

late post-drug period for each animal. For spectral power this was calculated for each region, and for correlation and coherence it was calculated for each pair of regions. Significance tests were then performed to test whether the change from baseline was significantly different between the 25I and control conditions.

Due to the small sample sizes and the risk of inflated type 1 error if parametric tests are performed on non-parametric data, the normality of the data was assessed prior to hypothesis testing. For each comparison, the normality of data for the 25I and control condition was assessed using the Shapiro-Wilks test using the 'shapiro.test' command in R. If there were no significant violations of normality ($p>0.05$ on Shapiro Wilks test) then a paired two-tailed T test was performed to test for difference between the 25I and control condition at each time point using the command 't.test' in R.

Where there were violations of normality ($p<0.05$ on Shapiro Wilks test) the intended approach was to use the Wilcoxon Signed Rank test – the non-parametric equivalent to the paired T test (Freidlin et al., 2003, Wilcoxon, 1945). Due to the small sample sizes in this study and the reduced statistical power of non-parametric tests it was not possible to demonstrate significance below the 5% level of significance using the Wilcoxon signed rank test and therefore this test was not performed. For a two-tailed test with $n=5$ the minimum p value attainable using this test is $p=0.0625$ and with $n=4$ the minimum p value attainable is $p=0.125$. Significance was therefore not tested where the data violated the assumption of normality and is marked in the figures accordingly.

For the Granger causality data, the authors of the MVGC toolkit are clear that GC is not known to follow a normal distribution and strongly advise against the use of parametric tests in interpreting changes in Granger causality (Barnett and Seth, 2014). The intended approach to statistically test for changes in GC between 25I and control was the Wilcoxon Signed Rank test (Wilcoxon, 1945), however, as discussed above the sample size of the present study was insufficient to obtain significant results using this approach, and so differences in Granger causality could not be tested for statistical significance.

False discovery rate correction

To account for multiple testing leading to excessive type 1 error false discovery rate (FDR), correction was performed using the approach of Benjamini, Hochberg and Yekutieli (Benjamini and Yekutieli, 2001, Benjamini and Hochberg, 1995). FDR was applied separately to the p values for spectral power, correlation and coherence at each time point using the 'p.adjust' command in R with the 'FDR' method. FDR was also used to correct the p values for the

correlation between undirected and directed FC. For each group of tests, the FDR correction procedure used reduces the probability that a significant result is a false positive to 5%.

Correlation between FC measures

Correlation analysis was used to determine whether there was evidence of correlation (or anticorrelation) between the changes in undirected and directed measures of FC. The difference in the change in undirected and directed FC between 25I and control was calculated for the early post-drug and late post-drug periods in the time and frequency domains. Due to the non-parametric distribution of Granger causality, rank correlation was calculated using Kendall's Tau. The correlation coefficients and p values were calculated with the 'corr' function in MATLAB with 'Kendall' as the 'Type' argument; p values were corrected using FDR (as described above) for each measure and time point.

Graphical presentation of functional connectivity measures

Due to the small sample sizes in this study and the non-parametric distribution of some variables, illustrating changes between functional connectivity measures using changes in means was not appropriate. The use of boxplots was considered, however, due to the large numbers of comparisons, did not visualise the data effectively. To graphically illustrate changes between drug and control, a rank correlation procedure was used to describe the distribution of the difference between the drug and control conditions, based on the Wilcoxon signed rank test. This approach has previously been used for presenting functional connectivity data from human MEG subjects (Barnett et al., 2020).

The Wilcoxon signed rank test is the non-parametric equivalent of the paired T test (Wilcoxon, 1945), with the data paired in these experiments between the 25I and control conditions. The Wilcoxon signed rank test measures whether paired differences are symmetrical around the mean. The W statistic is calculated by ranking the absolute magnitude of the differences between paired values across the two groups and calculating the sum of the ranks with a positive signed difference and subtracting the sum of ranks with a negative signed difference. The MATLAB command 'signedrank' was used to calculate the W statistic which was normalised based on the minimum and maximum possible values to give a score between -1 and 1.

A normalised W statistic of 1 means that all paired measures were higher in the 25I condition over control, whilst a value of -1 means that all paired measures were lower in the 25I condition

compared to control. A value of zero indicates that the paired differences were symmetrical around the mean – indicating there is no difference between groups.

4.3. Results

4.3.1. Local field potentials

Representative LFP traces from each region in a single animal are presented for the cortico-limbic experiment in Figure 4.5 and the cortico-striatal experiment in Figure 4.6. LFP from a single 2 second epoch is shown for the baseline, early post-drug and late post-drug periods in the 25I and control conditions.

Figure 4.5: Representative LFP traces from a single animal in the cortico-limbic experiment

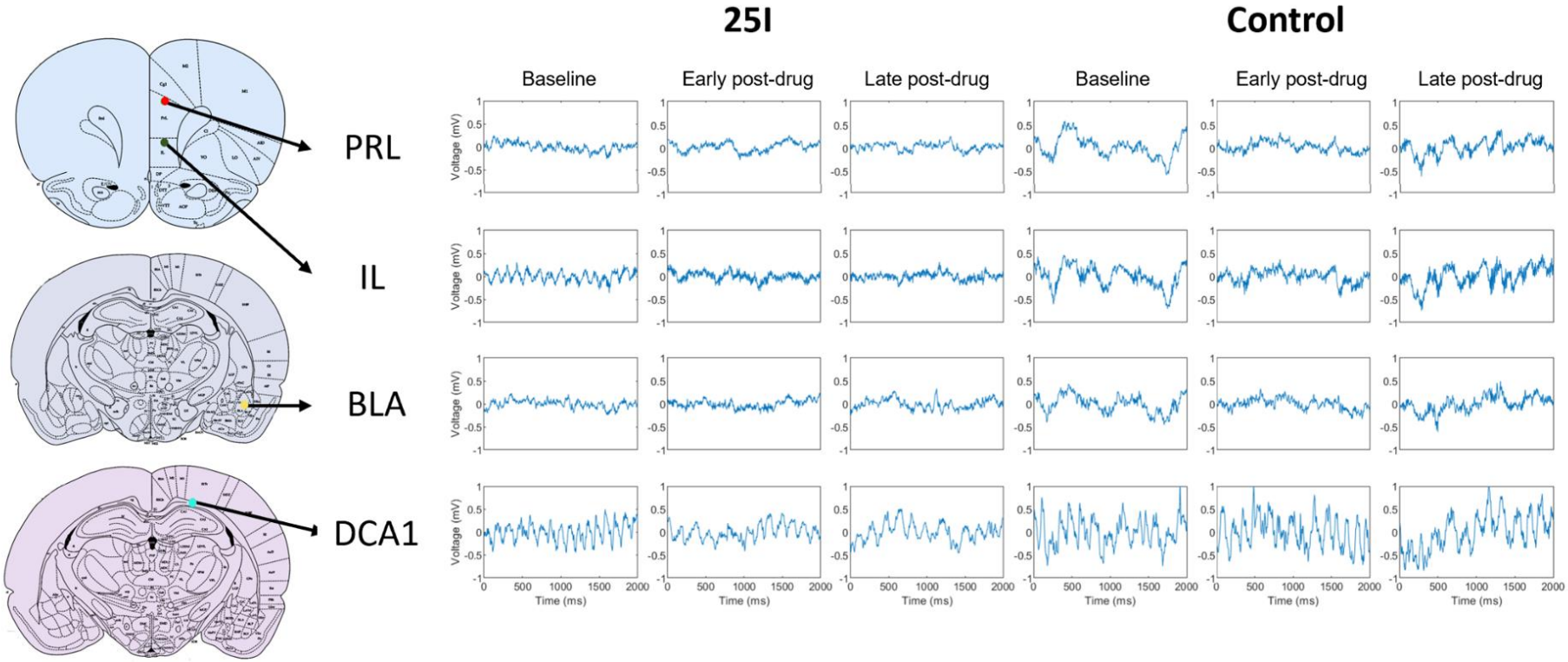

Representative LFP traces from each region, time point and condition are shown from animal 4 in the cortico-limbic experiment. The LFP traces in each column are from a single 2 second epoch. LFP data was demeaned but otherwise is presented unfiltered or unmodified.

Figure 4.6: Representative LFP traces from a single animal in the cortico-striatal experiment

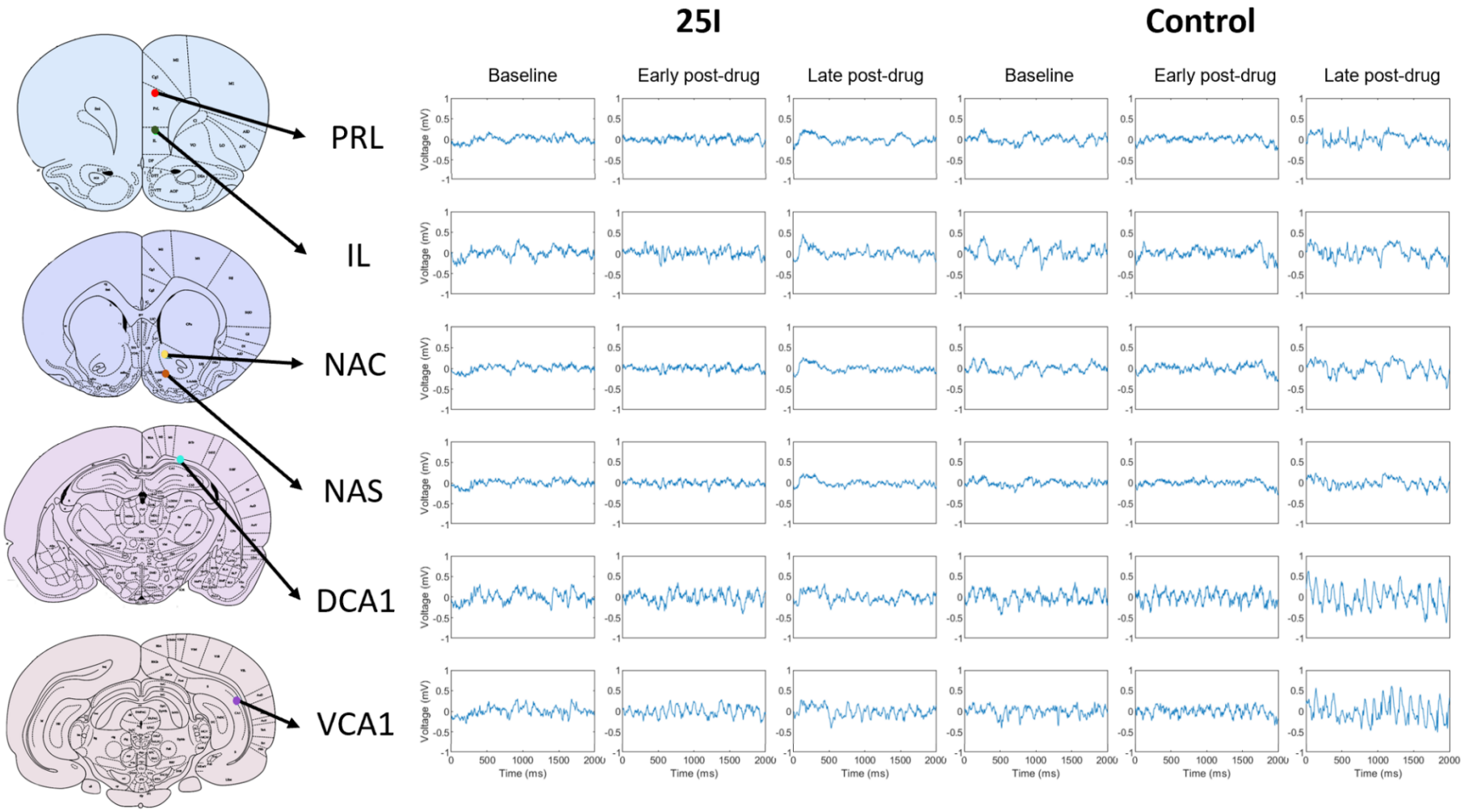

Representative LFP traces from each region, time point and condition are shown from animal 4 in the cortico-striatal experiment. The LFP traces in each column are from a single 2 second epoch. LFP data was demeaned but otherwise is presented unfiltered or unmodified.

4.3.2. Spectral analysis

5-HT_{2A} agonism causes immediate onset of persistent HFO across cortico-limbic and cortico-striatal networks

Spectrograms enable changes in spectral power to be visualised by frequency and time and can be used to provide a summary of the LFP data over the course of the experiment. Spectrograms are presented for the 25I and control condition for the cortico-limbic experiment in Figure 4.7, and the cortico-striatal experiment in Figure 4.8. Shortly after administration of 25I the emergence of a distinct, largely continuous, band of HFO is seen in the BLA, NAC, NAS, IL and PRL. The emergence of this distinct HFO band is accompanied by general reduction in spectral power leading to a blackening of the background on the spectrograms seen as increases in the amount of dark blue in the plots and is most visible from the beta bands upwards.

Figure 4.7: Representative spectrograms from a single animal in the cortico-limbic study

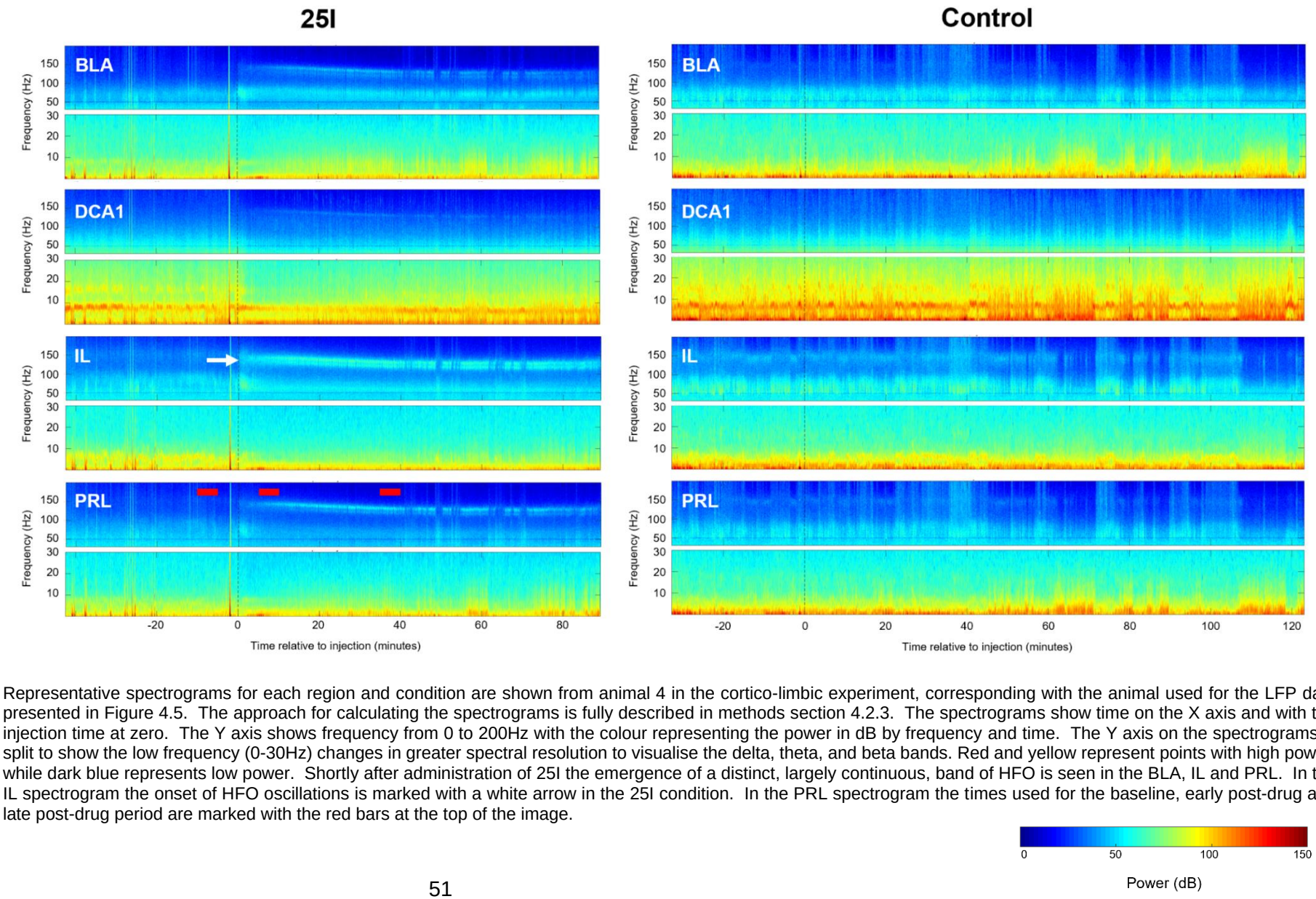

Representative spectrograms for each region and condition are shown from animal 4 in the cortico-limbic experiment, corresponding with the animal used for the LFP data presented in Figure 4.5. The approach for calculating the spectrograms is fully described in methods section 4.2.3. The spectrograms show time on the X axis and with the injection time at zero. The Y axis shows frequency from 0 to 200Hz with the colour representing the power in dB by frequency and time. The Y axis on the spectrograms is split to show the low frequency (0-30Hz) changes in greater spectral resolution to visualise the delta, theta, and beta bands. Red and yellow represent points with high power, while dark blue represents low power. Shortly after administration of 25I the emergence of a distinct, largely continuous, band of HFO is seen in the BLA, IL and PRL. In the IL spectrogram the onset of HFO oscillations is marked with a white arrow in the 25I condition. In the PRL spectrogram the times used for the baseline, early post-drug and late post-drug period are marked with the red bars at the top of the image.

Figure 4.8: Representative spectrograms from a single animal in the cortico-striatal experiment

Representative spectrograms for each region and condition are shown from animal 4 in the cortico-striatal experiment, corresponding with the animal used for the LFP data presented in Figure 4.5. The approach for calculating the spectrograms is fully described in methods section 4.2.3. The spectrograms show time on the X axis and with the injection time at zero. The Y axis shows frequency from 0 to 200Hz with the colour representing the power in dB by frequency and time. The Y axis on the spectrograms is split to show the low frequency (0-30Hz) changes in greater spectral resolution to visualise the delta, theta, and beta bands. Red and yellow represent points with high power, while dark blue represents low power. Shortly after administration of 25I the emergence of a distinct, largely continuous, band of HFO is seen in the NAC, NAS, IL and PRL.

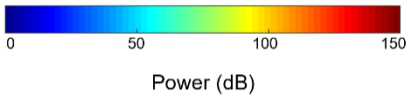

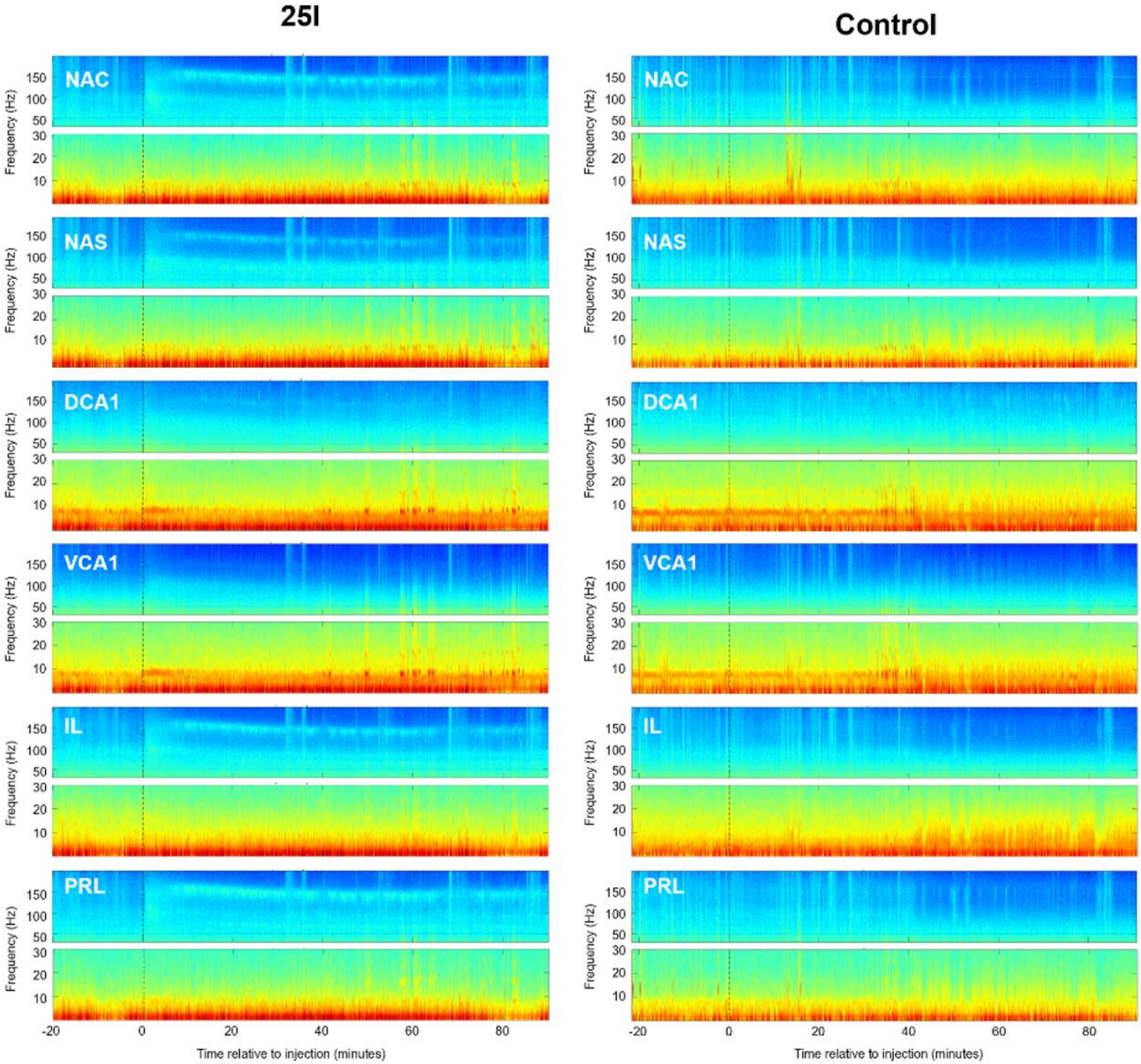

5-HT_{2A} agonist induced HFO shows a reduction in peak frequency over time

To visualise and compare spectral power across animals, power spectra were calculated for each animal, region, and time point. These are presented in Figure 4.9 for the cortico-limbic experiments and Figure 4.10 for the cortico-striatal experiments. To enable visual comparison between animals and recording sessions Z scores were calculated across the power spectra from the periods of interest for each animal and condition.

In the cortico-limbic experiments (Figure 4.9) the emergence of HFO oscillations can be clearly seen in BLA, IL and PRL following 25I in the early and late post-drug periods relative to control. There is a reduction in the peak frequency of HFO between the early and late post-drug periods. Where there are HFO peaks visible in the power spectra in the control condition these remain stable across the three time points. A reduction in both low and high gamma frequencies can be seen in the IL and PRL regions in the early post-drug period. In the cortico-striatal experiments (Figure 4.10) there is clear emergence of HFO in NAC, NAS, IL and PRL in the early post-drug period, with a reduction in peak frequency of HFO between the early and late post-drug periods. The absence of HFO in the hippocampal regions in both experiments likely reflects low levels of $5HT_{2A}$ receptor expression in the hippocampus (Weber and Andrade, 2010).

Figure 4.9: Power spectra by time point and region for cortico-limbic experiment

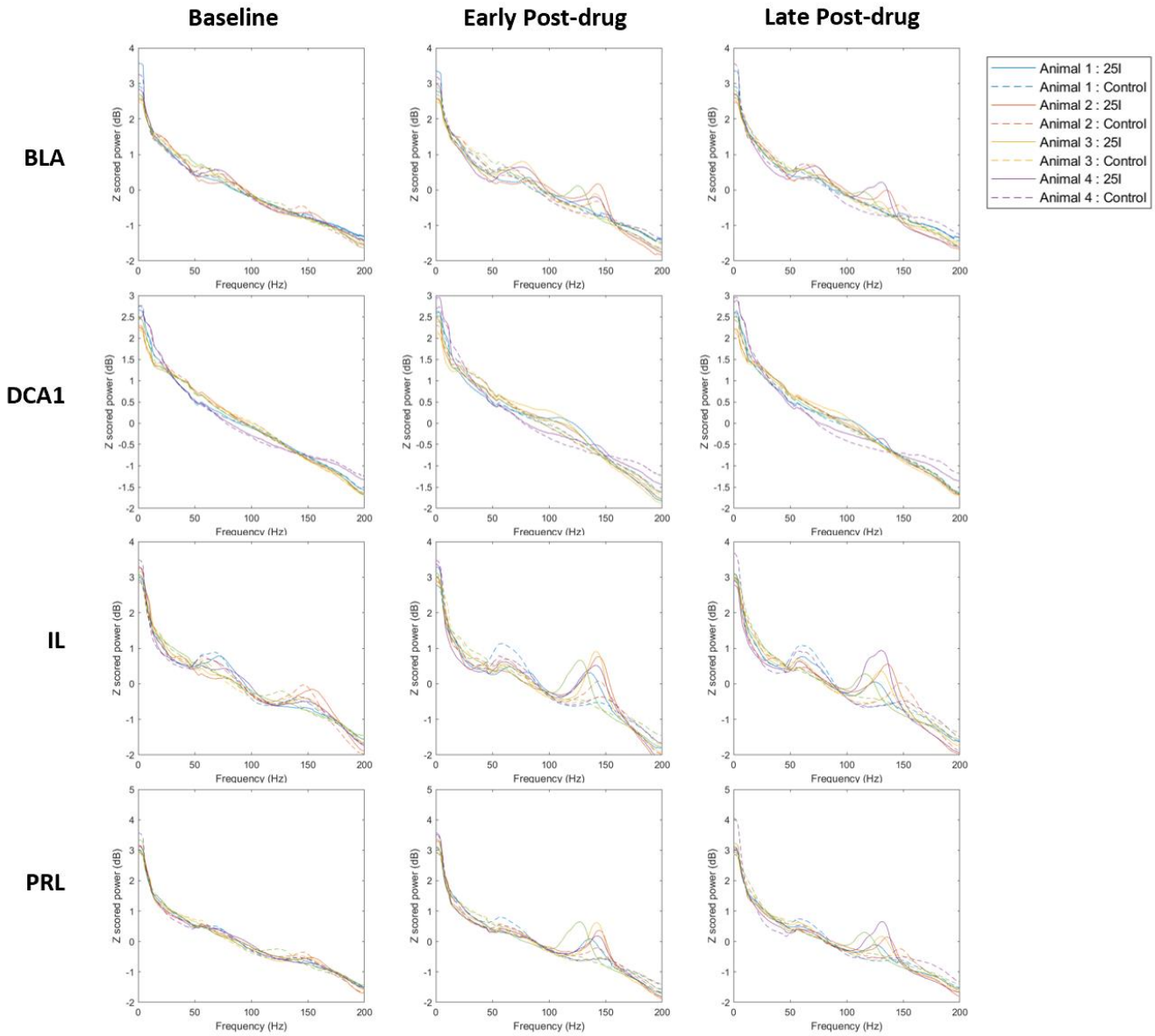

Z scored power spectra for each animal and condition are plotted by region and time point. Data from each animal is shown in a single colour with spectra from the 25I condition shown with solid lines and spectra from the control condition showing with dashed lines.

Figure 4.10: Power spectra by time point and region for cortico-striatal experiment

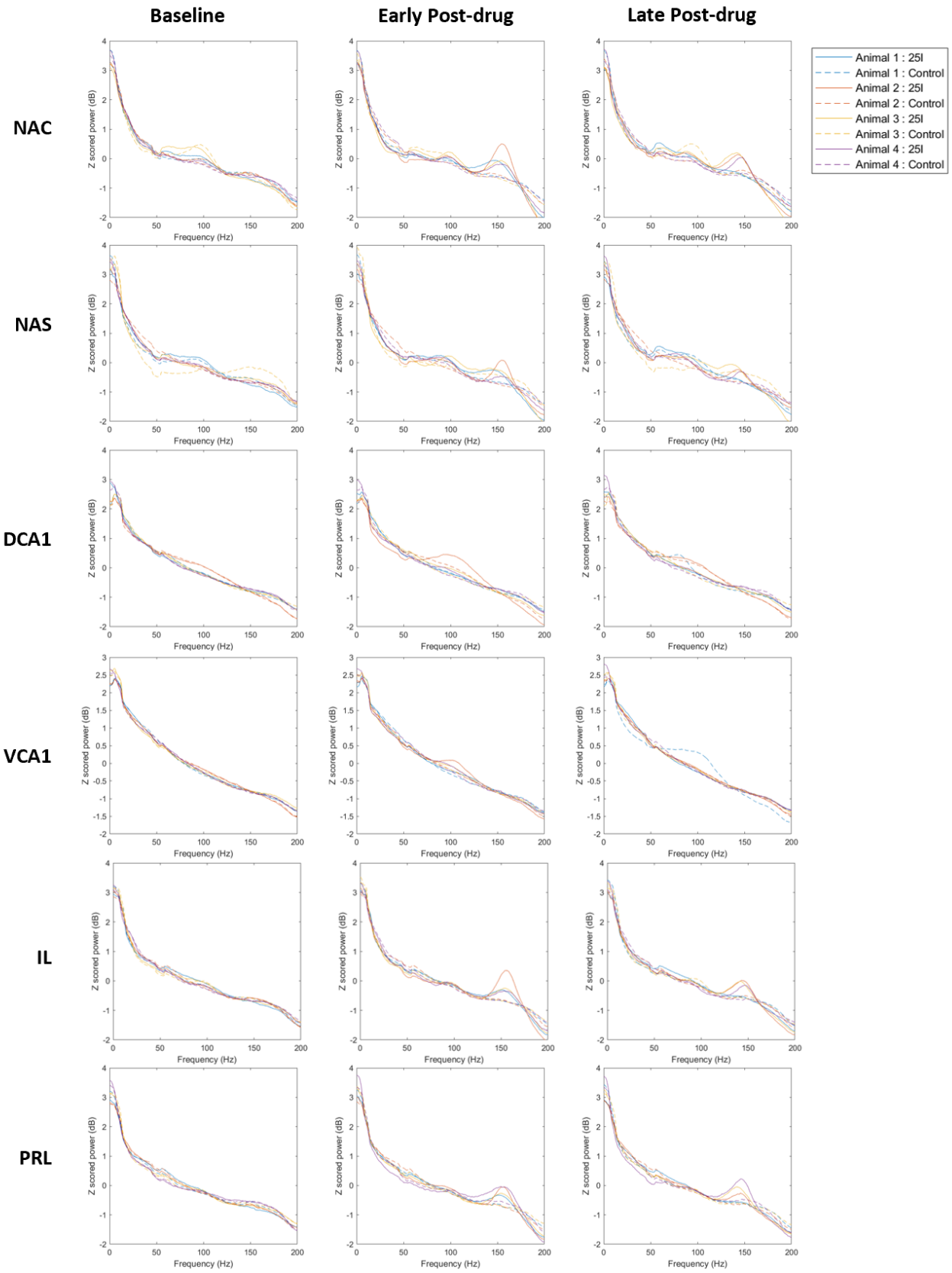

Z scored power spectra for each animal, and condition are plotted by region and time point. Data from each animal is shown in a single colour with spectra from the 25I condition shown with solid lines and spectra from the control condition showing with dashed lines.

4.3.3. Increases in HFO power in cortico-limbic and cortico-striatal circuits is persistent; at other frequencies power shows a biphasic response

To enable statistical comparison of the power data presented in Figure 4.9 and Figure 4.10, band-limited power was calculated for each time point and condition as the mean power across each of the frequency bands in Table 4.1. The percentage change in band-limited power from baseline (ΔPower) in each frequency band was calculated for the early post-drug and late post-drug periods in the 25I ($\Delta Power_{25I}$) and control conditions ($\Delta Power_{Control}$).

Figure 4.11 graphically illustrates the mean percentage difference between the 25I and control conditions ($\Delta Power_{25I} - \Delta Power_{Control}$) for each frequency band and region for the early post-drug and late post-drug periods. Where data were normally distributed the results of significance testing between the $\Delta Power_{25I}$ and $\Delta Power_{Control}$ are shown. Results of significance testing are presented pre- and post-FDR correction.

In the cortico-limbic experiment the general pattern of drug effects appeared to be biphasic, with a global decrease in power in the early post-drug period, followed by subsequent increases in the late post-drug period. In the early post-drug period in the cortico-limbic experiments there was a significant increase in HFO power for 25I over control in the IL and PRL regions, with significant decreases in low gamma power in BLA, and across low gamma and beta power in IL. These findings were no longer significant following FDR correction.

In the cortico-striatal experiments the same general trends were apparent. In the early post-drug period, there was a general reduction in power for 25I over control, except for HFO which showed increases in the NAC, NAS, IL and PRL. In the late post-drug period the increase in power in the HFO band persisted but was no longer significant and there were broadband non-significant increases in hippocampal power.

Figure 4.11: Percentage change in band-limited spectral power by region

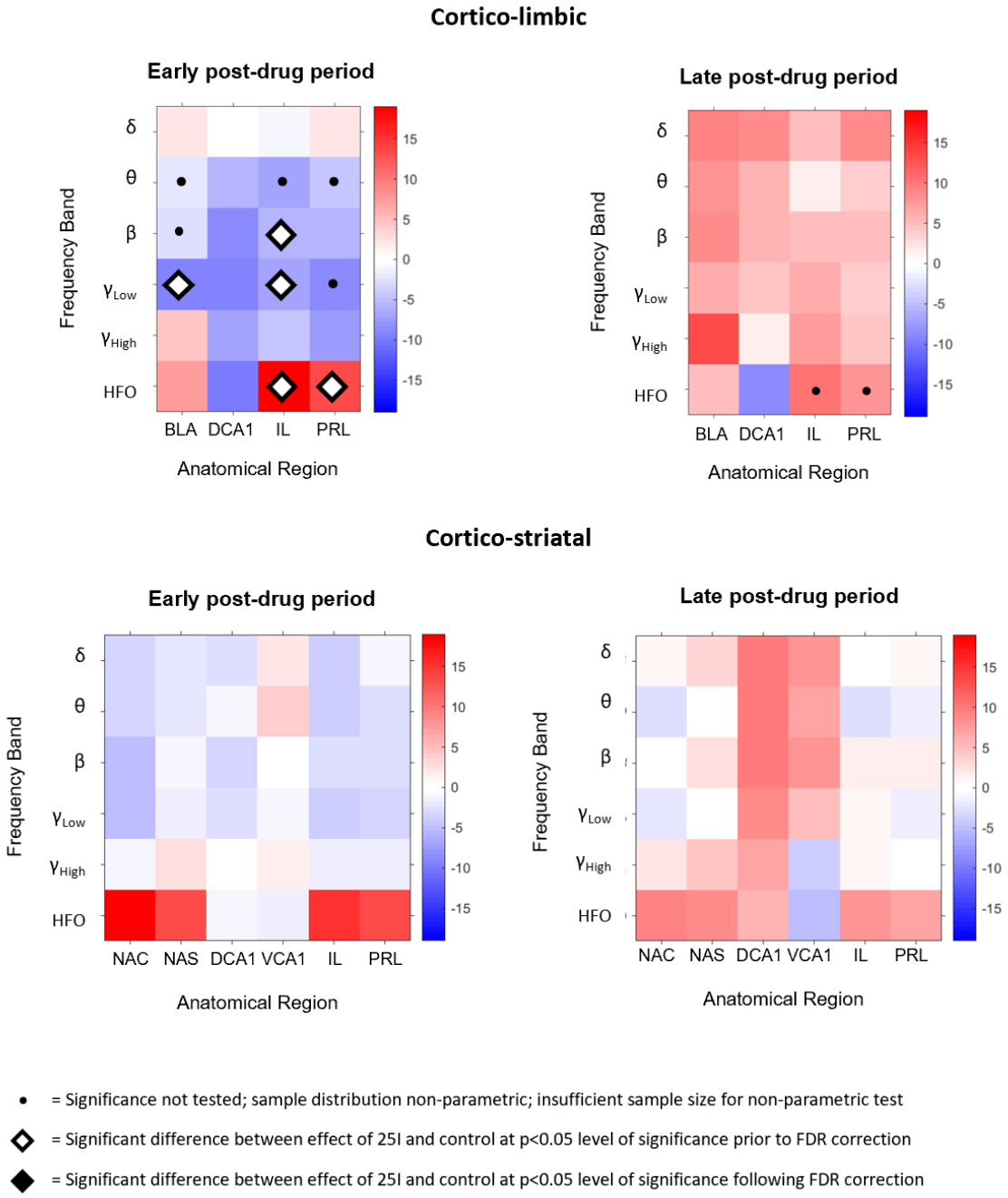

The colour of each grid square represents the mean difference between the percentage change in band-limited spectral power from baseline (ΔPower) between the 25I and control condition ($\Delta Power_{25I} - \Delta Power_{Control}$) for the early and late post-drug periods. Open diamonds indicate a significant difference between Δ25I and ΔControl on a two tailed paired T-test ($p<0.05$) prior to FDR adjustment. Closed black diamonds indicate significance tests that remained significant at ($p<0.05$) following FDR adjustment. Where no symbol is shown, a T-test was performed but did not reach the threshold for significance ($p<0.05$). Black dots indicate comparisons where data was non-parametric and significance testing was not performed.

4.3.4. Time-domain functional connectivity:

25I shows distinct patterns of modulation across cortico-hippocampal, cortico-limbic, and cortico-striatal circuits

Changes in time-domain functional connectivity were calculated from baseline for partial correlation (undirected functional connectivity; ΔCorr) and time-domain Granger causality directed functional connectivity; ΔGC). The difference between ΔCorr and ΔGC in the 25I condition relative to control is shown for the early and late post-drug periods in Figure 4.12 and 4.13 respectively.

Figure 4.12: Changes in temporal domain functional connectivity from baseline to the early post-drug period

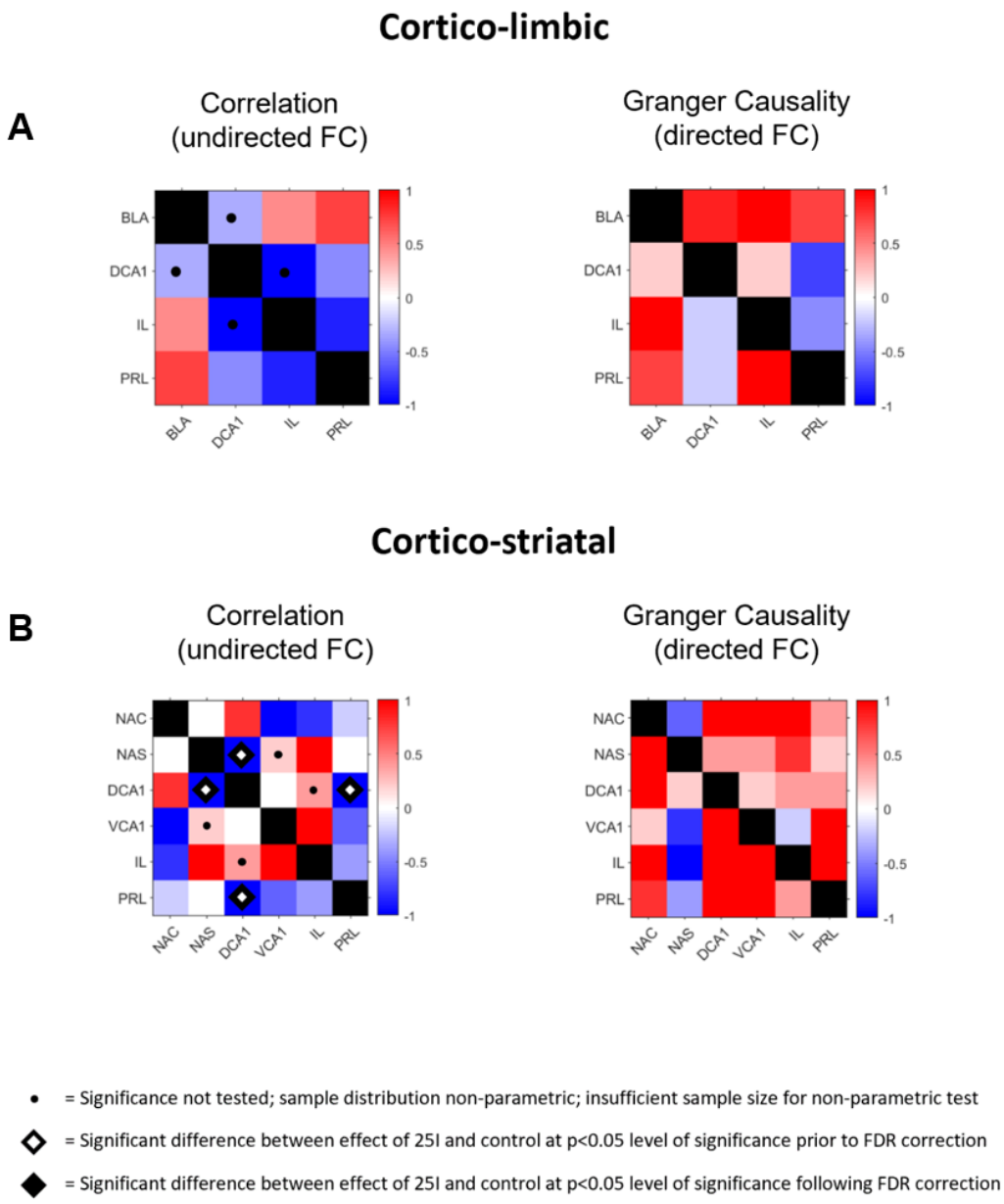

Functional connectivity data from cortico-limbic experiments (A) and cortico-striatal experiments (B). The colour of each grid square represents the difference between the change in functional connectivity (FC) from baseline (ΔFC) between the 25I (ΔFC_{25I}) and control condition ($\Delta FC_{Control}$). The data is presented using the W statistic from the Wilcoxon signed rank test normalised to a value between -1 and 1 (see Methods 4.2.5) and is presented on a colour scale from red to blue, with blue representing a decrease in FC in the 25I condition relative to control, and red representing an increase in FC in the 25I condition relative to control. Undirected FC is symmetrical between region pairs, however, directed FC varies depending on whether it is inbound or outbound. The direction of the connection for the directed FC is always read as from the region on the X axis, to the region on the Y axis. Open diamonds indicate a significant difference between ΔFC_{25I} and $\Delta FC_{Control}$ on a two tailed paired T-test ($p<0.05$) prior to FDR adjustment. Closed black diamonds indicate significance tests that remained significant at ($p<0.05$) following FDR adjustment. Where no symbol is shown, a T-test was performed but did not reach the threshold for significance ($p<0.05$). Black dots indicate comparisons where data was non-parametric and significance testing was not performed. Significant testing was not performed for directed FC (see Methods 4.2.5).

In the early post-drug period in the cortico-limbic experiments (Figure 4.12A) there were decreases in ΔCorr for the 25I condition relative to control between all regions except for the connections between the prefrontal cortex and the amygdala, although none of these changes reached significance. There were increases in ΔGC for 25I relative to control to the BLA from all other regions, with corresponding increases in ΔGC from BLA to both IL and PRL. The connection from IL to PRL showed an increase in ΔGC, whilst the reciprocal connection showed a decrease suggestive of relative drive from IL to PRL.

In the early post-drug period in the cortico-striatal experiment (Figure 4.12B) there were significant decreases in ΔCorr for the 25I condition relative to control in between DCA1 and NAS and DCA1 and PRL suggesting disturbance of both the cortico-hippocampal and striato-hippocampal pathways. These changes were no longer significant following FDR. There were increases in Granger causality for the 25I condition relative to control between all pairs of regions in both directions with the exception of the NAS which showed a reduction in outbound Granger causality to all other regions, and a decrease in Granger causality from VCA1 to IL.

In the late post-drug period in the cortico-limbic experiment (Figure 4.13A), there was a significant increase in ΔCorr for the 25I condition relative to control between DCA1 and BLA, although this was no longer significant following FDR correction. There were global increases in Granger causality, except for the connections from DCA1 and IL to PRL which were decreased.

In the late post-drug period in the cortico-striatal experiment there were no significant changes in correlation between regions (Figure 4.13B). The NAC continued to show strong increases in ΔGC for the 25I condition relative to control, with strong directionality to NAS, VCA1, IL and PRL, with reduction in the strength of the reciprocal connections suggesting the NAC is taking a stronger driving role of the NAC in the cortico-striatal circuit, in keeping with bottom-up changes in cognition, whilst IL and PRL showed bidirectional increases in Granger causality.

As discussed in section 4.2.5 it was not possible to test for significant changes in Granger causality due to the non-parametric distribution of Granger causality and the small sample size of the study.

Figure 4.13: Changes in temporal domain functional connectivity from baseline to the late post-drug period

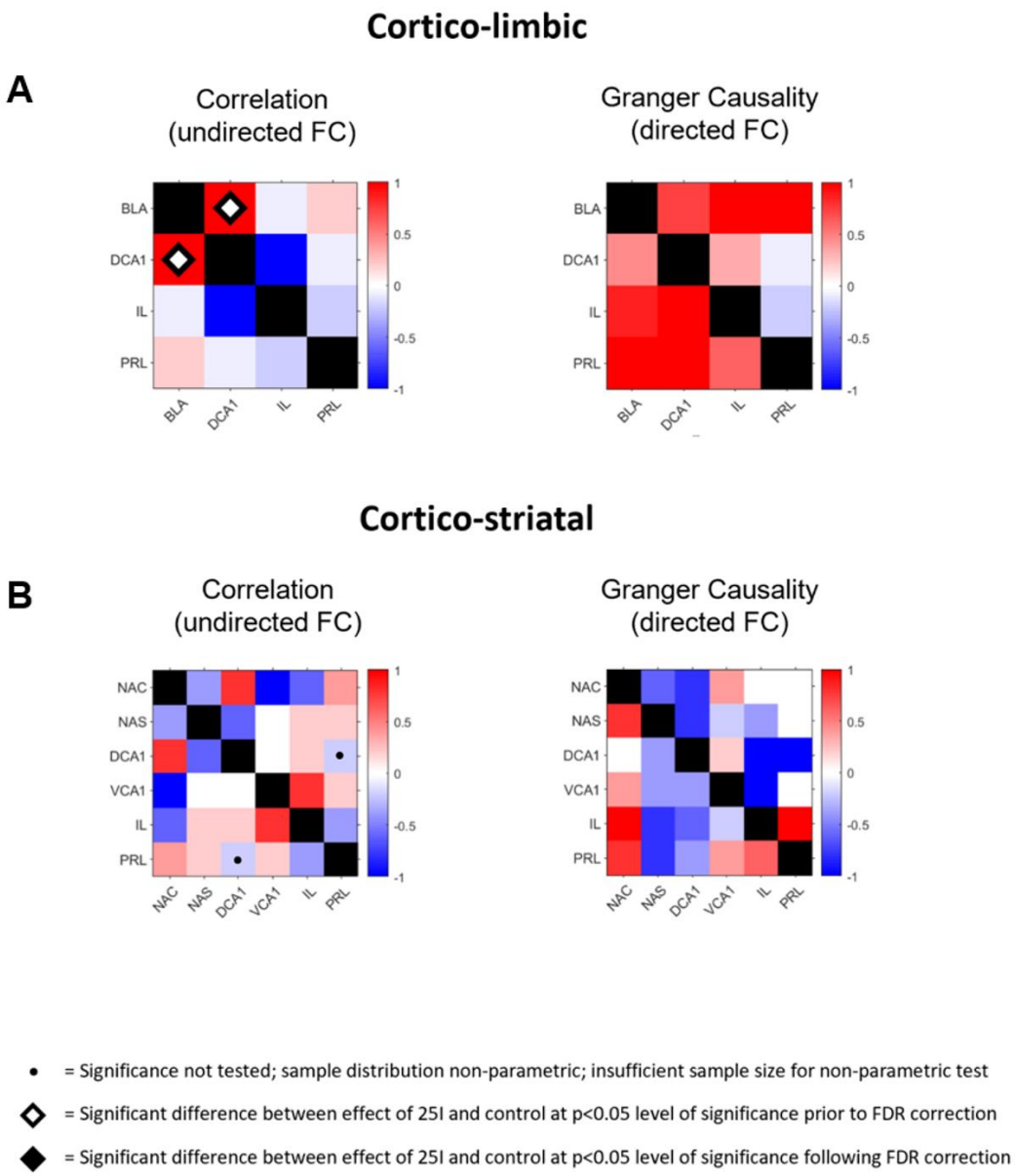

Functional connectivity data from cortico-limbic experiments (A) and cortico-striatal experiments (B). The colour of each grid square represents the difference between the change in functional connectivity (FC) from baseline (ΔFC) between the 25I (ΔFC_{25I}) and control condition ($\Delta FC_{Control}$). The data is presented using the W statistic from the Wilcoxon signed rank test normalised to a value between -1 and 1 (see Methods 4.2.5) and is presented on a colour scale from red to blue, with blue representing a decrease in FC in the 25I condition relative to control, and red representing an increase in FC in the 25I condition relative to control. Undirected FC is symmetrical between region pairs, however, directed FC varies depending on whether it is inbound or outbound. The direction of the connection for the directed FC is always read as from the region on the X axis, to the region on the Y axis. Open diamonds indicate a significant difference between ΔFC_{25I} and $\Delta FC_{Control}$ on a two tailed paired T-test ($p<0.05$) prior to FDR adjustment. Closed black diamonds indicate significance tests that remained significant at ($p<0.05$) following FDR adjustment. Where no symbol is shown, a T-test was performed but did not reach the threshold for significance ($p<0.05$). Black dots indicate comparisons where data was non-parametric and significance testing was not performed. Significant testing was not performed for directed FC (see Methods 4.2.5).

Correlation between time-domain undirected and directed functional connectivity was highly variable but not significant

To test the hypothesis that changes in undirected functional connectivity (ΔCorr) and directed functional connectivity (ΔGC) induced by 25I would move in the same direction, rank correlation was calculated using Kendall's Tau. Correlation coefficients were calculated between the effects of 25I on undirected ($\Delta Corr_{25I}$- $\Delta Corr_{Control}$) and directed (ΔGC_{25I}- $\Delta GC_{Control}$) functional connectivity for each region pair and direction with the results illustrated graphically in Figure 4.14. The relationship between undirected and directed functional connectivity was variable, with some regions showing correlation and others anticorrelation, and none of the correlations reaching significance.

Figure 4.14: Correlation between the change in undirected and directed temporal domain functional connectivity

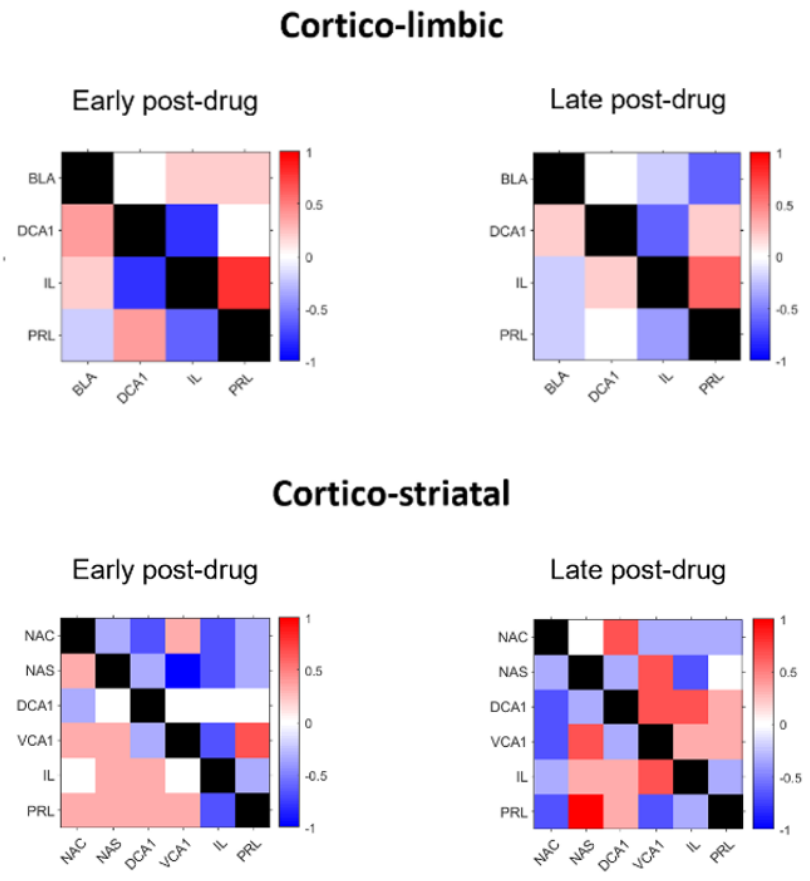

The colour of each grid square represents the rank correlation coefficient between the effect of 25I on undirected functional connectivity ($\Delta Corr_{25I}$- $\Delta Corr_{Control}$) and directed FC (ΔGC_{25I}- $\Delta GC_{Control}$) in each direction calculated using Kendall's Tau. The direction of the connection for the directed FC is always read as from the region on the X axis, to the region on the Y axis. None of the correlations in this figure were significant prior to FDR correction.

4.3.5. Frequency domain functional connectivity

Both coherence and frequency domain Granger causality vary with frequency. In this section the continuous measures of coherence and frequency domain Granger causality are presented graphically, prior to statistical comparison of band-limited functional connectivity in the frequency bands of interest.

4.3.6. Baseline coherence provides anatomical insights

The relationship between coherence and frequency for each pair of regions in the cortico-limbic experiments is shown in Figure 4.15 and for the cortico-striatal experiments in Figure 4.16. Coherence remains largely stable between the baseline, early post-drug and late post-drug periods in both experiments. In both experiments and conditions there is high coherence between PRL and IL across the frequency bands with peaks in theta visible in all recordings, and HFO and gamma peaks more prominent in the cortico-limbic experiment. Hippocampal-prefrontal theta coherence can also be seen in both conditions and experiments.

Figure 4.15: Cortico-limbic coherence by region pair and frequency

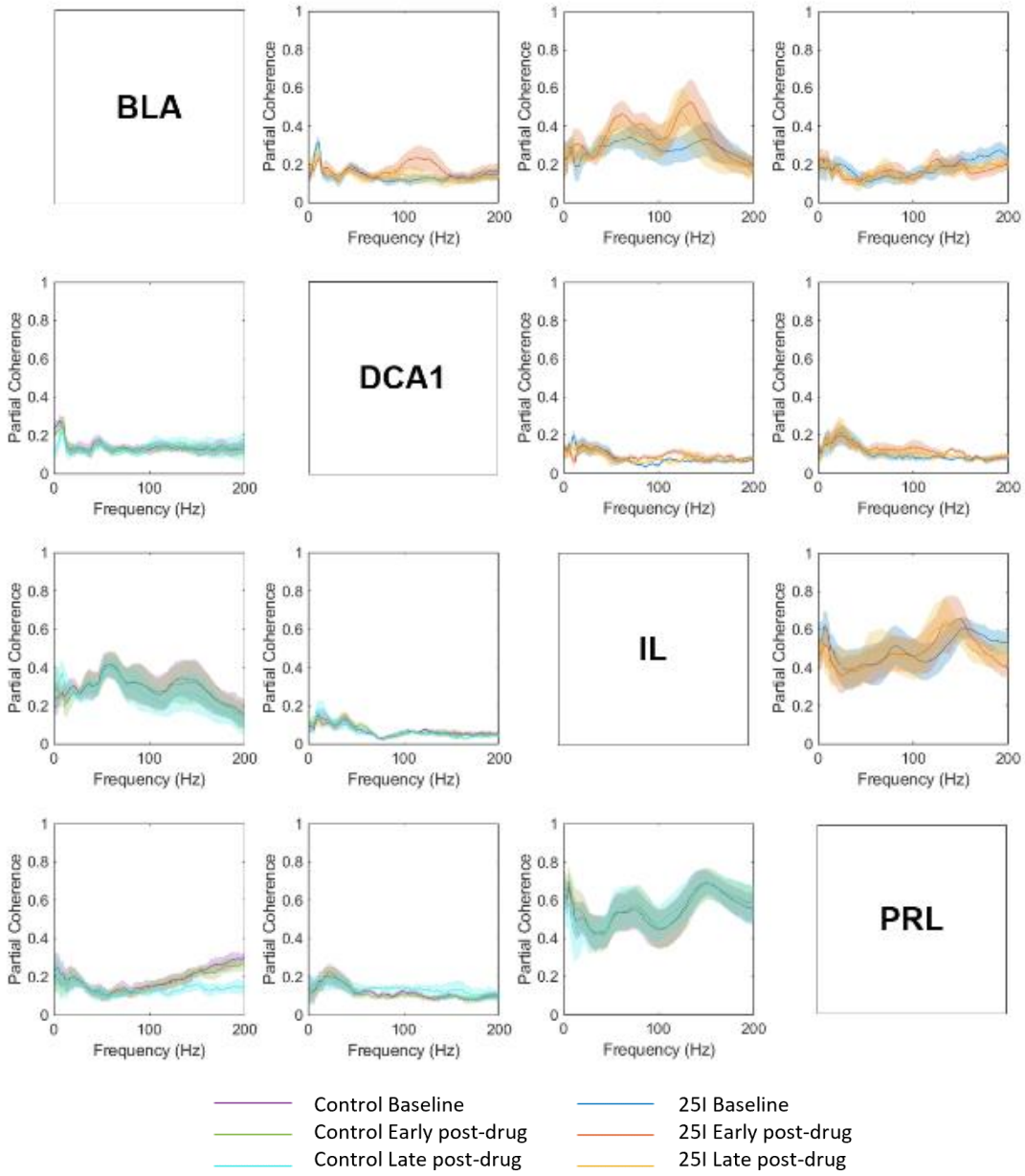

Panel plot of the mean +/- standard error of coherence across animals (n=5) for each condition and pair of regions. The regions are listed along the diagonal with the plot for each pair of regions at the intersection of row and column. Each plot shows the coherence for the baseline, early post-drug and late post-drug period coloured according to the key at the bottom of the panel. Plots to the bottom left show coherence in the control condition, whilst plots to the top right show coherence in the 25I condition.

In the cortico-striatal experiment (Figure 4.16) there is a high level of coherence between recordings from NAC and NAS across the 25I and control conditions. There is also a strong coherence between IL and NAC, which is stronger than the coherence with PRL across the full spectrum. The NAC demonstrates higher coherence than NAS with both PRL and IL suggesting stronger functional pathways between the two regions. Strong coherence is seen in the theta range between DCA1 and VCA1 in keeping with the hippocampus as the primary source of theta. High levels of broadband coherence in IL and PRL support synchronisation of computation across prefrontal cortical regions.

Figure 4.16: Cortico-striatal coherence by region pair and frequency

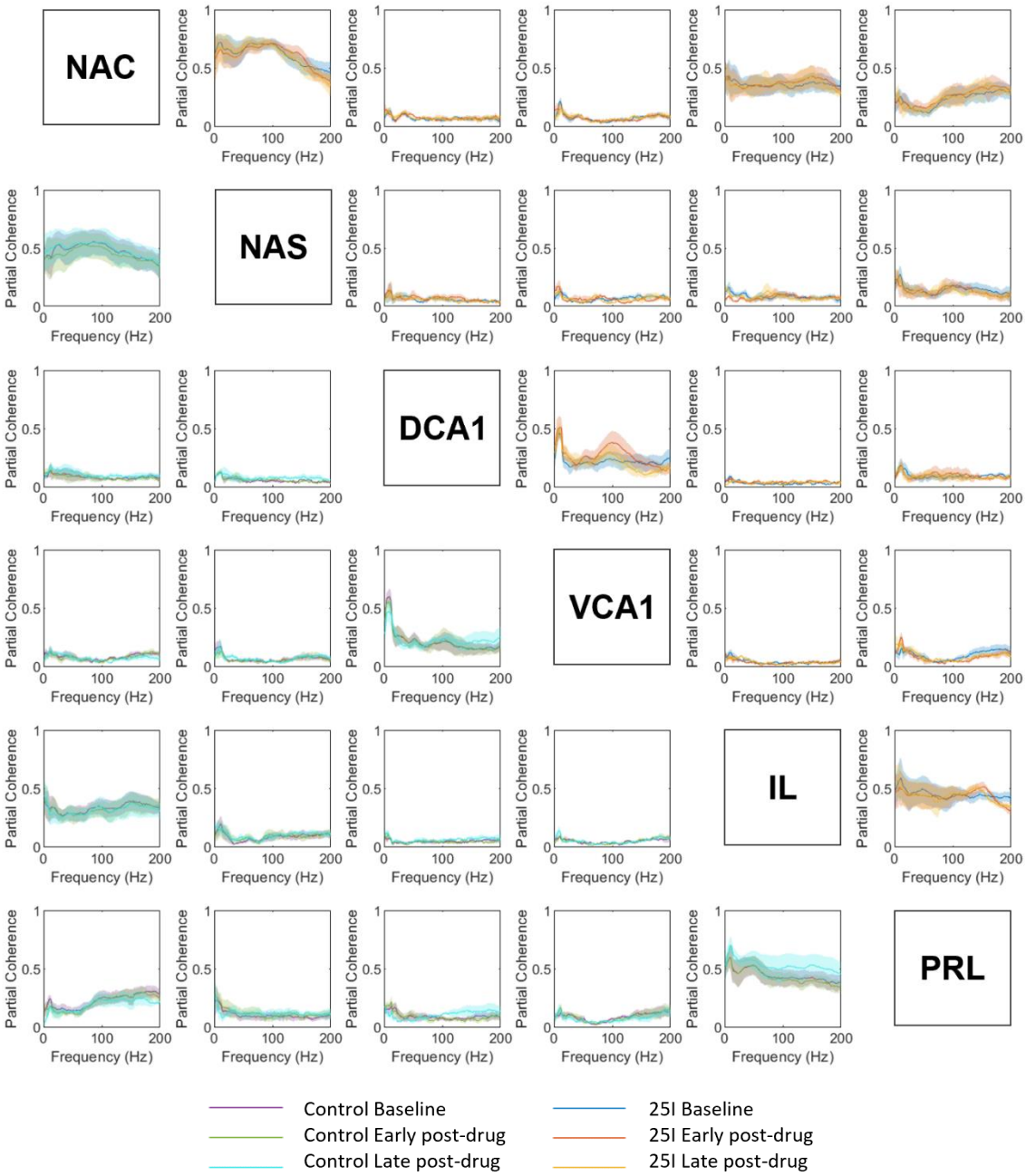

Panel plot of the mean +/- standard error of coherence across animals (n=4) for each condition and pair of regions. The regions are listed along the diagonal with the plot for each pair of regions at the intersection of row and column. Each plot shows the coherence for the baseline, early post-drug and late post-drug period coloured according to the key at the bottom of the panel. Plots to the bottom left show coherence in the control condition, whilst plots to the top right show coherence in the 25I condition.

4.3.7. 25I causes specific changes in coherence occur across the cortico-hippocampal, cortico-limbic, and cortico-striatal circuits

In the control condition in the cortico-limbic experiments (Figure 4.15) there is a decrease in coherence in the higher frequencies in the late post-drug period between the PRL and BLA, and a slight increase in gamma coherence between DCA1 and PRL. A similar picture is seen in the late post-drug period with small increases in high frequency coherence between IL and PRL, DCA1 and PRL and DCA1 and VCA1. Overall, the changes in the control condition are minor across both experiments.

In contrast in the 25I condition there are clear increases in cortico-limbic coherence in the gamma and HFO range between IL and BLA. There is evidence of the emergence of HFO coherence between IL and PRL and to a lesser extent between BLA and DCA1. There is a decrease in theta coherence between DCA1 and BLA, and between DCA1 and IL suggesting probable disruption of cortico-hippocampal connectivity.

In the cortico-striatal experiments (Figure 4.16) under the 25I condition there is evidence of an increase in coherence between DCA1 and VCA1 at approximately 100Hz that is more pronounced in the early post-drug period. There is a slight increase in HFO coherence between IL and PRL, with a reduction in coherence above 150Hz. There is an increase in theta coherence between VCA1 and PRL and a decrease in theta and delta coherence between NAS and IL.

4.3.8. Baseline Granger causality suggests a physiological role for HFO in the cortico-limbic circuit and affirms known roles of theta and gamma oscillations in cortico-hippocampal circuitry

The relationship between frequency and Granger causality for the cortico-limbic experiments is shown for the control condition in Figure 4.17 and for the 25I condition in Figure 4.18. The relationship between frequency and Granger causality for the cortico-striatal experiments is shown for the control condition in Figure 4.19 and for the 25I condition in Figure 4.20.

Figure 4.17: Cortico-limbic spectral Granger causality by region pair and frequency in the control condition

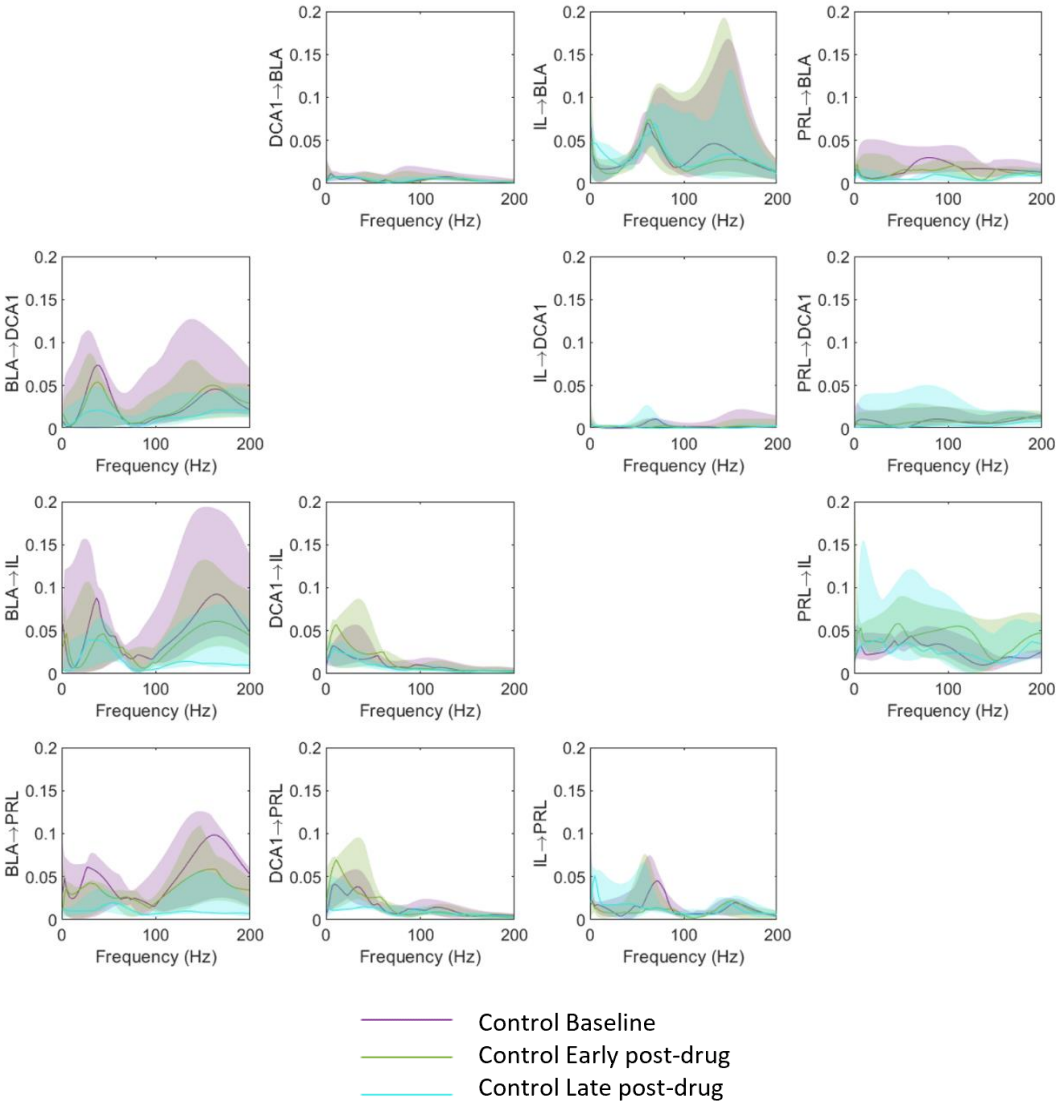

The median +/- interquartile range of Granger causality in the control condition is plotted across animals (n=5) for each pair of regions. For each connection Granger causality is calculated for each direction, with the plot for the same connection in the opposite direction located in the symmetrical location across the diagonal in the panel. Each plot shows the Granger causality for the baseline, early post-drug and late post-drug period coloured according to the key at the bottom of the panel.

Figure 4.18: Cortico-limbic spectral Granger causality by region pair and frequency in the 25I condition

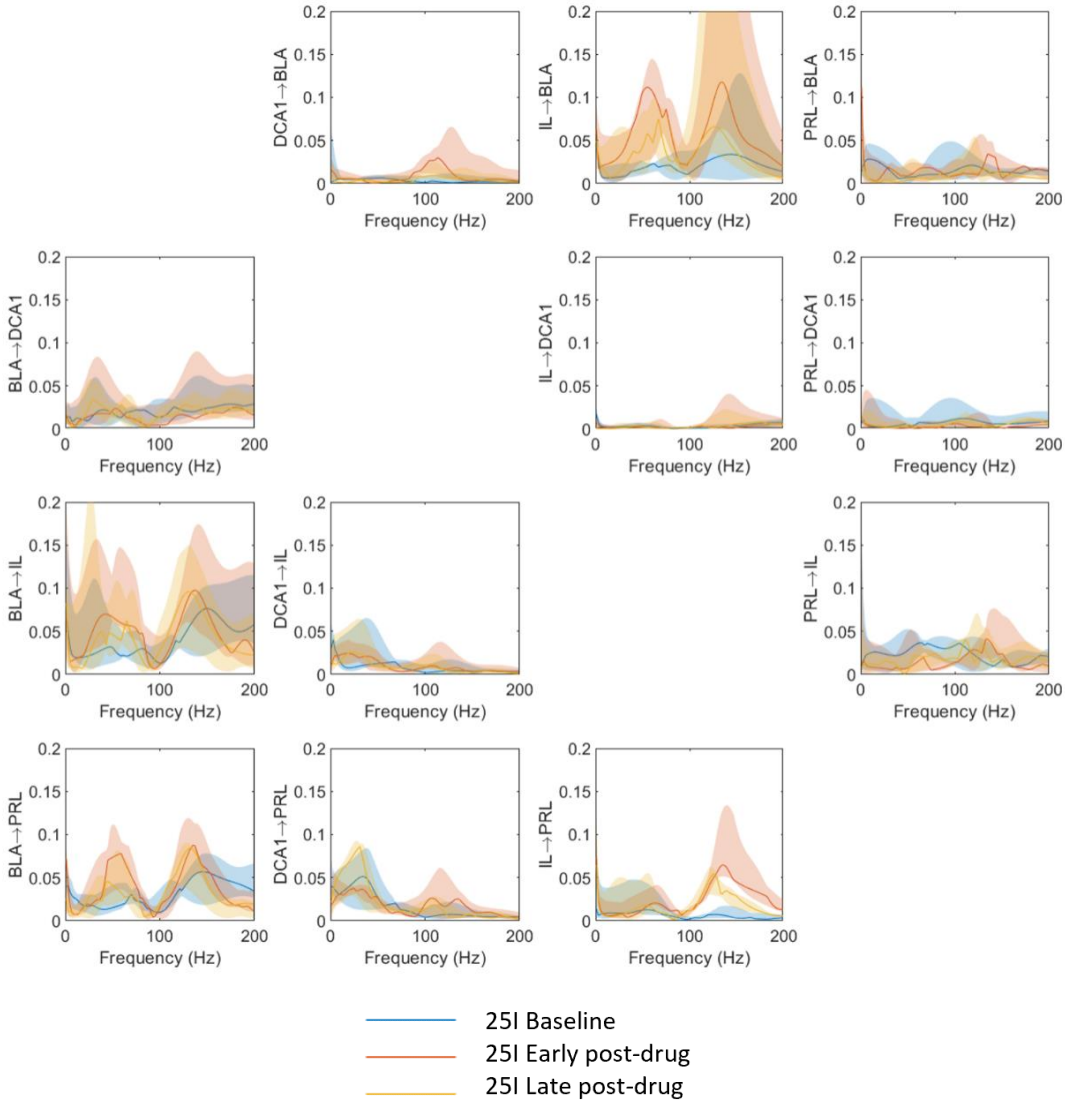

The median +/- interquartile range of Granger causality in the 25I condition is plotted across animals (n=5) for each pair of regions. For each connection Granger causality is calculated for each direction, with the plot for the same connection in the opposite direction located in the symmetrical location across the diagonal in the panel. Each plot shows the Granger causality for the baseline, early post-drug and late post-drug period coloured according to the key at the bottom of the panel.

Figure 4.19: Cortico-striatal spectral Granger causality by region pair and frequency in the control condition

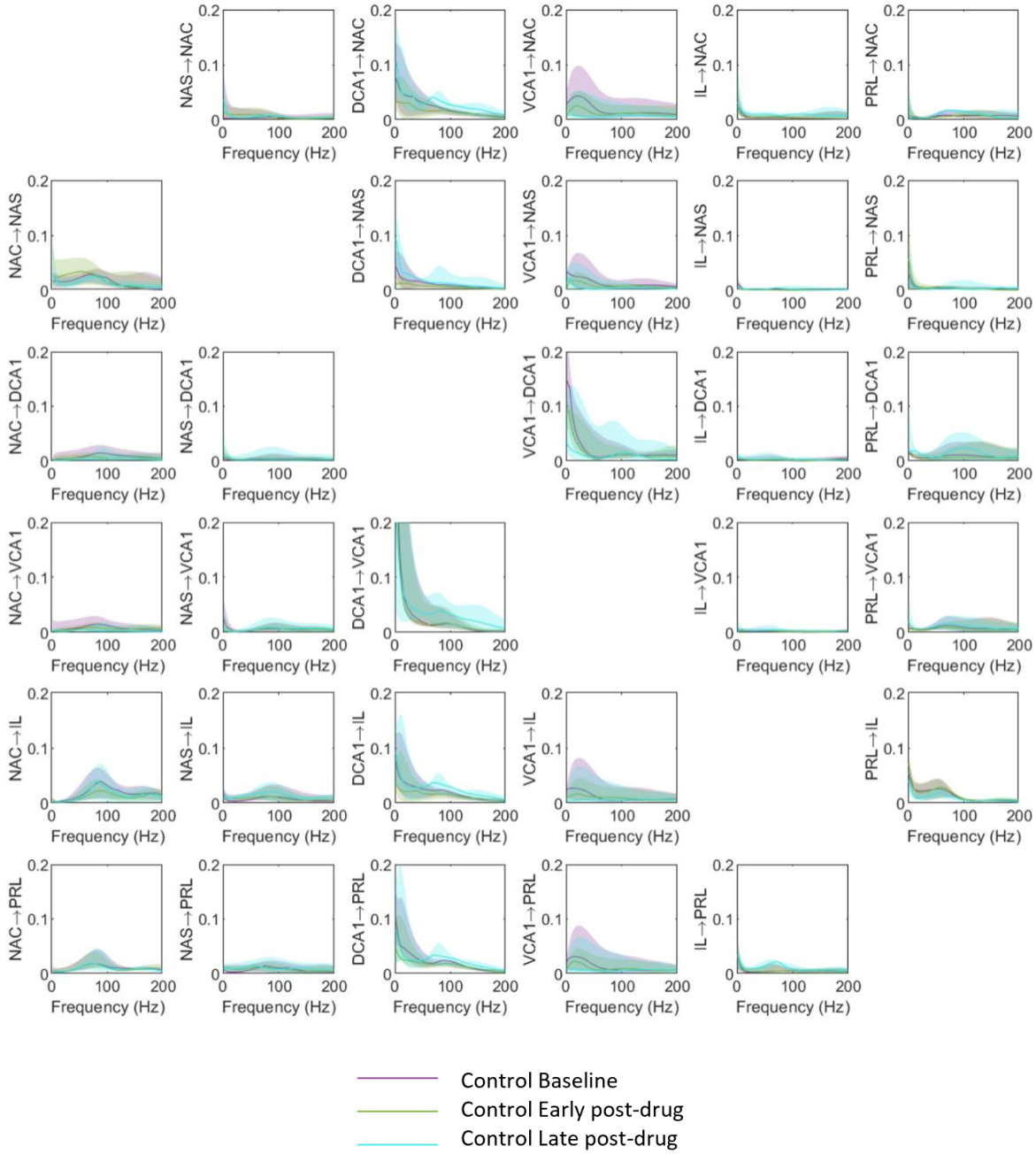

The median +/- interquartile range of Granger causality in the control condition is plotted across animals (n=4) for each pair of regions. For each connection Granger causality is calculated for each direction, with the plot for the same connection in the opposite direction located in the symmetrical location across the diagonal in the panel. Each plot shows the Granger causality for the baseline, early post-drug and late post-drug period coloured according to the key at the bottom of the panel.

Figure 4.20: Cortico-striatal spectral Granger causality by region pair and frequency in the 25I condition

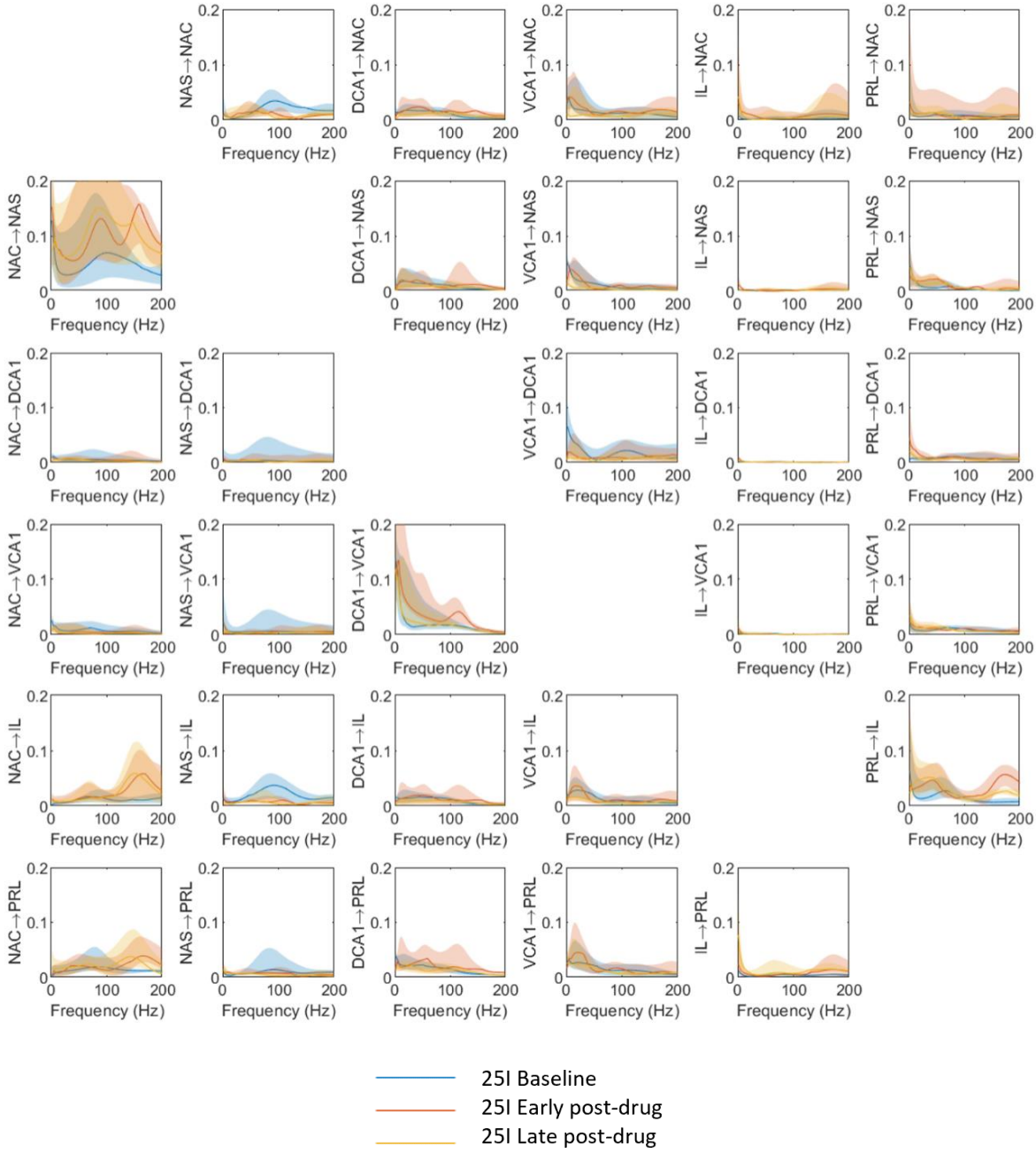

The median +/- interquartile range of Granger causality in the 25I condition is plotted across animals (n=4) for each pair of regions. For each connection Granger causality is calculated for each direction, with the plot for the same connection in the opposite direction located in the symmetrical location across the diagonal in the panel. Each plot shows the Granger causality for the baseline, early post-drug and late post-drug period coloured according to the key at the bottom of the panel.

In the control condition in both experiments (Figures 4.17 and 4.19) there are minimal changes in Granger causality from baseline to early or late post-drug periods. In the cortico-limbic experiment there is a small increase in Granger causality in the late post-drug period from DCA1 to all other regions in the high gamma band, but interactions otherwise remain stable across the three time points. The level of Granger causality between NAC to NAS is markedly lower in the control experiment than in the 25I experiment at baseline (Figures 4.19 and 4.20).

In the cortico-striatal experiment (Figure 4.19), theta oscillations show a strong directional flow from DCA1 and VCA1 to all other brain regions, with an even stronger effect seen in delta from DCA1 alone. In the cortico-limbic experiment (Figure 4.17) the hippocampal theta has a clear directional flow to IL and PRL but not to BLA. In the control condition the BLA demonstrates a directional flow of beta/low gamma to all other brain regions, and connectivity of equal magnitude in the HFO range, which is reciprocated in the signal from IL. The presence of significant Granger causality in the HFO range was unanticipated in the control condition and suggests that HFO may have a physiological role in the function of the cortico-limbic circuit.

In the cortico-limbic experiment (Figure 4.17) the connection from PRL to IL shows wide variability, whilst the connection from IL to PRL shows a clear peak in Granger causality in the high gamma range. In the cortico-striatal experiment (4.19) a high gamma peak is again visible in in both directions between PRL and IL, and in the connection from NAC to the prefrontal regions.

4.3.9. 25I increases activation of a cortico-limbic loop between prefrontal cortex and BLA.

25I causes substantial increases in directed functional connectivity across both experiments, with specific frequencies characterising the connections between different regions (Figures 4.18 and 4.20).

There is a large increase in Granger causality from IL to BLA in the gamma and HFO bands. Whilst there are reciprocal increases these are of a much smaller magnitude, indicative of increased top-down drive from IL to BLA (Figure 4.18). The control experiments also show directed connectivity between IL and BLA, however, the magnitude is similar in each direction and remains stable over the course of the experiment (Figure 4.17). There is a clear increase in Granger causality from IL to PRL in the HFO band, which is not seen in the other direction, suggesting an increased drive from IL to PRL (Figure 4.18). Conversely, the cortico-striatal experiment shows an increase in Granger causality from PRL to IL in the HFO band, suggesting that communication between these regions is bidirectional (Figure 4.20). There is

an increase in gamma and HFO band Granger causality from the BLA to PRL which is not seen in the opposite direction supporting directionality from the BLA to the PRL (Figure 4.18). Taken together these findings support increased communication within a directed cortico-limbic circuit from IL to BLA and back to PRL, representing a potential means through which 5-HT_{2A} agonists and potentially ketamine may exert antidepressant effects.

4.3.10. Granger causality analysis supports a directed flow of HFO from the NAC to the prefrontal cortex

In the cortico-striatal experiments there is an increase in Granger causality in the HFO band from NAC to PRL and NAC to IL that is of greater amplitude than that seen in the opposite direction, supporting the NAC driving prefrontal HFO (Figure 4.20). In contrast with the BLA, the connectivity of the NAC and prefrontal cortex does not have a strong gamma component. There is also a clear increase in the HFO band from NAC to NAS, with a reciprocal reduction in Granger causality in the other direction.

4.3.11. 25I increases cortico-limbic and cortico-hippocampal communication

To enable statistical analysis of the effects of 25I on coherence and spectral Granger causality over time, band-limited values were calculated for each measure. In this section, changes in coherence (undirected functional connectivity; ΔCoh) and Granger causality (directed functional connectivity; ΔGC) relative to baseline are compared between the control and 25I conditions.

The difference between the change in ΔCoh and ΔGC in the 25I condition relative to control is shown for the early post-drug period in Figure 4.21 and for the late post-drug period in Figure 4.22. These figures show the functional connectivity measures by region and frequency band for each experiment and summarise the direction of change using the W statistic (methods Section 4.2.5). Statistical testing of ΔCoh is reported where data was normally distributed and the figure is marked where testing was not performed due to non-parametric distribution. Due the non-parametric distribution of Granger causality there was not sufficient statistical power to test for significant differences in the ΔGC.

Figure 4.21: Changes in frequency domain functional connectivity from baseline to the early post-drug period

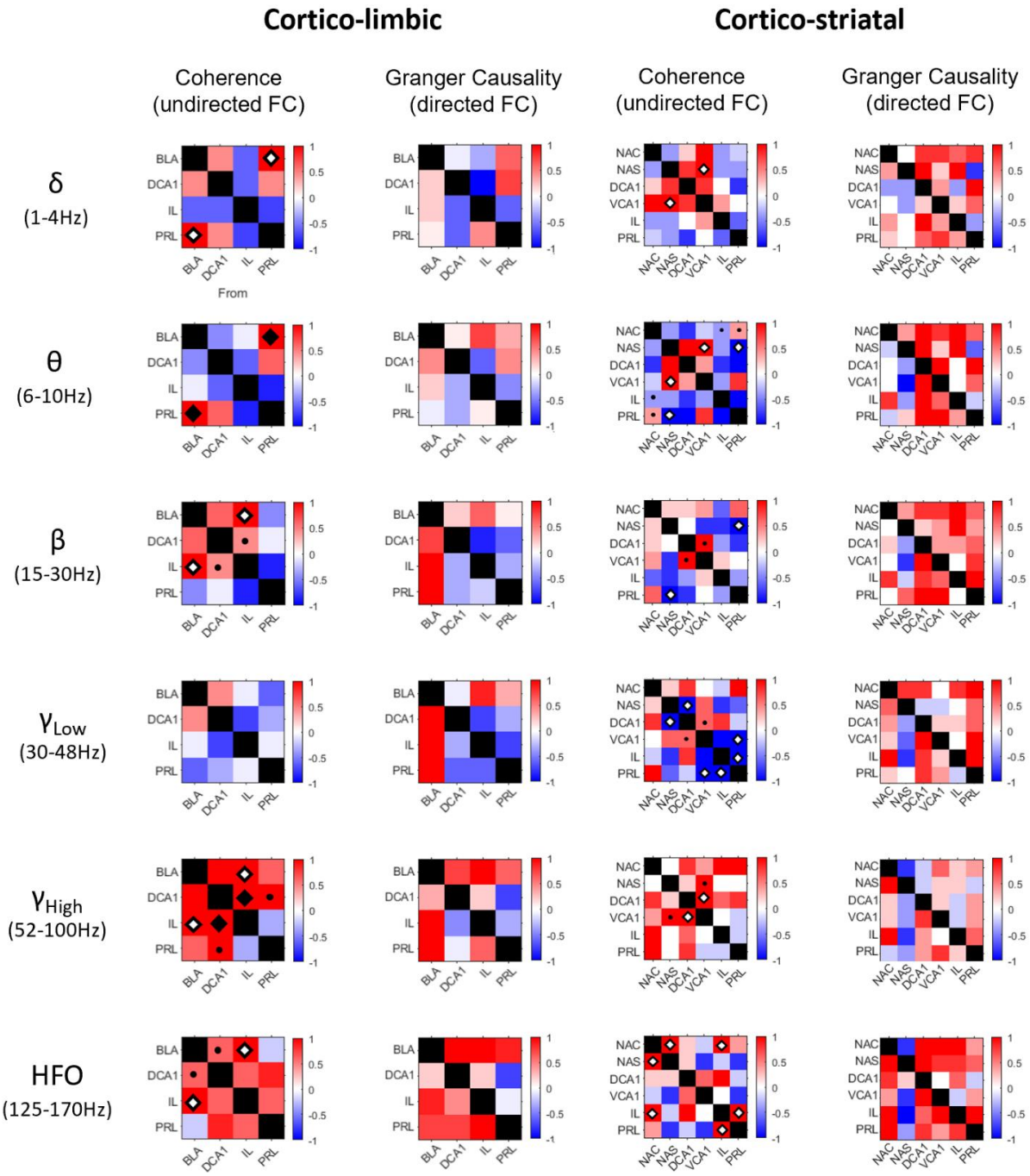

The colour of each grid square represents the difference between the change in FC from baseline (ΔFC) between the 25I (ΔFC_{25I}) and control condition ($\Delta FC_{Control}$). The data is presented using the W statistic from the Wilcoxon signed rank test normalised to a value between -1 and 1 (see Methods 4.2.5) and is presented on a colour scale from red to blue, with blue representing a decrease in FC in the 25I condition relative to control, and red representing an increase in FC in the 25I condition relative to control. Undirected FC is symmetrical between region pairs, however, directed FC varies depending on whether it is inbound or outbound. The direction for directional FC is always read as from the region on the X axis, to the region on the Y axis. Open diamonds indicate a significant difference between ΔFC_{25I} and $\Delta FC_{Control}$ on a two tailed paired T-test ($p<0.05$) prior to FDR adjustment. Closed black diamonds indicate significance tests that remained significant at ($p<0.05$) following FDR adjustment. Where no symbol is shown in the coherence plots, a T-test was performed but did not reach the threshold for significance ($p<0.05$). Black dots indicate comparisons where data was non-parametric and significance testing was not performed. Significant testing was not performed for directed FC (see Methods 4.2.5).

Figure 4.22: Changes in frequency domain functional connectivity from baseline to the late post-drug period

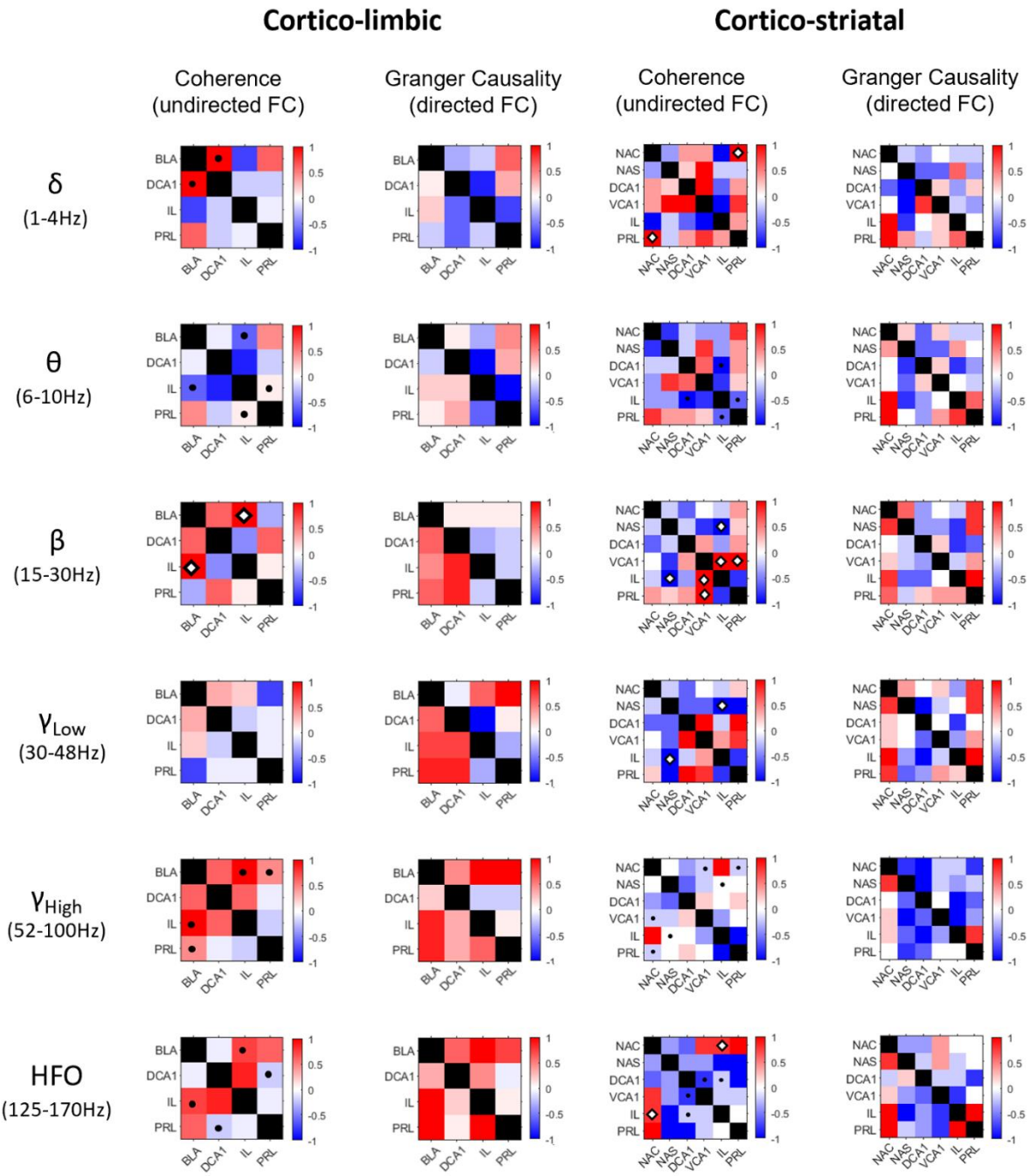

The colour of each grid square represents the difference between the change in FC from baseline (ΔFC) between the 25I (ΔFC_{25I}) and control condition ($\Delta FC_{Control}$). The data is presented using the W statistic from the Wilcoxon signed rank test normalised to a value between -1 and 1 (see Methods 4.2.5) and is presented on a colour scale from red to blue, with blue representing a decrease in FC in the 25I condition relative to control, and red representing an increase in FC in the 25I condition relative to control. Undirected FC is symmetrical between region pairs, however, directed FC varies depending on whether it is inbound or outbound. The direction for the directional FC is always read as from the region on the X axis, to the region on the Y axis. Open diamonds indicate a significant difference between ΔFC_{25I} and $\Delta FC_{Control}$ on a two tailed paired T-test ($p<0.05$) prior to FDR adjustment. Closed black diamonds indicate significance tests that remained significant at ($p<0.05$) following FDR adjustment. Where no symbol is shown in the coherence plots, a T-test was performed but did not reach the threshold for significance ($p<0.05$). Black dots indicate comparisons where data was non-parametric and significance testing was not performed. Significant testing was not performed for directed FC (see Methods 4.2.5).

Prior to FDR correction in the early post-drug period the cortico-limbic experiment (Figure 4.21) showed significant increases in ΔCoh for 25I relative to control between PRL and BLA in the delta and theta bands, significant increases between IL and BLA in the beta, high gamma and HFO bands, and significant increases between DCA1 and IL in the high gamma band. The increased theta coherence between BLA and PRL, and the increased high gamma coherence between DCA1 and IL remained significant following FDR correction. In the late post-drug period (Figure 4.22), there was a significant increase in ΔCoh for 25I relative to control between IL and BLA in the beta band, although this was no longer significant following FDR.

In the early post-drug period (Figure 4.21) increases in ΔGC for 25I relative to control demonstrated increased directed output from the BLA to all other regions from the beta to HFO bands, with increasing inbound ΔGC from all other regions in the high gamma and HFO bands. Increases in directed output from the BLA persisted in the late post-drug period (Figure 4.22). Reductions in ΔGC in both directions between prefrontal cortex and DCA1 were seen in the beta and high gamma bands (Figure 4.21) with similar findings seen in the cortico-striatal experiments in the late post-drug period (Figure 4.22).

These findings support activation of 5-HT_{2A} receptors by 25I driving increased coordination within both cortico-limbic and cortico-hippocampal circuits. Although not significant there was also a trend of reduced coherence between IL and PRL across the delta, theta, and beta bands, suggesting disruption of normal cortical dynamics.

4.3.12. 25I increases cortico-striatal and prefrontal functional connectivity across a wide range of frequencies

In the early post-drug period, the cortico-striatal experiment showed significant increases in ΔCoh for 25I relative to control between NAS and VCA1 in delta and theta bands, significant increases between VCA1 and DCA1 in the high gamma band, and significant increases in coherence between NAC and IL, NAC and NAS, and IL and PRL in the HFO band. There were also significant decreases in ΔCoh for 25I relative to control between NAS and PRL in the theta and beta bands, and significant decreases between DCA1 and NAS, VCA1 and PRL and between IL and PRL in the low gamma band. None of these associations remained significant after FDR correction, however, the cortico-striatal experiment was underpowered for correction of multiple comparisons (n=4). In the early post-drug period ΔGC demonstrated broadband increases in directed functional connectivity for 25I relative to control, except for the NAS which showed reductions in outbound ΔGC across almost all frequency bands and region pairs.

In the late post-drug period, the cortico-striatal experiment showed significant increases in ΔCoh for the 25I condition relative to control between NAC and PRL in the delta band, between VCA1 and IL and VCA1 and PRL in the beta band. There were corresponding decreases in ΔCoh for the 25I condition relative to control between IL and NAS across the beta and low gamma bands. The significant increase in ΔCoh for the 25I condition relative to control between NAC and IL seen in the early post-drug period remained significant in the HFO band. None of these changes were significant following FDR correction. In the late post-drug period, the changes in ΔGC for 25I relative to control were largely reversed, except for the NAC which continued to show strong increases in outbound ΔGC to IL and PRL across the full frequency spectrum, and to NAS from theta to HFO frequencies. Increases in ΔGC from PRL to IL remained across all frequencies from theta and gamma to HFO, and from IL to PRL in the theta and HFO range.

4.3.13. Undirected and directed functional connectivity measures in the frequency domain showed dissociable patterns of drug-induced changes

To test the hypothesis that changes in frequency-domain undirected functional connectivity (ΔCoh) and directed functional connectivity (ΔGC) induced by 25I would move in the same direction, rank correlation was calculated using Kendall's Tau. Correlation coefficients were calculated between the effects of 25I on undirected (ΔCoh_{25I}- $\Delta Coh_{Control}$) and directed (ΔGC_{25I}-$\Delta GC_{Control}$) functional connectivity for each region pair and direction with the results illustrated graphically in Figure 4.23.

Analysis of correlation showed mixed results, with some region pairs showing correlation between undirected and directed functional connectivity and others showing anticorrelation. In the early post-drug period in the cortico-limbic experiment there was a significant positive correlation between undirected and directed functional connectivity from IL to PRL in the delta band, and from DCA1 to IL in the theta band. In the early post-drug period in the cortico-limbic experiment there was a significant negative correlation from IL to PRL in the beta band. In the late post-drug period in the cortico-limbic experiment there was a significant negative correlation between undirected and directed functional connectivity from IL to PRL in the HFO band. None of these tests remained significant after FDR, and with 3 of 72 (4.2%) significance tests in the early post-drug period, and 1 of 72 (1.4%) significance tests being significant in the late post-drug period it is likely that these correlations were due to chance.

Figure 4.23: Correlation between the change in undirected and directed frequency domain functional connectivity

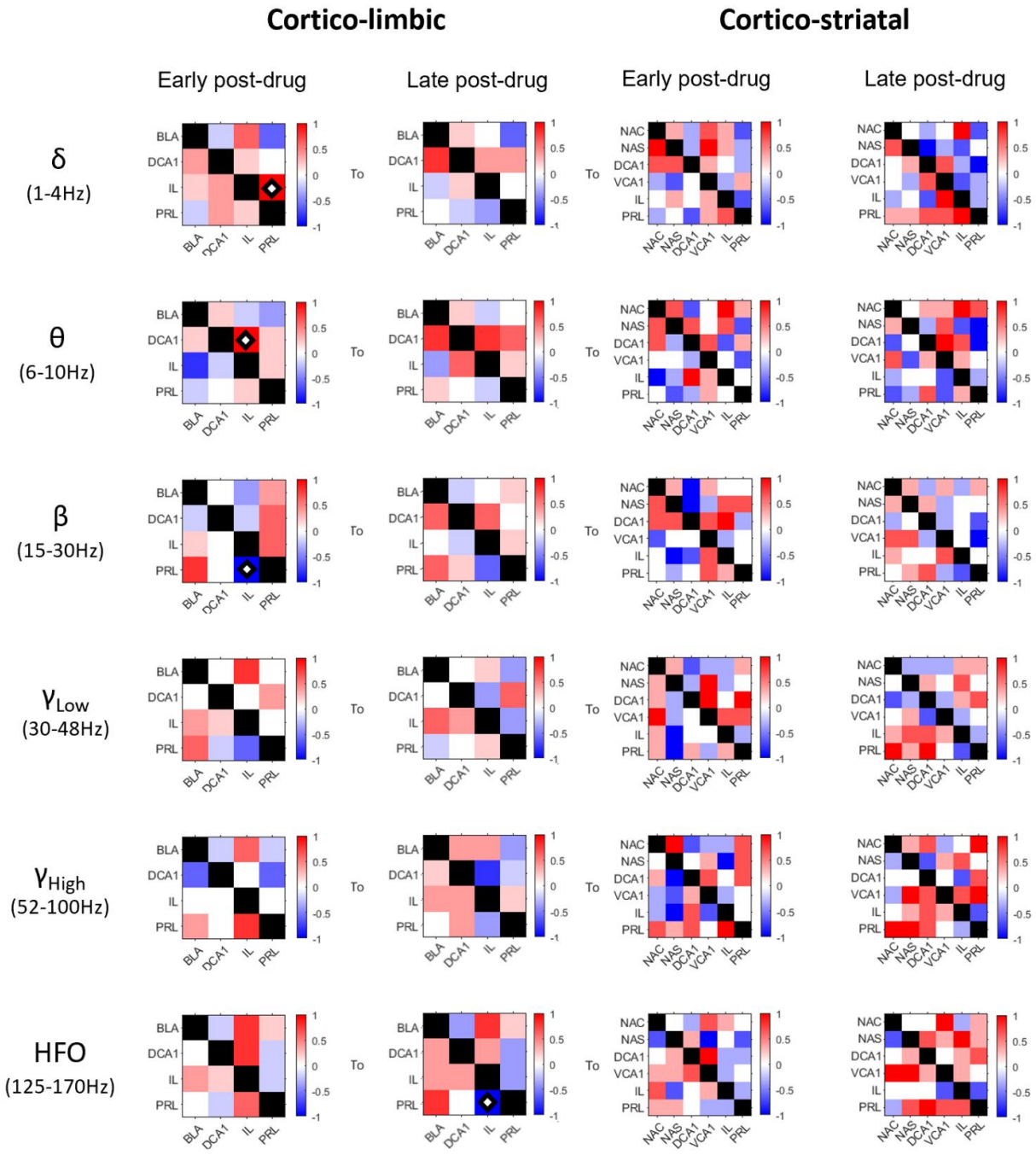

The colour of each grid square represents the rank correlation coefficient between the effect of 25I on undirected FC (ΔCoh_{25I}- $\Delta Coh_{Control}$) and directed FC (ΔGC_{25I}- $\Delta GC_{Control}$) calculated using Kendall's Tau. Correlations are shown between undirected FC and each component of the directed FC. The direction of the connection for the directed FC is always read as from the region on the X axis, to the region on the Y axis. Open diamonds indicate that the strength of rank correlation is likely to be significant ($p<0.05$). None of the significance tests remained significant following FDR adjustment.

4.4. Discussion

4.4.1. Key findings

During development of the functional connectivity analysis pipeline it became apparent that this dataset did not provide sufficient power for stringent statistical testing. This was particularly apparent with respect to the implementation of the Granger causality Toolbox due to the necessity to use non-parametric significance testing for frequency domain Granger causality. Due to the reduced statistical power common to non-parametric tests this meant it was not possible to test for significant differences in Granger causality meaning Granger causality could only be reported at trend level. Tabular summaries of the significant findings from the analysis of spectral power (Table 4.5), correlation (Table 4.6), and coherence (Table 4.7) are presented below. Despite the limitations of statistical testing, setting both trend and significant effects of 25I on coordinated cortico-limbic and cortico-striatal activity in the context of the literature supports a range of preliminary conclusions.

Table 4.5: Summary of significant changes in spectral power

Experiment	Regions	Early	Late
Cortico-limbic	BLA	↓ low gamma	-
	DCA1	-	-
	IL	↓ low gamma and beta; ↑HFO	-
	PRL	↑ HFO	-

Summary of regions that demonstrated a significant difference between $\Delta Power_{25I}$ and $\Delta Power_{Control}$ on a two tailed paired T-test ($p<0.05$) prior to FDR; none of these findings remained significant following FDR correction.

Table 4.6: Summary of significant changes in undirected temporal domain functional connectivity (correlation)

Experiment	Regions	Early	Late
Cortico-limbic	BLA-DCA1	-	↑
Cortico-striatal	NAS-DCA1	↓	-
	DCA1-PRL	↓	-

Summary of regions that demonstrated a significant difference between ΔFC_{25I} and $\Delta FC_{Control}$ on a two tailed paired T-test ($p<0.05$) prior to FDR; none of these findings remained significant following FDR correction.

Table 4.7: Summary of significant changes in undirected frequency domain functional connectivity (coherence)

Experiment	Regions	Early post-drug period	Late post-drug period
Cortico-limbic	BLA-PRL	↑ delta and theta*	-
	BLA-IL	↑ beta, high gamma and HFO	↑ beta
	DCA1-IL	↑ high gamma*	-
Cortico-Striatal	NAC-NAS	↑ HFO	-
	NAC-IL	-	↑ HFO
	NAC-PRL	-	↑ delta
	NAS-DCA1	↓ low gamma	-
	NAS-VCA1	↑ delta and theta	-
	NAS-IL	↑ HFO	↓ beta and low gamma
	NAS-PRL	↓ theta and beta	-
	DCA1-VCA1	↑ high gamma	-
	VCA1-IL	↓ low gamma	↑ beta
	VCA1-PRL	↓ low gamma	↑ beta
	IL-PRL	↑ HFO coherence	-

Summary of regions that demonstrated a significant difference between ΔFC_{25I} and $\Delta FC_{Control}$ on a two tailed paired T-test ($p<0.05$) prior to FDR; (*) indicates findings that remained significant following FDR correction.

4.4.2. Increases in HFO power in the nucleus accumbens, prefrontal cortex and basolateral amygdala extend known findings in the literature

Spectral analysis confirmed the emergence of HFO in the nucleus accumbens following treatment with 5-HT_{2A} agonists (Goda et al., 2013) and extended this finding to show concurrent induction of HFO in the prefrontal cortex and BLA. Changes in power appear to be biphasic between the early and late post-drug period, highlighting the importance of a clear understanding of the pharmacokinetics of 5-HT_{2A} agonists in interpreting research findings. Biphasic changes in spectral power have previously been reported in a rodent EEG study using the psychedelic drug 2C-B (Páleníček et al., 2013). Early suppression of beta power was seen in IL, and suppression of low gamma power in both BLA and IL. These reductions in gamma power are in keeping with published reports of reductions in prefrontal low gamma power following DOI in rats (Wood et al., 2012), and reductions in prefrontal human beta and gamma in human EEG findings and MEG data (Riba et al., 2002, Barnett et al., 2020).

4.4.3. Time domain functional connectivity has a clear role in functional connectivity analysis

Time domain functional connectivity analysis identified the change in directed connectivity from the NAC to NAS and prefrontal cortex and showed increased cortico-limbic communication. Of the significant findings from the analysis of undirected time domain functional connectivity, only the reductions in undirected functional connectivity between DCA1 and NAS were identified in both the time domain and frequency domain analyses. Significantly increased correlation between BLA and DCA1 was identified, representing broadband increases in coherence across all bands except theta, and reductions in correlation between DCA1 and PRL were also identified representing broadband reductions across all frequency bands with the exception of high gamma which showed increased correlation. Prefrontal cortex and hippocampus are both components of the DMN (Hsu et al., 2016), with reduced connectivity within the DMN reported in response to a variety of antidepressant agents including 5-HT_{2A} agonists, ketamine, SSRIs, and MDMA (Müller et al., 2020, Pasquini et al., 2020, Zacharias et al., 2020).

The ability of the time-domain analyses to detect associations that were not significant in the frequency-domain analyses was unanticipated. Review of the plots of coherence and frequency domain Granger causality (Figures 4.15 to 4.20) highlights the contributions of multiple frequencies in many of the region pair associations. The time domain analyses captured these broader patterns of synchronization and message passing and provides additional information over the use of frequency domain functional connectivity alone. Frequency domain functional connectivity is inherently easier to calculate and describe which carries obvious benefits. Indeed, much of the functional connectivity analysis in functional MRI studies is based upon changing patterns of correlation between voxels or regions of interests (ROI) alone.

4.4.4. Frequency domain functional connectivity is informative in baseline and control conditions as well as under the effects of 25I

Analysis of undirected and directed functional connectivity in the baseline period and control condition provides insights about the anatomical and physiological relationships between regions. In the cortico-striatal experiments, the importance of theta coupling within in the hippocampus (Montgomery et al., 2009) is shown as a spike in high coherence between DCA1 and VCA1, whilst Granger causality analysis highlights that theta oscillations show the outbound directed causality from the hippocampus throughout the cortico-limbic and cortico-striatal circuits (Thierry et al., 2000, Siapas et al., 2005). Whilst the role of hippocampal theta

is well established in the literature, a similar approach applied to less studied brain regions may provide significant insights with regards to oscillatory coupling. In the cortico-striatal experiments NAC demonstrated higher coherence than NAS with both PRL and IL, with this finding potentially supported by reports of greater density of projections from PRL and IL to medium spiny neurons in the NAC rather than NAS (Li et al., 2018).

In a comprehensive review of the development of Granger causality in neuroscience, Seth states that "In general, [Granger causality analysis] is better suited to revealing differences in directed functional connectivity between experimental conditions than to characterizing these connectivity patterns per se" (Seth et al., 2015). Comparison between experimental conditions controls against the detection of temporal dependencies from sources extraneous to the experimental design (Friston et al., 2013) such as regional variation in haemodynamics in fMRI studies (David et al., 2008). Given the high temporal and spatial resolution of implanted electrodes, interpretation of baseline Granger causality is likely to be less problematic providing the data is free of recording artefacts. As discussed in the paragraph above, the frequency-domain Granger causality analyses in the baseline and control conditions in this study provide substantial information about signal flow within the circuits of interest that are supported by the wider literature.

The presence of HFO peaks in Granger causality at baseline between BLA and IL, and between IL and PRL, were unexpected but suggest that HFO may have a physiological role outside of that described following pharmacological manipulation. Indeed recent work has shown that the emergence of HFO following ketamine is dependent on nasal respiration in rats, and draws links between this finding and olfactory bulbectomy models of depression in rodents (Wróbel et al., 2020).

4.4.5. 25I causes marked changes in the functional connectivity of the cortico-limbic, cortico-striatal, and cortico-hippocampal circuits with NAC driving changes in HFO activity

Based on findings from both temporal and spectral Granger causality, the nucleus accumbens appears to take on a driving role following 25I administration. Directed functional connectivity in the HFO range increased in the 25I condition from NAC to IL, PRL and NAS at both early and late time points, with accompanying increases in coherence between NAC and IL. These findings support the NAC as the source of HFO within the cortico-striatal network.

Granger causality analysis of the cortico-limbic circuit shows increases in directed connectivity in the HFO range from IL to BLA, and from IL to PRL with BLA in turn showing directed connectivity back to PRL. This suggests a putative neural circuit with HFO originating in the

nucleus accumbens and passing to the IL cortex to drive HFO in the BLA which in turn feedback to prefrontal cortex. In the case of subanaesthetic ketamine, Granger causality analysis has shown that the olfactory bulb in turn drives HFO in NAC with the authors highlighting the potential significance in relation to olfactory bulbectomy models of depression in rodents (Hunt et al., 2019).

In contrast to the increase in directed functional connectivity from the NAC to other regions, the NAS demonstrated reductions in outbound Granger causality across all frequency ranges, despite increases in coherence with VCA1 in the theta range and DCA1 in the gamma range. The expression of 5-HT_{2A} receptors is reported to vary within the nucleus accumbens with greater expression in the shell than the core, providing a possible explanation for the markedly different effects (Mijnster et al., 1997).

4.4.6. Changes in undirected and directed functional connectivity measures do not routinely show strong positive associations

Counter to the hypothesis that undirected and directed functional connectivity would show changes in the same direction, there was no evidence of a consistent relationship between the size of the changes between the 25I and control conditions in undirected and directed functional connectivity in either experiment in the time or frequency domain. This aligns with the finding previously reported in analysis of human MEG data (Barnett et al., 2020) and highlights the importance of using both undirected and directed approaches when describing functional connectivity.

4.4.7. Limitations of the study

Due to the use of a pre-existing dataset, the numbers of animals included in the present analyses was limited. In both experiments the study was insufficiently powered to find non-parametric changes in statistical significance, limiting the ability to interpret the directed functional connectivity analyses. The number of region pairs and frequency bands characterised in the study necessitated the use of correction for multiple testing, however, the study was underpowered to show effects following FDR.

The multivariate nature of the Granger causality and other measures meant it was not possible to pool across animals even where regions were present in both experiments. Whilst pooling of data could be done with bivariate measures, this would be likely to introduce spurious associations through shared dependence between regions (Kuś et al., 2004). A reduced multivariate model using regions shared between experiments (IL, PRL, DCA1) would also be

a possibility, however, it was felt that this approach was likely to introduce more issues in interpretation than it would solve in this dataset, given it would also require inclusion of the strain of the animal as a covariate in the analyses.

To my knowledge the pharmacokinetics of i.p. 25I in rodents has not yet been established. A greater understanding of how the pharmacokinetics of 25I compared with those of psilocybin, DOI and LSD would enable clearer comparison of findings between studies. The selection of early and late post-drug periods was based largely upon the data available, however, it is clear from the spectrograms (Figures 4.7 and 4.8) that the effects of 25I continued beyond the end of the recording. Therapeutic use of 5-HT_{2A} agonists suggests that they result in persistent changes in depressive symptoms (Carhart-Harris et al., 2018a) long beyond the duration of the drug itself. Follow-up recordings would be beneficial in determining whether there are persistent changes in functional connectivity following treatment with 5-HT_{2A} agonists.

4.4.8. Further work

The approach to functional connectivity analysis presented in this chapter provided compelling insights into the functional anatomy of the cortico-limbic and cortico-striatal circuits, in both the control and 25I conditions, despite the limitations associated with using a pre-existing dataset. An extension of the approach used in the present study to explore the effects of 5-HT_{2A} agonists would be of significant scientific interest, ideally combining recording sites across both cortico-limbic and cortico-striatal circuits. Comparison with subanaesthetic ketamine may yield further insights into the pharmacological actions of rapid acting antidepressants.

The approach demonstrated the ability to deploy multivariate functional connectivity analysis on multielectrode LFP recordings across delta to HFO frequencies with relatively short epochs of data (2-10 seconds). In combination with a comprehensive video-driven analysis of behaviour this approach has the potential to yield substantial insights into neurophysiology under a range of experimental conditions.

In this study healthy rats were used; however, anxiety and depression are known to cause changes in functional connectivity in cortico-limbic, cortico-striatal and cortico-hippocampal pathways (Martin et al., 2009, Siegle et al., 2007, Godsil et al., 2013). How the effects of 5-HT_{2A} agonists interact with the underlying changes in functional connectivity in a rodent model of depression is not yet known and would be an important step forward in determining the pharmacological basis of 5-HT_{2A} agonists as antidepressants.

Whilst functional connectivity measures provide a description of the statistical associations between LFP data from different regions, they are unable to provide insight into the underlying

mechanisms. In the following chapter effective causality analysis is employed using dynamic causal modelling (DCM), in an attempt to both replicate the findings of the functional connectivity analysis and to explore the potential for mechanistic inference relating to the underlying neurophysiological changes generating the spectral data described in this chapter (Moran et al., 2013).

Chapter 5. Systemic 5-HT_{2A} activation modulates effective connectivity in the cortico-limbic network

5.1. Introduction

In Chapter 4, spectral analysis and functional connectivity approaches were used to quantify the effects of 25I upon the cortico-limbic, cortico-striatal and cortico-hippocampal circuits. In this chapter an effective connectivity approach is applied to the same data using the framework of dynamic causal modelling (DCM).

Functional connectivity describes how statistical dependencies between neuronal signals vary over time, or across experimental conditions, but does not attempt to describe or infer the underlying neural mechanisms. In contrast, effective connectivity attempts to describe the relationship between neuronal signals in terms of parameters that describe neural activity in electrophysiological terms. Effective connectivity is described by Karl Friston as a description of "the influence that one neural system exerts over another, either at a synaptic or population level" (Friston, 2011). An earlier description describes effective connectivity as "the experiment and time-dependent, simplest possible circuit diagram that would replicate the observed timing relationships between the recorded neurons'' (Aertsen and Preissl, 1991).

DCM is a family of generative models that can be applied to electrophysiological (LFP, EEG, MEG) data or to functional MRI, although there are substantial differences in approach between DCM for electrophysiological signals and fMRI (Stephan et al., 2010, Friston et al., 2012, Kahan and Foltynie, 2013). DCM requires the specification of an anatomical model, or models, that are built up of one or more interconnected sources (brain regions). Each source has a defined internal structure consisting of different neural populations connected by intrinsic connections. For cross-spectral density (CSD) DCM, the network is activated by white/pink noise with steady state spectral responses derived from the transfer functions (Moran et al., 2013). The DCM models are inverted (the model parameters are fitted to the empirical data) through an iterative process using the principal of free-energy maximization to fit the model to the spectral data (Daunizeau et al., 2011).

Proof of concept in the use of DCM to explore the effects of pharmacological agents on LFP data in rats has come from previous work in the Jones lab, where DCM has been used to interpret the effects of ketamine on effective connectivity. This study looked at effective connectivity between the dorsal hippocampus and the medial prefrontal cortex of rats using data collected with a similar experimental approach to the data used for this thesis (Moran et al., 2015). It demonstrated reduced top-down drive from the prefrontal cortex to hippocampus

following administration of ketamine with the action at postsynaptic NMDA receptors responsible for the changes seen (Moran et al., 2015).

The approach taken in this chapter had three main aims:

1) To assess the ability of DCM models to fit high frequency spectral data.

2) To test hypotheses about the anatomical connections in the cortico-limbic system.

3) To provide a comparison with the measures of functional connectivity described in Chapter 4.

The secondary intention of this chapter was to develop expertise in the use of DCM models in preparation for future studies. To my knowledge, DCM has not previously been applied to high frequency electrophysiological data in the HFO range and has not previously been used to describe the effects of 5-HT_{2A} agonists in rats.

5.2. Methods

In this chapter I apply DCM for cross-spectral densities using the implementation in the SPM12 package for MATLAB (Friston et al., 2012).

Due to the subcortical nature of the nucleus accumbens, DCM modelling of the cortico-striatal dataset presents substantial challenges. The neural mass models in DCM are predominantly based upon a laminar cortical structure, although can be reasonably applied to the basolateral amygdala which, whilst not arranged as a laminar structure, is ‘cortex-like’ in that it contains functionally analogous neuronal populations (Muller et al., 2006). In contrast the nucleus accumbens primarily consists of GABAergic neurons that in turn project onto GABAergic neurons in the ventral pallidum before synapsing in the medio-dorsal nucleus of the thalamus which projects back to prefrontal cortex (Scofield et al., 2016, Root et al., 2015). This cortico-striatal loop does not easily translate into the models commonly used in DCM (Moran et al., 2013). The analysis presented in the rest of this chapter therefore relates solely to modelling the effective connectivity of the cortico-limbic and cortico-hippocampal circuits using data collected in the cortico-limbic experiment described in Chapter 2.

Comparison of models within the DCM framework requires the specification of a suitable model space. This includes specifying the experimental model and design, specifying the equations for the neural mass models, and specifying the anatomical models to be tested.

5.2.1. Neural mass models

Four neural mass models (ERP, LFP, CMM and CMM_NMDA) were compared to determine which provided the best trade-off of accuracy and complexity in fitting the spectral data (Stephan et al., 2009). As DCM has not previously been used with HFO, there was no prior data to suggest one model over another. The ERP and LFP models are convolution-based approaches to DCM (David and Friston, 2003) and are based on a trilaminar model of the cortex. These models each have three neuronal populations representing pyramidal output neurons, spiny stellate cells and GABAergic interneurons (Moran et al., 2013, David and Friston, 2003). A summary of the model architecture is shown in Figure 5.1.

In contrast to the ERP and LFP models, the CMM and CMM_NMDA models are based on a four-population model of the cortex and separate the pyramidal neurons into superficial and deep populations (Bastos et al., 2012). Superficial pyramidal cells are the source of forward connections, whilst deep pyramidal cells are the source of backward connections (Bastos et al., 2012). The CMM and CMM_NMDA models differ from the ERP models in being conductance-based rather than convolutional and differ from one another by the inclusion of NMDA receptor activity in the CMM_NMDA model (Marreiros et al., 2009, Moran et al., 2013). While the anatomical model for the CMM_NMDA model is specified in the same way as the neural mass models, it contains an additional set of extrinsic connectivity parameters in order to distinguish the effects of glutamate at AMPA and NMDA receptors. A summary of the key characteristics of each model is provided in Table 5.1.

Table 5.1: Characteristics of neural mass models

Neural mass model	Type of model	Populations	Glutamate receptors modelled
ERP	Convolution-based	3-population	AMPA
LFP	Convolution-based	3-population	AMPA
CMM	Conductance-based	4-population	AMPA
CMM_NMDA	Conductance-based	4-population	AMPA and NMDA

Figure 5.1: Overview of connections in ERP and LFP neural mass models

Neural mass model of a single neural source consisting of pyramidal cells (Pyr), inhibitory interneurons (II) and spiny stellate cells (SS). Intrinsic (within source) excitatory glutamatergic connections are shown in green and intrinsic GABAergic inhibitory connections are shown in the red. The self-inhibitory connection from II is only present in the LFP model and distinguishes LFP from ERP models.

Long-range glutamatergic extrinsic (between source) connections originate from pyramidal cells and terminate in other sources as specified in the DCM model. Forward connections terminate at spiny stellate cells and have a driving effect, whilst backwards connections terminate at both pyramidal cells and inhibitory interneurons and have a modulatory effect.

For further details of the underlying models and the associated neural state equations refer to Moran et al. (Moran et al., 2013).

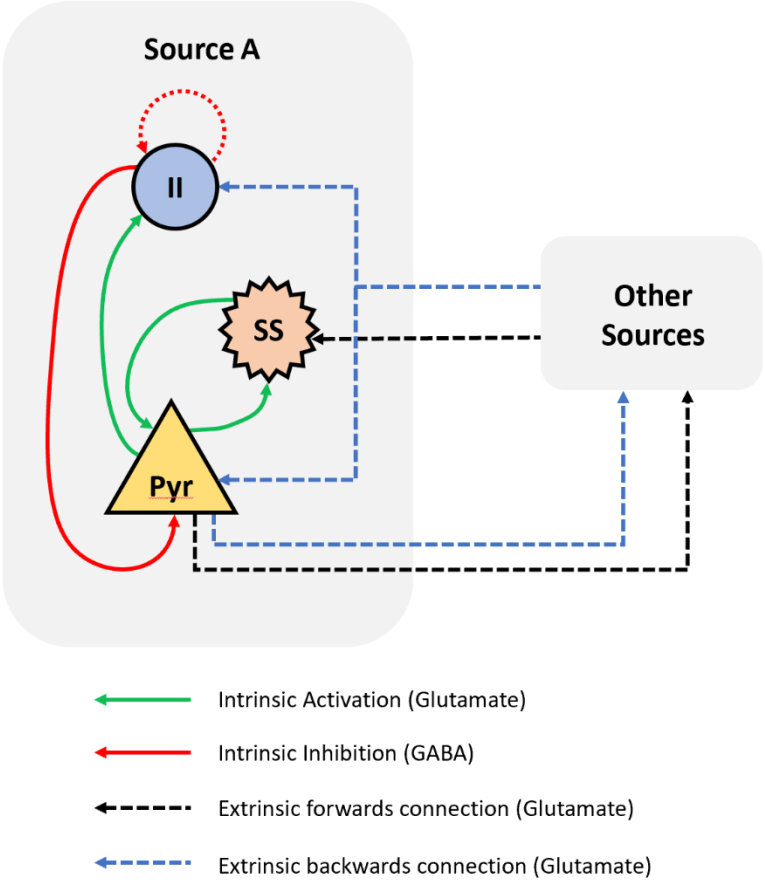

5.2.2. Anatomical models

Due to the vast range of potential models that could be specified, it was necessary to define some constraints on the anatomical models. In line with previous work using LFP data, each pair of anatomical regions could be linked by a forward connection, or a backward connection (but not both) providing there was sufficient experimental evidence for a connection between regions (Moran et al., 2015). The data used for this analysis was collected from the right hemisphere and so lateral connections (representing inter-hemispheric connections) between regions were not used.

Based on the existing literature on connections in the cortico-limbic circuit (see Figure 1.2) and the findings from the functional connectivity analysis, the anatomical hypotheses were defined and used to generate the anatomical model space. Each additional hypothesis tested results in a multiplication of the number of DCM models to invert by the number of variations on the connection required to test the hypothesis. To limit the number of combinations, the connections between the medial prefrontal cortex (PRL and IL) and other regions (BLA and

DCA1) were assumed to either both be forward connections, or both backward connections. Where there was sufficient, non-conflicting evidence in the literature supporting a given connection between regions, connections were fixed. A summary of the anatomical connections and hypotheses is provided in Figure 5.2.

Fixed connections:

Hippocampal-amygdala connections

The evidence for connections between the rodent BLA and the hippocampus primarily focuses on connections with the ventral hippocampus; however, functional connectivity measures presented in chapter 4 support connectivity between BLA and DCA1. The connections from BLA to DCA1 and from DCA1 to BLA were assumed to be backwards connections based on optogenetic data showing BLA neurons synapse on hippocampal pyramidal neurons and inhibitory interneurons and that DCA1 pyramidal neurons synapse on the principal cells of the BLA and on inhibitory interneurons (Felix-Ortiz et al., 2013, Hübner et al., 2014).

A backwards connection connects BLA to prefrontal cortex

Anterograde tracing and immunocytochemistry has shown that glutamatergic BLA afferents predominantly synapse with pyramidal cells in the prefrontal cortex, but also provide a direct innervation to local inhibitory interneurons (Gabbott et al., 2006). Activation of BLA neurons projecting to the prefrontal cortex evokes action potentials in interneurons but suppresses activity of pyramidal neurons in the prefrontal cortex (Dilgen et al., 2013, Ji et al., 2010). This suggests that connections from the prefrontal cortex to the BLA are likely to be backward connections, however, the Granger causality analysis in Chapter 4 suggested a directional input from the BLA to the PRL which may be more in keeping with a forward connection.

Figure 5.2: Graphical depiction of anatomical models for hypothesis testing

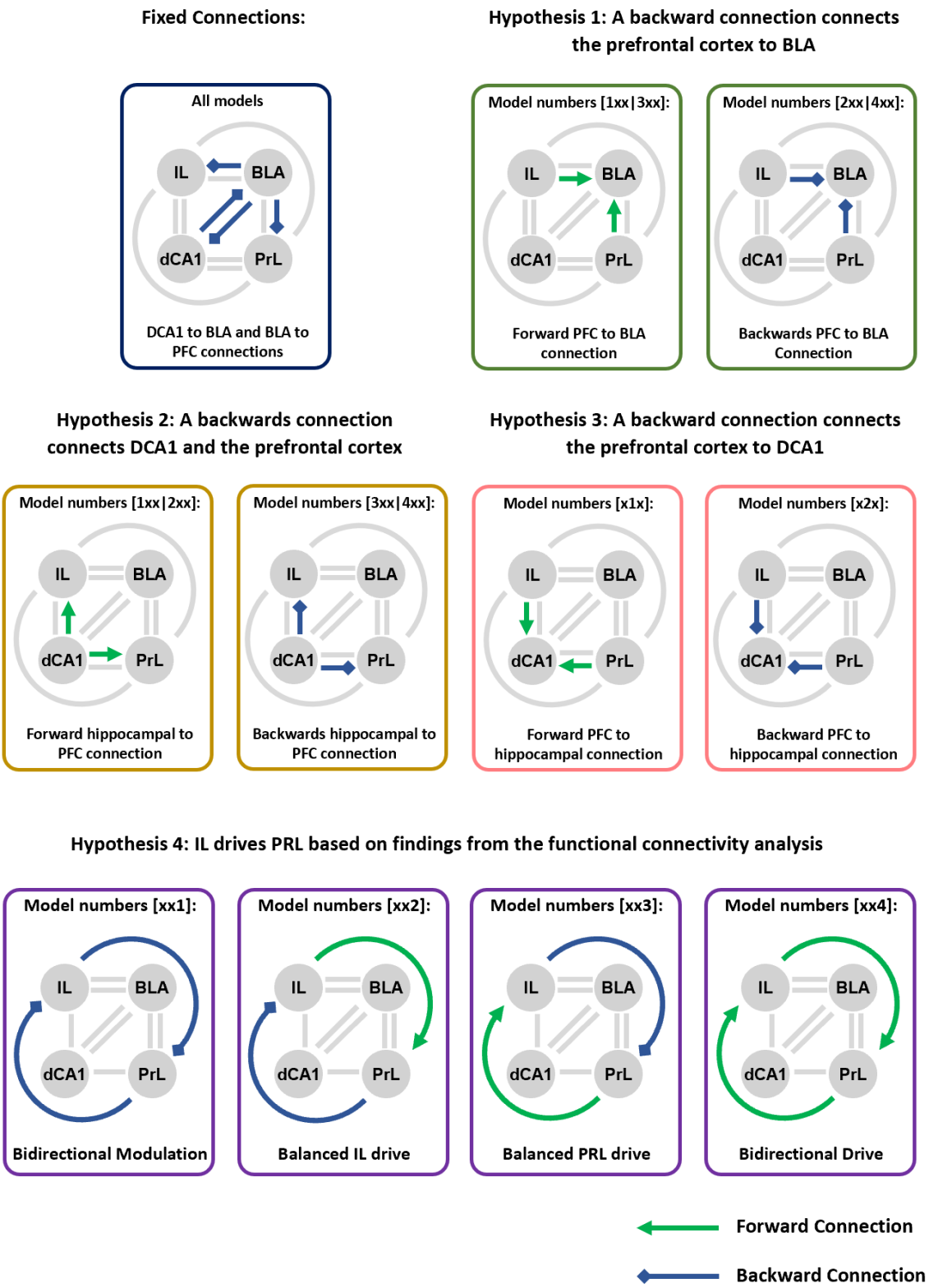

Overview of the anatomical model space tested in the DCM analysis. Grey circles represent neural sources. Green arrows represent forward (glutamatergic) connections between regions, and blue arrows represent backward (glutamatergic) connections between regions. Further details of these connections are shown in Figure 5.1. Grey lines represent connections that are present across models but are outside of a given anatomical hypothesis. A summary of the evidence for each connection is described in Section 5.2.4.

Anatomical Hypotheses

Hypothesis 1: A backward connection connects the prefrontal cortex to BLA

The medial prefrontal cortex sends glutamatergic projections to both principal neurons and interneurons in the BLA, with evidence of reciprocal connections from some of these principal neurons back to the prefrontal cortex providing a feedback mechanism (Hübner et al., 2014). In mice, neural activity in the BLA becomes entrained to prefrontal theta oscillations after successfully learning stimulus discrimination in fear conditioning tasks (Likhtik et al., 2014). Strong directional prefrontal-amygdala coupling occurs between the prefrontal theta and BLA gamma oscillations, with the frequency of the gamma band varying from fast to slow depending on the balance of fear and relaxation (Stujenske et al., 2014). Based on the anatomical data a backwards connection is most likely.

Hypothesis 2: A backwards connection connects DCA1 and the prefrontal cortex

Monosynaptic connection between rat hippocampus CA1 and the infralimbic cortex were first shown by dye tracking of neurons (Swanson, 1981), with projections from the hippocampus to the prefrontal cortex synapsing on both pyramidal and interneuron populations (Tierney et al., 2004). This pattern of connectivity is in keeping with a backwards connection from the hippocampus to the prefrontal cortex, however, previous DCM analysis from the Jones lab on the effects of ketamine supported a forward connection synapsing only on pyramidal cells (Moran et al., 2015).

Hypothesis 3: A backwards connection connects the prefrontal cortex to DCA1

The anatomical pathway from the prefrontal cortex to the hippocampus is polysynaptic and less well defined than the pathway from the hippocampus to the prefrontal cortex. IL and PRL are known to project to the entorhinal cortex (Insausti et al., 1997) which in turn projects to the hippocampus via the perforant pathway (Witter, 2007). An alternative pathway from the prefrontal cortex via the nucleus reuniens of the thalamus has been proposed which projects to both dorsal and ventral CA1 and is suggested to have a role in both memory and executive function (Dolleman-van der Weel et al., 2019). Given the role of the entorhinal cortex and nucleus reuniens as intermediaries in the pathway from prefrontal cortex to hippocampus, this connection is most likely to be modelled by backwards connection, however, in the previous DCM study on ketamine conducted by the lab, the leading model had a forward connection between prefrontal cortex and hippocampus (Moran et al., 2015).

Hypothesis 4: IL drives PRL based on findings from the functional connectivity analysis

IL and PRL show the most striking pattern of HFO emergence following 25I and so particular attention was placed on testing the anatomical connectivity of this region. Optogenetic approaches show that activation of IL pyramidal cells leads to inhibition of PRL output, although whether this is via inhibitory interneurons is unclear (Ji and Neugebauer, 2012). The functional connectivity results reported in Chapter 4 suggests that IL is the most likely source of HFO in the cortico-limbic circuit. Similarly, the reciprocal connectivity seen between cortical regions on the Granger causality analysis suggests that there is likely to be bidirectional connectivity between these regions, with IL having a leading role based on analysis of Granger causality (Chapter 4).

5.2.3. Patterns of modulation

Within a DCM model it is possible to specify which connections and neural populations are fixed, and which can vary from their prior values, however, this is reliant upon a clear hypothesis about where the experimental manipulation is likely to be acting. Serotonergic projections from the dorsal raphe innervate all of the areas studied in this thesis (Vertes, 1991). In the prefrontal cortex 5HT2a receptors are expressed most strongly in layer V deep pyramidal neurons, but are also present in superficial pyramidal neurons, GABAergic interneurons and to a lesser extent in non-pyramidal cells in layers I-III (Weber and Andrade, 2010). Given this ubiquity, there was no clear rationale to restrict modulation to a specific region.

5.2.4. Frequency ranges for DCM models

DCM has a finite number of variables that can vary during model inversion. This can limit the ability of a single model to fit data over broad frequency ranges, especially where drug effects have opposing effects over different frequency bands (Chapter 4). Dividing the frequency spectrum is a trade-off between the accuracy of model fitting over narrower frequency bands, verses reduced complexity and increased interpretability with a single, or small number of models. For this reason, the frequency bands of interest were divided into a low frequency range (2-12Hz), capturing the delta and theta bands, a mid-frequency range (12-48Hz) capturing beta and low gamma, and a high frequency range (52-170Hz) covering high gamma and high frequency oscillations. The frequencies were chosen to avoid filtering line noise at 50Hz. The results of each frequency range are presented individually in the subsequent results section.

5.2.5. Analysis pipeline

For each combination of neural mass model, anatomical model and frequency, a set of DCM models was inverted. Each set of DCM models was composed of separate DCM models for each animal (n=5) at each time point (baseline, early post-drug and late post-drug), and condition (25I and control). This yielded 6 DCM models per individual animal which were taken forward for model comparison and further analysis. Figure 5.3 summarises the structure of the DCM analysis graphically.

To enable fitting of HFO, the SPM12 code required a simple modification. This was due to automatic down sampling of neural data as part of the processing prior to fitting the DCM models. This limited the sampling frequency (f_s) to 250Hz, meaning the Nyquist frequency of

the signal ($f_s/2$) was bought within the frequency range of interest. The code that led to automatic down-sampling (lines 122 to 127 in 'spm_dcm_csd_data.m') was commented out and the sample rate manually set for each frequency range of interest.

Fitting of DCM models was conducted on BlueCrystal Phase 4 at the University of Bristol Advanced Computing Research Centre running MATLAB (Mathworks, Natick,MA) R2018a (9.4.0.813654) 64-bit (glnxa64) for Linux. All other analysis was performed on a windows desktop running MATLAB (Mathworks, Natick,MA) version R2019a 9.6.0.1072779.

Figure 5.3: Structure of DCM analysis

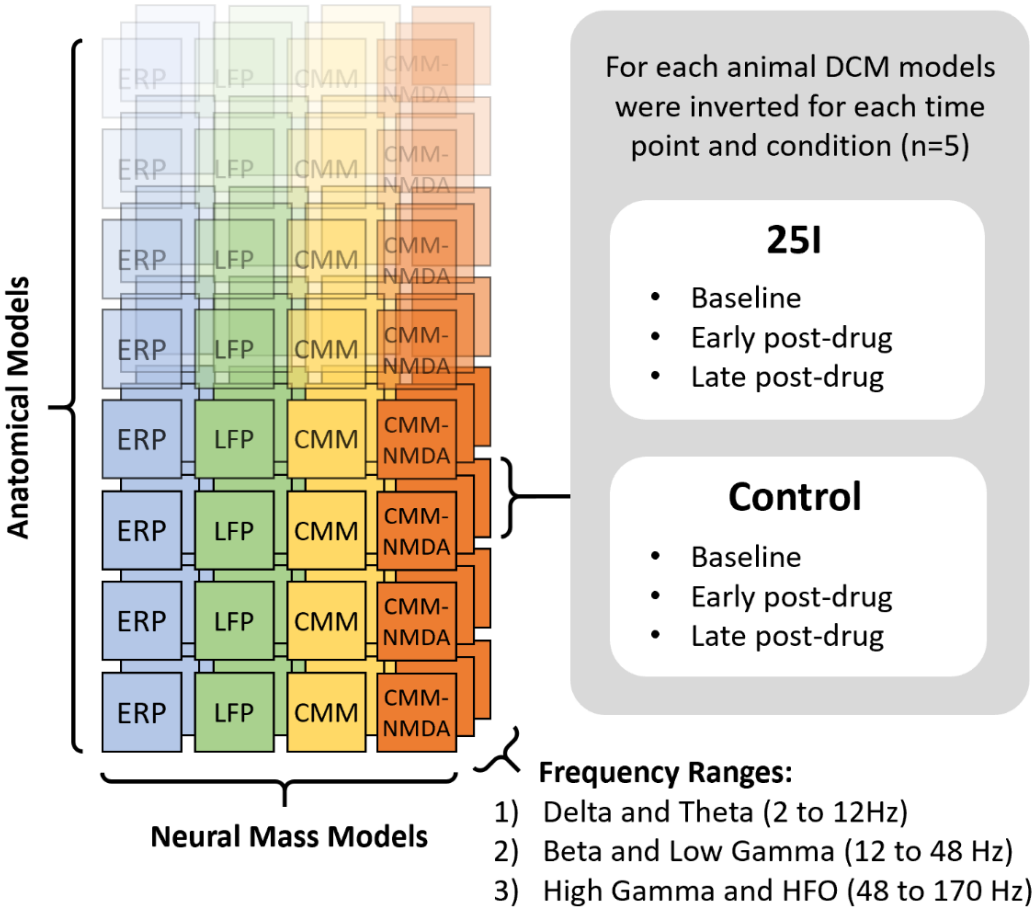

Each combination of anatomical model (see Figure 5.2) and neural mass model (see Table 5.1) was inverted for each of the frequency ranges of interest. For each animal (n=5) a separate DCM was inverted for each time point and experimental condition. Models were subsequently compared by family-wise comparison to test anatomical hypotheses (see Section 5.2.6). Individual models were compared across each frequency range to determine the leading models which were taken forward to determine the effects of 25I on extrinsic connectivity using hierarchical parametric empirical Bayes (PEB; see Section 5.2.8).

5.2.6. Testing anatomical hypotheses

A variety of approaches for model comparison have been developed alongside DCM to enable family-wise comparison between models and comparison of individual models. A summary of an approach to selecting a model comparison is provided by Stephen (Stephan et al., 2010). Fixed effects comparisons are conducted by comparing the sum of the log model evidence (approximated by the free energy) between models (Stephan et al., 2009). Fixed effects comparisons are appropriate when a single model is believed to underlie the observed phenomena in all animals. Conversely a random effects model allows for each subject to have a different distribution of model likelihoods and uses a Bayesian approach based on Gibbs sampling to determine the likelihoods of each model (Penny et al., 2010). Given the data presented in Chapter 4 there are clear differences in functional connectivity at baseline between animals (Illustrated by the median and IQR for both coherence and Granger causality in Figures 4.15 to 4.20). Differences in connectivity between animals supports the use of a random effects model, however, within models fitted to data from a single animal the neural mass model and anatomical model should remain fixed over each frequency range of interest.

Each animal in this study had separate DCM models inverted for the baseline, early post-drug and late post-drug periods in both 25I and control conditions giving a total of 6 DCMs per anatomical model. For each anatomical model the log model evidence was approximated for each animal as the sum of the free energy across the set of 6 DCM models fitted for that animal. This resulted in a single log model evidence per animal for each of the anatomical models. The estimated log model evidence was in turn used for both random-effects family-wise comparison using the command ‘spm_compare_families’ and individual model random-effects comparison using the command ‘spm_BMS’. Random effects comparison is more robust against outlying data that can have a disproportionate effect on fixed effects comparisons (Stephan et al., 2009).

Family-wise comparison was used to identify the type of neural mass model that was the best fit for the data. The family of neural mass models that provided the best fit were taken forward for subsequent family-wise and individual model comparison. Family-wise comparisons are expressed in terms of exceedance probability which is the probability that one model is more likely than any other model in the comparison to explain the data (Stephan et al., 2009).

5.2.7. Determination of leading models

Where individual model comparison yielded a single best model, this model was taken forward as the leading model for exploration of individual parameters. Where individual model comparison resulted in a tie between models, the family-wise comparison was considered alongside the individual model comparison to determine the leading model. Model fits were tested by visual comparison of the power and coherence spectra from the experimental data with the data generated from the fitted DCM models. Cross spectral densities were generated using the command 'spm_csd_mtf' on each model, converted to power (dB) and z scored for plotting and comparison with the experimental data. Coherence was generated from the cross spectral densities using the command 'spm_csd2coh'.

5.2.8. Analysis of extrinsic connectivity in leading models

To describe the effects of 25I on the extrinsic connectivity (A matrix) of the leading DCM models a hierarchical parametric empirical Bayes (PEB) approach was used. A detailed summary, and example implementation, of a hierarchical PEB approach is provided by Zeidman (Zeidman et al., 2019). In brief PEB uses a Bayesian generalised linear model approach to describe the variation in the DCM parameters of interest based upon the estimates and covariance of those parameters from individual DCM (or PEB) models. A second (or higher) level PEB can be specified over the parameters at the previous level, enabling hierarchical models. In this chapter I specified a first level "within condition" PEB and a second level "between condition" PEB for each animal, and a third level "between subject" PEB to combine data across the 5 animals.

The first level PEB was a "within condition" comparison that encoded the extrinsic connectivity at baseline, the change from baseline to the early post-drug period, and the change from baseline to the late post-drug period for each animal and experimental condition. A second level "between conditions" PEB combined the first level PEB models from each animal by encoding the parameters of the first level PEB under the control condition, and the effect of 25I on these parameters for each subject. The second level PEB models were entered into a final third level "between subjects" PEB that combined the individual second level PEB models from each animal to produce an overall model for the effect of 25I on extrinsic connectivity.

Bayesian model reduction (BMR) was applied to the "between subjects" PEB with the command 'spm_dcm_peb_bmc'. The BMR approach implemented with this command performs an efficient comparison of the 'full' PEB model with nested reduced models to iteratively discard parameters that do not contribute to the model evidence and calculates a

Bayesian Model Average (BMA) across the reduced models (Zeidman et al., 2019, Rosa et al., 2012, Friston and Penny, 2011). In the results from the PEB analyses presented below all parameters that varied from their priors with greater than 75% likelihood following BMR are reported alongside likelihoods.

To calculate the mean baseline across the control and 25I condition the second level PEB was altered to encode group means, and difference between means for each timepoint, before being entered into the third level "between subjects" PEB and application of BMR. This approach ensured that the mean baseline condition was calculated based on both the parameter estimates and the variance and provided likelihoods for baseline connectivity.

5.3. Results

5.3.1. LFP models more effective at low frequencies, CMM_NMDA models at high frequencies

Comparison of neural mass models demonstrated that LFP based models worked best for the low and middle frequency ranges whilst CMM_NMDA models worked best for the high frequency range (Figure 5.4). The exceedance probability for the LFP models in the low frequency range was 0.62 vs 0.32 for the next highest model family (ERP). The exceedance probability for LFP models in the middle frequency range was 0.45 vs. 0.33 for the next highest model family (CMM_NMDA). The exceedance probability for CMM_NMDA models in the high frequency range was 0.66 vs 0.11 for each of the other model families.

CMM_NMDA models include parameters encoding the action of glutamate at both AMPA and NMDA receptors and encompass non-linear interactions between conductance and depolarization, with scope to describe a broader range of neural processes (Moran et al., 2013). This broader range of CMM_NMDA models may explain why this model was better suited to describing the high frequency DCM models.

5.3.2. The anatomical structure of effective connectivity models varies over the frequency spectra

The results of the anatomical hypotheses varied by frequency range, although there was consistent evidence for a backwards connection between the prefrontal cortex and DCA1 (Figure 5.4). The variation in the best anatomical model by frequency range was unexpected, however likely represents the varied neural mechanisms resulting in LFP signals in different frequency ranges. It is likely that the underlying brain circuits may contain both forward and

backwards connections, with corresponding connection strengths, however it was beyond the scope of the present thesis to test this further.

The stated anatomical hypotheses aligned with the leading anatomical connections in the low frequency range, with the exception of the intracortical connection. In the high frequency range, there was a leaning towards forwards connections potentially supporting a role for feedforward excitation in the generation of HFO.

The coherence and Granger causality analysis in Chapter 4 highlighted the variation between connection strength and directionality over the frequency spectra with the results for the family-wise comparison potentially supporting a hypothesis that neural circuits form distinct patterns of circuitry (effective connectivity) when described over different parts of the frequency spectrum.

Figure 5.4: Family-wise comparison of the exceedance probability for neural mass and anatomical models for each frequency range

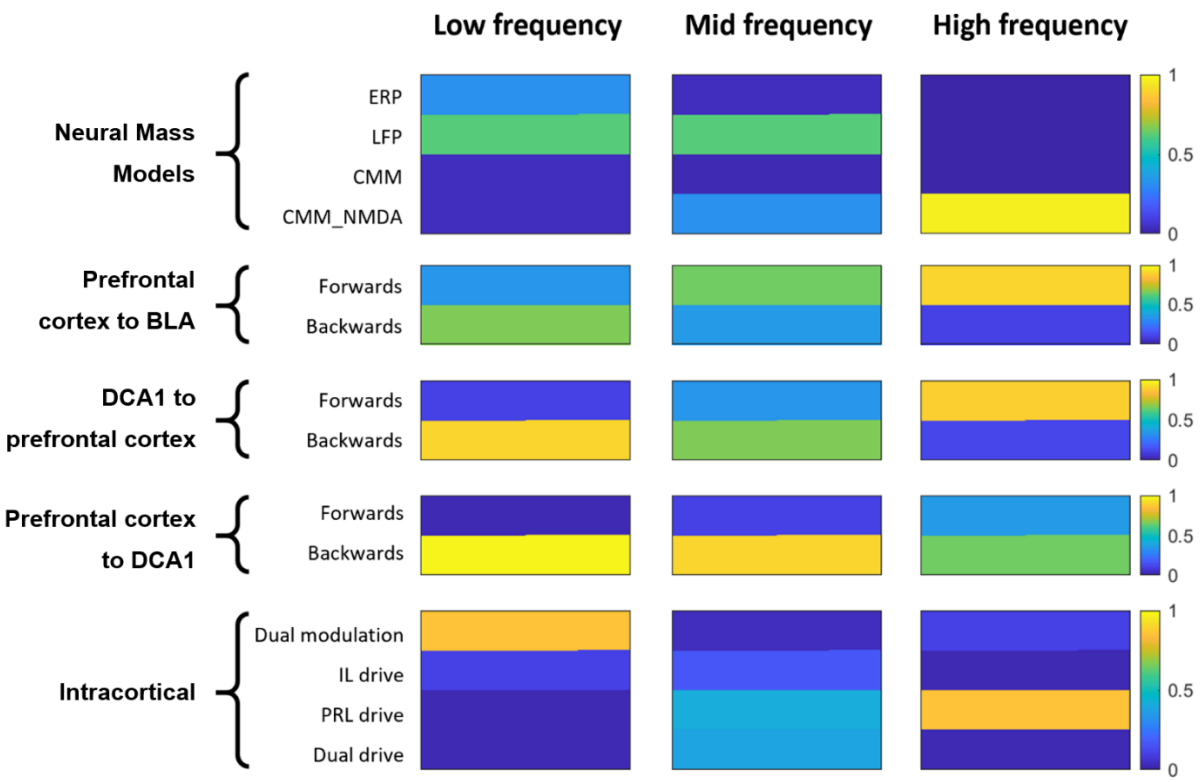

Family-wise comparison was used to determine the leading neural mass model (NMM) for each frequency range (see description in Section 5.2.6). Subsequent family-wise comparisons for each frequency range were based only on models using the leading NMM. Exceedance probability is expressed from 0 to 1 as illustrated by the colour bar accompanying each plot with a sum of 1 across each comparison. An exceedance probability of 1 means that the model family is 100% likely to explain the data better than any other family in the comparison, and a value of 0 meaning the model family is 0% likely to explain the data better than any other family in the comparison. Low and mid frequency models favoured LFP models, whilst the high frequency model favoured the CMM_NMDA model. Anatomical hypotheses varied across the frequency ranges with only the comparison of the connection from the prefrontal cortex to DCA1 backwards across all three frequency ranges. Results are discussed in more detail in the text.

5.3.3. Low frequency DCM model

Model Selection

The leading models from individual model comparison in the 2-12Hz frequency range was LFP model 311. Model 311 was the leading model for 2 out of 5 animals and lay at the intersection of the leading model families from the family-wise comparison, with the exception of having a forward connection from prefrontal cortex to BLA (exceedance probability = 0.35), rather than a backwards connection from prefrontal cortex to BLA as per family wise comparison (exceedance probability = 0.65). The leading model performed well in fitting the data with comparison of the experimental data and model-generated data spectral power shown in Figure 5.5. The fit between experimental and model generated coherence was also assessed visually (not shown) with the generated data demonstrating reasonable correspondence with the experimental data, although not as accurately as for spectral power.

Figure 5.5: Leading low frequency (2-12Hz) model fits by condition and timepoint

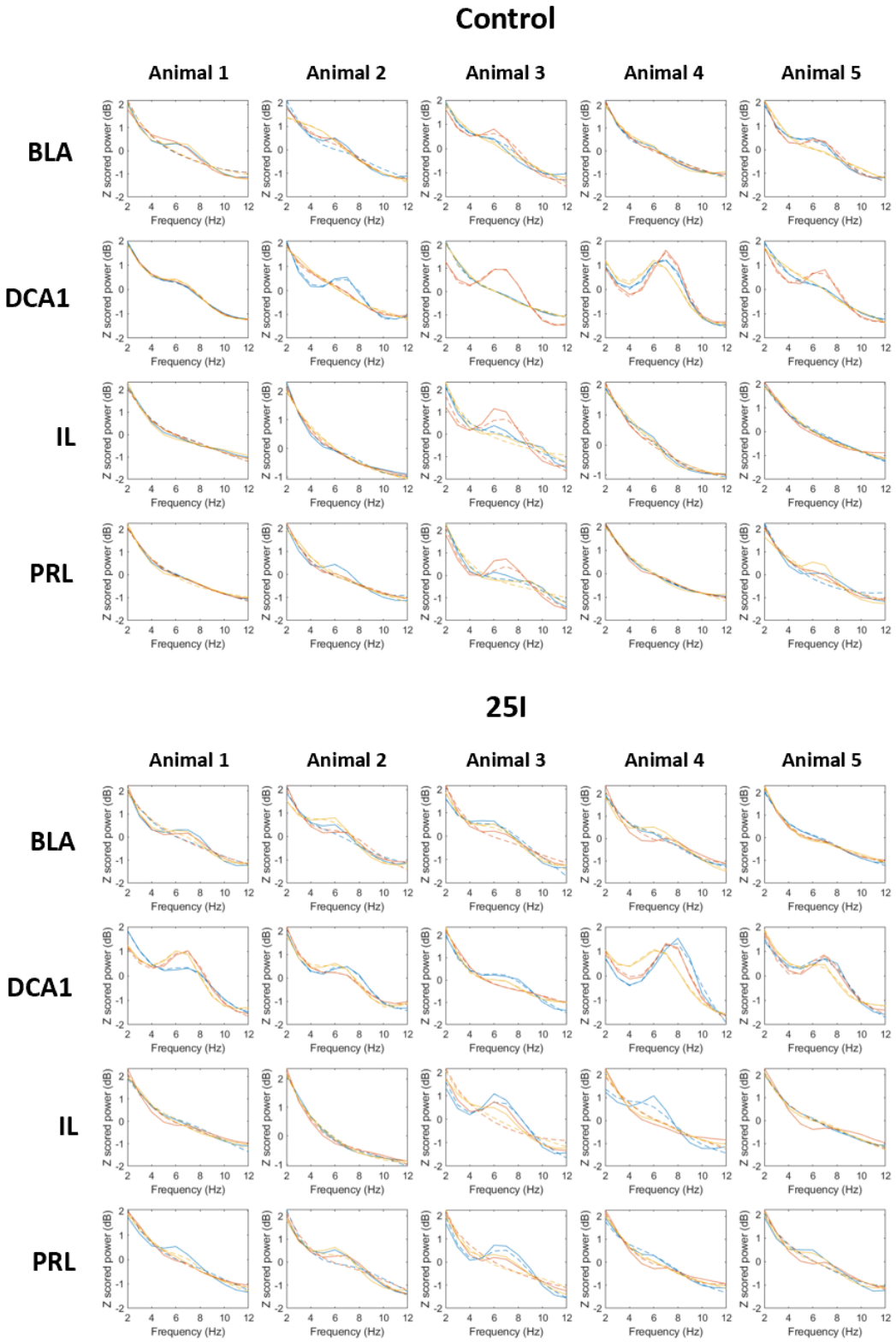

Model fits for leading low frequency DCM model showing Z-scored spectral power against frequency. Experimental data is shown in the solid lines, with generated data from the model in dashed lines. Model fits for the control condition are shown in the top panel and for the 25I condition in the bottom. Each plot shows the baseline, early post-drug and late post-drug effects for control. Generated data from the model captures most of the spectral features seen in the experimental data.

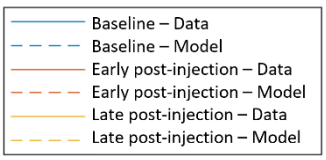

25I increases low frequency cortico-amygdala connectivity in both directions and disrupts top down cortico-hippocampal communication

The full effects of 25I on extrinsic connectivity between regions at low frequencies is presented in Figure 5.6, alongside the group mean connectivity at baseline and a diagram of the leading model.

In the early post-drug period 25I resulted in an increase in the strength of the connection from the BLA to the PRL that persisted into the late post-drug period with a corresponding increase from PRL back to BLA. These findings support persistent increased coupling between BLA and PRL in the delta and theta range following 25I. The finding is consistent with the functional connectivity analysis in Chapter 4, where PRL and BLA showed significant increases in delta and theta coherence in the early post-drug period that persisted, but were no longer significant, in the late post-drug period. Granger causality suggested that this change in connectivity was directed from the PRL to the BLA at both early and late timepoints.

The decreases in connectivity from PRL to DCA1 in the early post-drug period and IL to DCA1 in the late post-drug period support disruption of cortico-hippocampal connectivity; again, this finding is corroborated by the functional connectivity analyses in chapter 4 that demonstrate reduced connectivity from IL to DCA1 at both timepoints.

Figure 5.6: Effects of 25I on extrinsic connectivity for the leading low frequency (2-12Hz) model

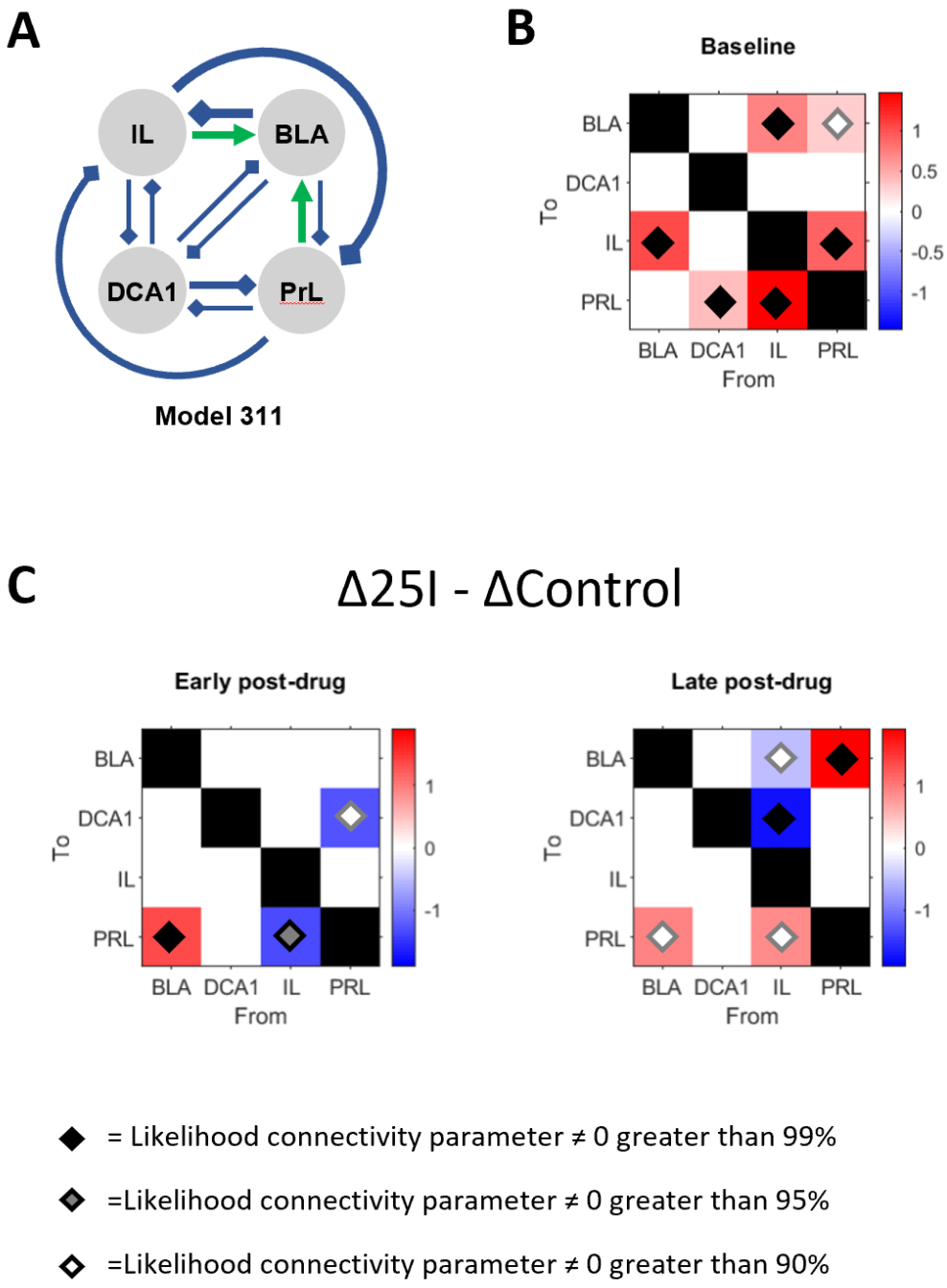

A: Diagram of the leading model for the low frequency range at baseline, calculated as the group mean across conditions and animals using PEB. Green lines represent forwards extrinsic connections, and blue lines represent backwards extrinsic connections. The thickness of lines has been scaled to represent the relative strength of each connection with thin lines representing a reduced connection strength and thick lines representing an increased connection strength. **B:** Matrix plot of the baseline connection strength calculated as the group mean across conditions and animals using PEB. Likelihood estimates for each parameter according to the graphical legend. **C:** Matrix plot of the difference in extrinsic connectivity (described by the gain parameter on each connection) from baseline to the early and late post-drug period. Values are expressed as the difference between the change seen with 25I over control, with red representing an increased connection strength, and blue a decrease in connection strength. Likelihood estimates for each parameter are marked according to the graphical legend.

5.3.4. Middle frequency DCM model

Model selection

The individual model comparison in the 12-48Hz range did not yield a leading model. Models numbers 113, 203, 312, 314 and 414 were equally likely – each providing the most likely model for a single animal. Review of the family-wise comparison showed a backwards connection from hippocampus to the prefrontal cortex and from the prefrontal cortex to the hippocampus was most likely, alongside a forward connection from the prefrontal cortex to the BLA. Balanced PRL drive (xx3) and bidirectional drive (xx4) were equally likely for the cortical connection. Only model 314 was a leading model in the individual model comparison and lay at the intersection of the family comparison so was taken forward as the leading model in subsequent analysis.

The leading model performed well in fitting the data with comparison of the experimental data and model generated data spectral power shown in Figure 5.7. The fit between experimental and model-generated coherence was also assessed visually (not shown) with the generated data demonstrating reasonable correspondence with the experimental data, although not as accurately as for spectral power.

Figure 5.7: Leading middle frequency (12-48Hz) model fits by condition and timepoint

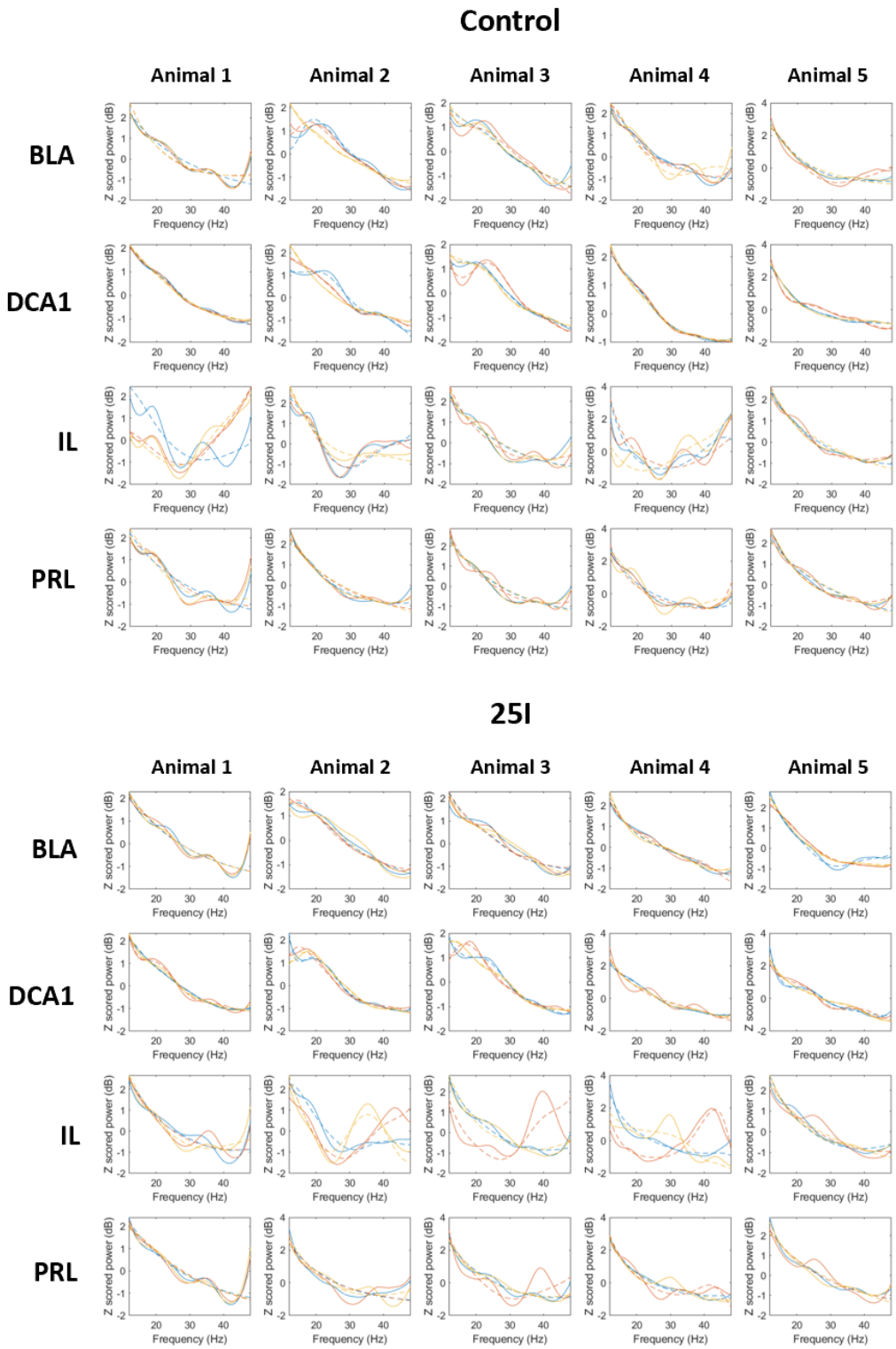

Model fits for leading middle frequency DCM model showing Z-scored spectral power against frequency. Experimental data is shown in the solid lines, with generated data from the model in dashed lines. Model fits for the control condition are shown in the top panel and for the 25I condition in the bottom. Each plot shows the baseline, early post-drug and late post-drug effects for control. Generated data from the model captures most of the spectral features seen in the experimental data.

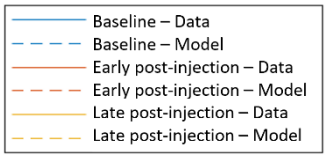

In middle frequencies 25I results in top-down cortical control of the amygdala, with further disruption to cortico-limbic hippocampal coupling

The full effects of 25I on extrinsic connectivity between regions in the middle frequencies is presented in Figure 5.8, alongside the group mean connectivity at baseline and a diagram of the leading model.

In the late post-drug period there was a large decrease in the strength of bottom-up connections from the BLA to the PRL, and a corresponding increase in the top-down connection from IL to BLA. A corresponding increase was seen in beta coherence between IL and BLA in the functional connectivity analysis at both time points, and a (non-significant) decrease in coherence between BLA and PRL. This suggests a shift in the balance of cortico-amygdala connectivity towards top-down control in the beta and low gamma frequencies. The changes in connectivity from BLA to PRL are in the opposite direction to the changes observed at low frequencies, despite consistent model architecture across connections between BLA and prefrontal cortex.

In the middle frequencies there was significant disruption of hippocampal coupling between both the BLA and the prefrontal cortex. At both time points the strength of the connection from BLA to DCA1 was reduced, with reductions in connection strength from IL to DCA1 seen in the early post-drug period, and from PRL to DCA1 in the late post-drug period. The connection from IL to DCA1 shows corresponding reductions in coherence and reduced Granger causality in beta and low gamma frequencies at both time points in the functional connectivity analysis (Chapter 4), although this is less consistent from PRL to DCA1.

Figure 5.8: Effects of 25I on extrinsic connectivity for the leading middle frequency (12-48Hz) model

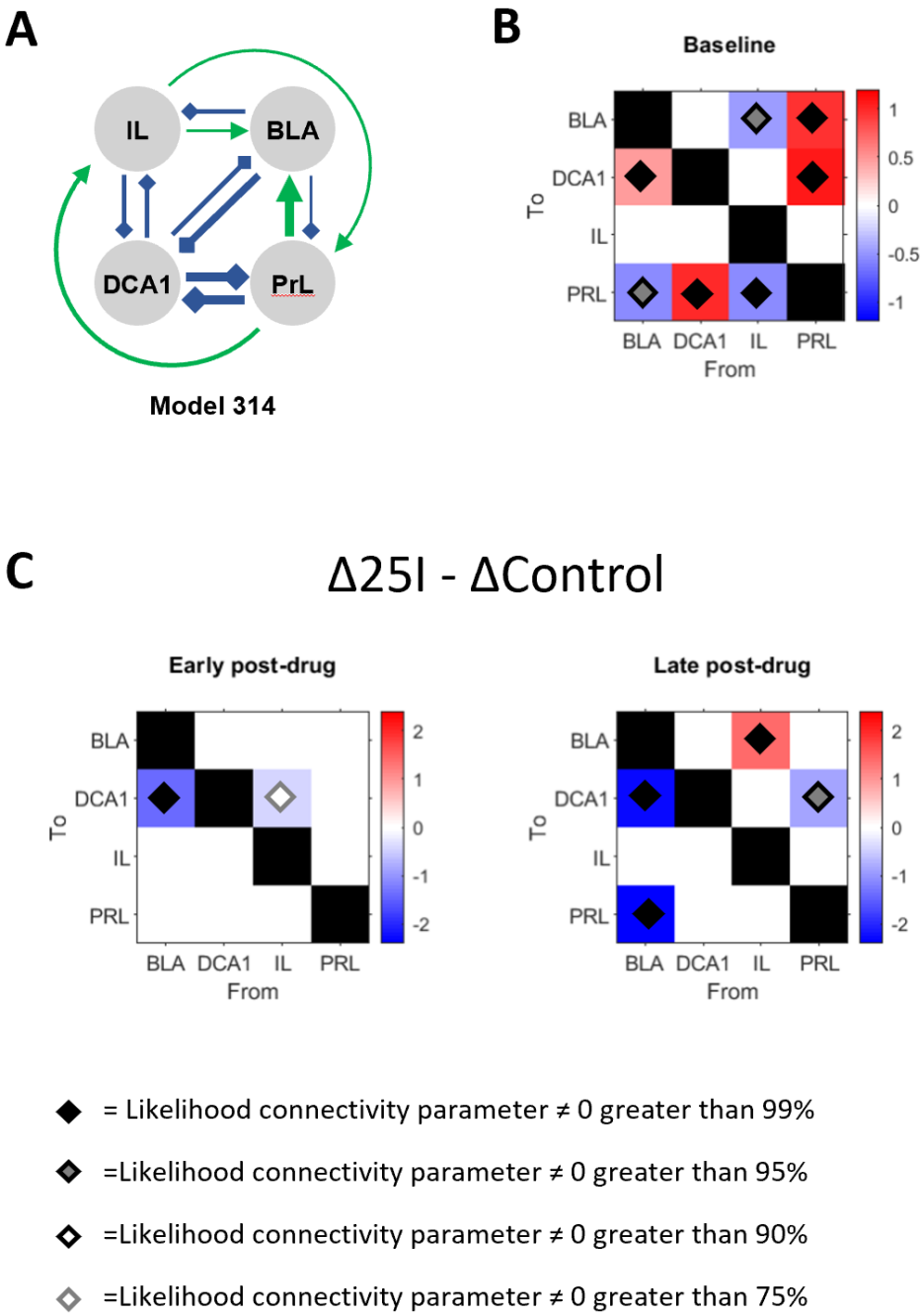

A: Diagram of the leading model for the middle frequency range at baseline, calculated as the group mean across conditions and animals using PEB. Green lines represent forwards extrinsic connections and blue lines represent backwards extrinsic connections. The thickness of lines has been scaled to represent the relative strength of each connection with thin lines representing a reduced connection strength and thick lines representing an increased connection strength. **B:** Matrix plot of the baseline connection strength calculated as the group mean across conditions and animals using PEB. Likelihood estimates for each parameter according to the graphical legend. **C:** Matrix plot of the difference in extrinsic connectivity (described by the gain parameter on each connection) from baseline to the early and late post-drug period. Values are expressed as the difference between the change seen with 25I over control, with red representing an increased connection strength, and blue a decrease in connection strength. Likelihood estimates for each parameter are marked according to the graphical legend.

5.3.5. High frequency DCM model

The individual model comparison in the 52-170Hz range did not yield a leading model. Models numbers 101,103,113, 212 and 313 were equally likely – each providing the most likely model for a single animal. Review of the family-wise comparison showed that a forward connection was most likely from the hippocampus to the prefrontal cortex (1xx|2xx), and from the prefrontal cortex to the amygdala (1xx|3xx). A backwards connection was most likely from the prefrontal cortex to the hippocampus (x1x), and balanced PRL drive (xx3) was the most likely cortical model. The model at the intersection of the family-wise comparison was model 113 which was also a leading model in the individual model comparison, so was taken forward as the leading model in subsequent analysis.

The leading model performed well in fitting the data (including HFO) with comparison of the experimental data and model-generated data spectral power shown in Figure 5.9. The fit between experimental and model-generated coherence was also assessed visually (not shown) with the generated data demonstrating reasonable correspondence with the experimental data, although not as accurately as for spectral power.

Figure 5.9: Leading high frequency (52-170Hz) model fits by condition and timepoint

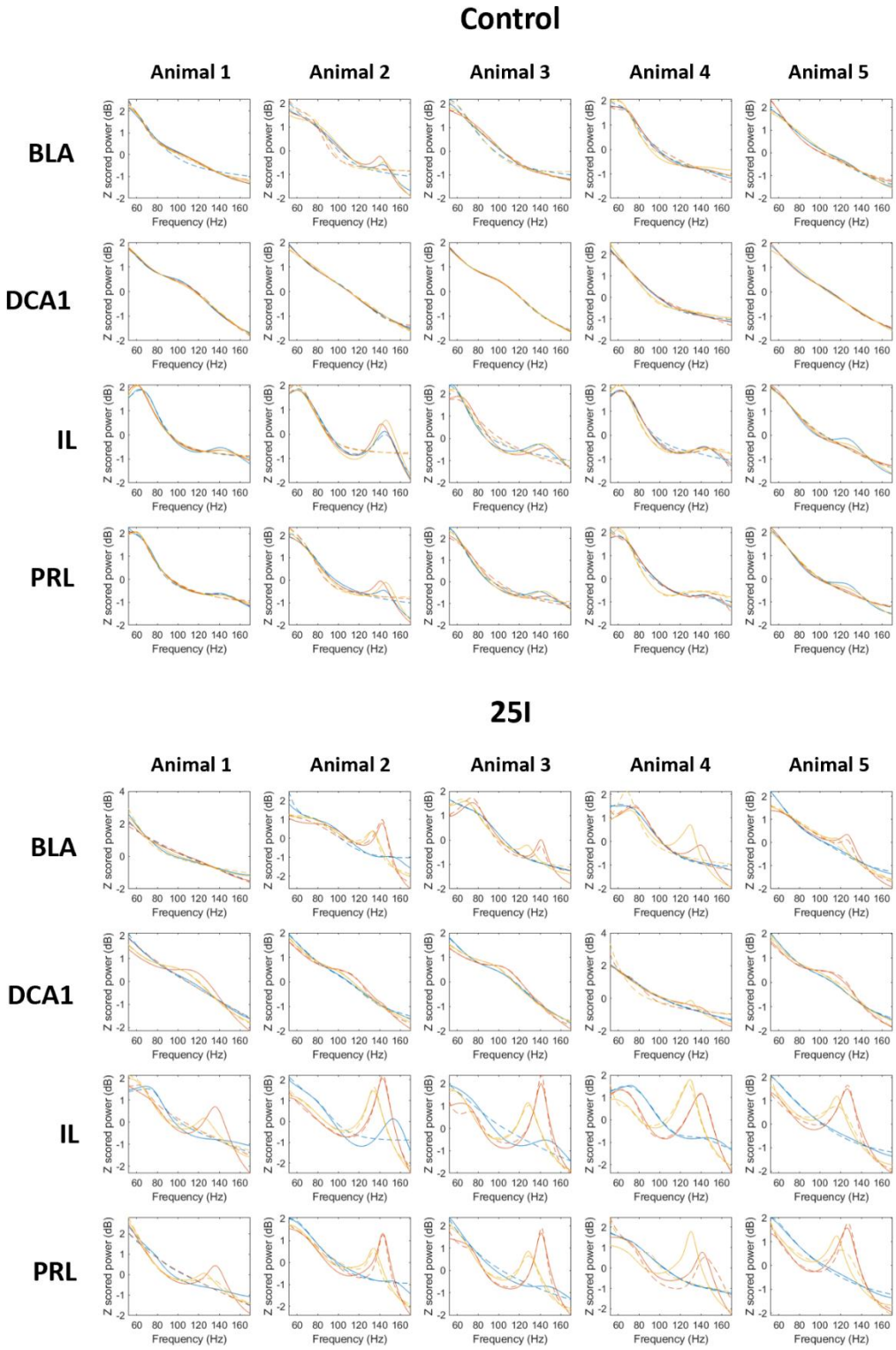

Model fits for leading high frequency DCM model showing Z-scored spectral power against frequency. Experimental data is shown in the solid lines, with generated data from the model in dashed lines. Model fits for the control condition are shown in the top panel and for the 25I condition in the bottom. Each plot shows the baseline, early post-drug and late post-drug effects for control. Generated data from the model captures most of the spectral features seen in the experimental data including the emergence of HFO peaks in IL, PRL and BLA under the 25I condition.

Early post-drug IL cortex suppresses PRL and demonstrates top-down modulation of the DCA1; BLA receives increased connections from DCA1 (early) and PRL (late)

CMM_NMDA models include connectivity parameter estimates for AMPA receptor-mediated connectivity and NMDA receptor-mediated connectivity. The full effects of 25I on extrinsic AMPA connectivity between regions in the high frequencies is presented in Figure 5.10, alongside the group mean connectivity at baseline and a diagram of the leading model. There was no variation from zero for the NMDA connectivity parameters at baseline and no effects of 25I or control over time (data not shown).

In the early post-drug period in the high frequency range there is an increase in connectivity from the IL to PRL, with a corresponding decrease from PRL to IL. This is in keeping with the functional connectivity analysis supporting IL driving PRL activity following 5-HT_{2A} receptor activation. Whilst the connection from IL to PRL is a backwards connection this is in keeping with optogenetic data suggesting that IL can suppress PRL output (Ji and Neugebauer, 2012).

At both time points IL demonstrates increased connectivity to DCA1, with corresponding reductions in connectivity from DCA1 to IL. This finding is consistent with increases in coherence in the high gamma range between IL and DCA1, and consistent with the direction of the Granger causality. DCA1 shows increases in connectivity to PRL in the early post-drug period, accompanied by a decrease in connectivity from PRL.

In the early post-drug period DCA1 shows increased connection strength to the BLA, whilst in the late post-drug period PRL shows increased connection to BLA. This increase in connectivity with the BLA is supported by the functional connectivity analysis (Chapter 4) where BLA primarily demonstrated increased coupling with both DCA1 and prefrontal cortex in HFO and gamma bands.

Figure 5.10: Effects of 25I on extrinsic AMPA mediated connectivity for the leading high frequency (52-170Hz) model

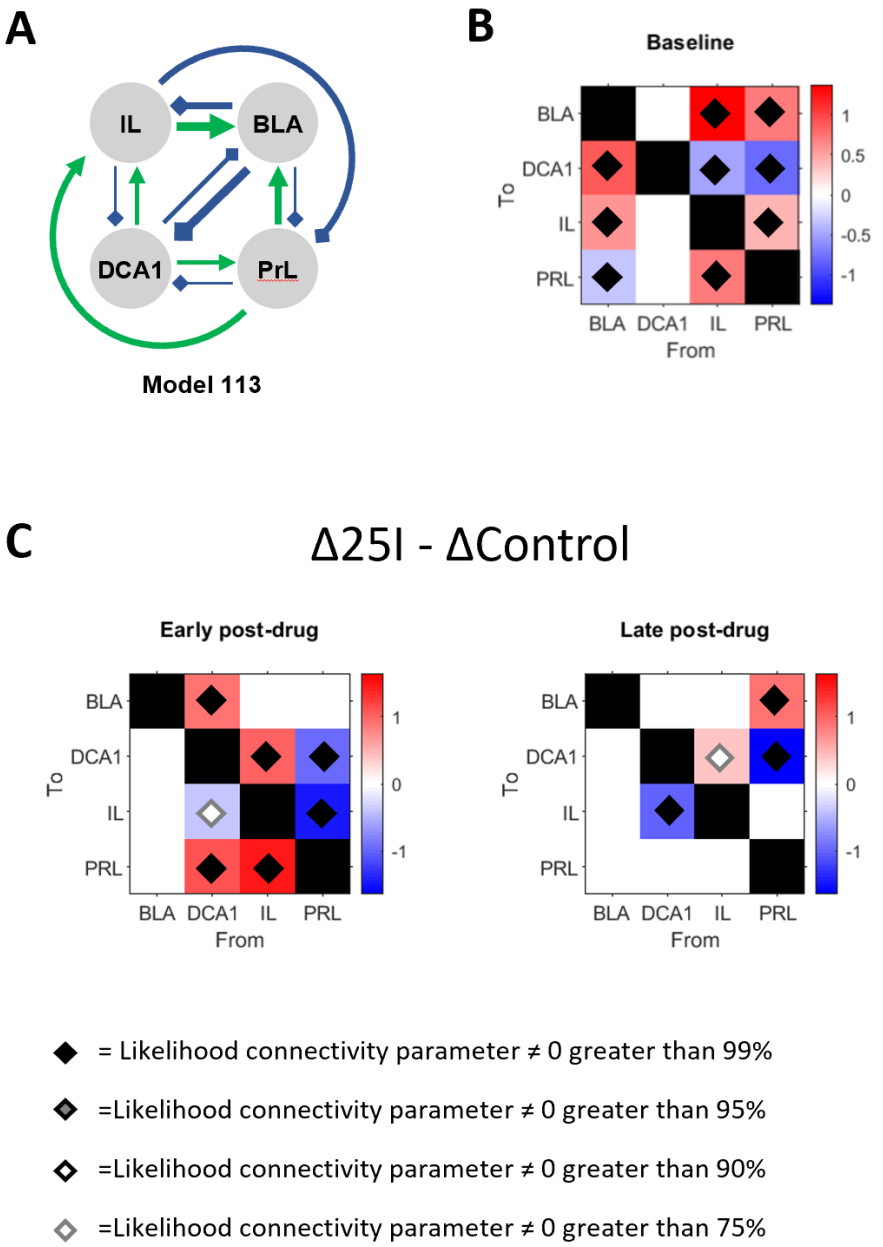

A: Diagram of the leading model for the high frequency range at baseline, calculated as the group mean across conditions and animals using PEB. CMM_NMDA models include parameters for AMPA and NMDA receptor-mediated connectivity. Only AMPA connectivity is shown in this figure as NMDA connectivity did not demonstrate any non-zero effects. Green lines represent forwards extrinsic connections and blue lines represent backwards extrinsic connections. The thickness of lines has been scaled to represent the relative strength of each connection with thin lines representing a reduced connection strength and thick lines representing an increased connection strength. **B:** Matrix plot of the baseline connection strength calculated as the group mean across conditions and animals using PEB. Likelihood estimates for each parameter according to the graphical legend. **C:** Matrix plot of the difference in extrinsic connectivity (described by the gain parameter on each connection) from baseline to the early and late post-drug period. Values are expressed as the difference between the change seen with 25I over control, with red representing an increased connection strength and blue a decrease in connection strength. Likelihood estimates for each parameter are marked according to the graphical legend.

5.4. Discussion

The effective connectivity analysis presented in the present chapter extends the findings of the functional connectivity analysis in Chapter 4 with the approaches showing convergence upon increased top-down regulation of the amygdala by the prefrontal cortex, and a suppression of top-down drive from the prefrontal cortex to the hippocampus.

5.4.1. Implications for future research

The analyses presented in this chapter show proof of principle in the use of DCM to effectively fit high gamma and HFO spectral features using CMM_NMDA models. Whilst CMM_NMDA models were effective at high frequencies they performed poorly in the low frequency range, where LFP models were most effective. These findings support the use of LFP models to model delta and theta frequencies in future DCM studies of the cortico-limbic system, and the use of CMM_NMDA models to model high gamma and HFO frequencies.

5.4.2. The effective architecture of neural circuits varies with frequency

Testing of anatomical models showed variation in the leading models by frequency except for the connection from the prefrontal regions to DCA1, where a backwards connection was most likely across all three frequency ranges of interest. The only routes from the prefrontal cortex to the hippocampus are polysynaptic with the most likely pathways being via the entorhinal cortex (Witter, 2007) and nucleus reuniens (Dolleman-van der Weel et al., 2019), whilst all other inter-regional connections have prominent monosynaptic connections.

Except for the polysynaptic connection from prefrontal cortex to DCA1, the high frequency models showed a preference for forwards (driving) connections between regions, whilst the low frequency models showed a preference for backwards (modulatory) connections, giving a potential insight into the functional role and/or mechanism of neuronal synchronisation in these frequency ranges.

The preference for varied anatomical models across the frequency ranges was not anticipated and highlights the complexity of neural circuits. When combined with the variation in functional connectivity across the frequency spectra (presented in Chapter 4) these findings support variation in the effective inter-regional organisation of neuronal processes across the frequency spectra despite shared anatomical architecture. These findings highlight a potential role for the use of effective connectivity approaches and model comparison for the anatomical dissection of neuronal circuits in the spectral domain.

5.4.3. 5-HT_{2A} agonism increases top-down control of amygdala activity by prefrontal cortex

25I resulted in increased coupling between BLA and PRL in the low frequency range; with the connection strength from BLA to PRL increasing in the early post-drug period, and bidirectional increases in connection strength in the late post-drug period. In the middle frequencies 25I caused an increase in the top-down connection from IL to BLA in the late post-drug period, with a decrease in the connection strength from PRL to BLA. In the high frequencies 25I caused an increase in the top-down connection from PRL to BLA in the late post-drug period. Reduced coupling between the prefrontal cortex and amygdala is consistently found in anxiety disorders (Mochcovitch et al., 2014), and reduced top-down control from prefrontal cortex to amygdala has recently been demonstrated in patients with generalised anxiety disorder relative to healthy controls using Granger causality analysis on resting state fMRI data (Dong et al., 2019). Reduced coupling between the prefrontal cortex and amygdala is also seen in depression (Siegle et al., 2007), and is associated with previous suicide attempts indicative of severe illness (Wang et al., 2020). Increased coupling between the prefrontal cortex and amygdala on fMRI is predictive of attenuation of negative affect in cognitive reappraisal tasks (Banks et al., 2007), suggesting that increasing coupling may be beneficial for the reversal of the cognitive bias in depression. Given these findings, the increase in coupling between the amygdala and prefrontal cortex seen with 25I may be contributory to the therapeutic effects of 5-HT_{2A} agonists in recent clinical trials for anxiety and depression (Andersen et al., 2020).

5.4.4. 5-HT_{2A} agonists disrupt the hierarchical organisation of the cortico-hippocampal circuit

In the low and middle frequency range, 25I reduced top-down connectivity from the prefrontal cortex to the hippocampus. In the high frequency range there was an increase in connectivity from IL to DCA1, likely explained by the increase in HFO coherence described in Chapter 4. In contrast PRL shows a consistent decrease in top-down connectivity to DCA1 with a corresponding increase in bottom-up connectivity from DCA1 to PRL. Taken together these results show that 25I shifts the balance of cortico-hippocampal coupling from top-down towards bottom-up. The disruption of top-down control has been proposed to be a key feature of psychotic disorders (Adams et al., 2013), and may be contributory to the psychotomimetic effects seen with 5-HT_{2A} agonists.

Suppression of top-down cortico-hippocampal connectivity, accompanied by increased bottom-up hippocampal to cortical connectivity, has previously been described following ketamine administration (Moran et al., 2015). The commonality between the effects of

ketamine and 25I on cortico-hippocampal drive provides further evidence for shared pharmacological properties between ketamine and 5-HT_{2A} agonists, in addition to the shared effects on HFO (Chapter 4).

Reductions in top-down control have also been demonstrated in a study of human MEG data from an auditory oddball task under LSD and control conditions (Timmermann et al., 2018). DCM analysis demonstrated that LSD had modulatory effects by reducing the strength of top-down connections, alongside a bottom-up component through modulation of intrinsic connectivity in the primary auditory cortex (Timmermann et al., 2018). This suggests 5-HT_{2A} agonists may exert their effects through broad disruption of hierarchical cortical processes.

5.4.5. Comparison with existing literature yields mechanistic insights

DCM has previously been applied to study 5-HT_{2A} agonists in human fMRI and MEG studies (Muthukumaraswamy et al., 2013, Timmermann et al., 2018, Preller et al., 2019). In a MEG study using psilocybin in healthy volunteers, DCM was used to test the effects of psilocybin on intrinsic neuronal activity within a 4 population model of the posterior cingulate cortex and found that psilocybin increased activity of the deep pyramidal neurons (Muthukumaraswamy et al., 2013). Deep pyramidal neurons have the highest density of expression of 5-HT_{2A} receptors in rat prefrontal cortex supporting this neural population as an important target (Weber and Andrade, 2010). Application of DOI to a bath containing prefrontal cortex slices induces prolonged excitatory post-synaptic currents in response to electrical stimulation in deep pyramidal neurons and increases the likelihood of recurrent and spontaneous self-oscillatory behaviour (Lambe and Aghajanian, 2007, Lambe and Aghajanian, 2006). These effects are dependent on the activity of NR2B-NMDA receptors and are believed to be mediated by glutamate spillover which can result in activation of local neurons outside of the direct synapse (Lambe and Aghajanian, 2006).

The functional connectivity analysis in Chapter 4 supported IL as the most likely source of HFO in the cortico-limbic circuit. In the leading high frequency DCM model, backwards connections, originating from deep pyramidal neurons, show increased gain following 25I from IL to PRL and DCA1, in keeping with IL driving neural activity in the HFO range. These findings support a mechanistic role for activation of 5-HT_{2A} receptors on deep pyramidal neurons in IL in the generation of HFO that may be mediated by glutamate overspill and/or recurrent and self-oscillatory behaviour of deep pyramidal neurons.

Evidence for crosstalk between 5-HT_{2A} and glutamate signalling is reviewed in detail by López-Giménez (López-Giménez and González-Maeso, 2018) with evidence suggesting a

heteromeric complex between the 5-HT_{2A} receptor and metabotropic glutamate receptor 2 is required for behavioural and neurophysiological effects of 5-HT_{2A} agonists (Moreno et al., 2011). Convergence between serotonergic and glutamatergic signalling pathways may provide a common pathway in the generation of HFO by ketamine and 5-HT_{2A} agonists.

5.4.6. Limitations

As described in section 5.2.2 it was necessary to place certain limitations on the anatomical model space considered in this chapter due to the computational resources required to invert large numbers of DCM models. Whilst these limitations were determined by review of the functional connectivity data and the existing literature, the anatomy of the neural circuits is more complex. In the present analysis the prefrontal regions were assumed to either both have forward, or both backward connections with the other regions, despite clear differences in the functional connectivity between the two regions. The connections between the BLA and prefrontal cortex were fixed in both directions, although comparison of forward and backward connections in each direction may have been beneficial. In future, effective connectivity studies of the cortico-limbic circuit prioritising use of the LFP and CMM_NMDA neural mass models over ERP and CMM models, would enable a broader range of anatomical models to be tested.

The use of separate DCM models across a range of frequencies was informed by previous work in the lab and reflects the limitations of DCM in fitting broadband spectral data (Moran et al., 2015). Despite the variation between the leading models across the different frequency ranges, the results largely replicated and were supported by the functional connectivity analysis supporting the validity of the approach. The ease of interpretation of the findings would be improved substantially if a single model could be used to fit the full range of spectral data, however, this was beyond the scope of this thesis.

5.4.7. Further work

The effective causality analysis presented in this chapter describes the effects of 5-HT_{2A} agonism on extrinsic connectivity facilitating comparison with the functional connectivity analysis in Chapter 4. The leading DCM models also contain a broader set of model parameters that may provide further mechanistic insights. Exploration of the wider parameterisation of the leading models was beyond the scope of this thesis, however can be achieved through reapplication of the hierarchical PEB analyses used to describe extrinsic connectivity to the rest of the parameter space. Comparison of 25I-induced changes in model

parameters in the high frequency range may yield further mechanistic insights into the generation of HFO. Comparison of 25I-induced changes across the leading low, middle, and high frequency range models may enable synthesis of shared mechanisms of 5-HT_{2A} action.

As discussed in Section 5.2, the effective connectivity analysis presented in this chapter did not attempt to model the cortico-striatal circuit using DCM due to the challenges in fitting the nucleus accumbens into the laminar architecture used in DCM. Within the limbic circuit of the basal ganglia, the nucleus accumbens can be considered as the analogous to the striatum in the motor circuit of the basal ganglia (see Figure 5.11) which has previously been modelled using DCM (Moran et al., 2011). Approaches to combine sources using different neural mass models have been developed, which allow specification of anatomical models combining the neural mass model of the basal ganglia with cortical neural mass models (van Wijk et al., 2018). At present these approaches are only described for some convolutional cortical models so the ability to fit HFO may be limited. Whilst modelling the nucleus accumbens with the basal ganglia neural mass model has face validity this approach has not previously been attempted and was beyond the scope of the current thesis.

Despite these challenges, existing findings in the literature suggest that extending the current work to the cortico-striatal circuit may be of interest. Using DCM on human fMRI data, LSD, LSD after pre-treatment with a 5-HT_{2A} antagonist, and placebo were compared in a double-blind randomised, controlled trial (Preller et al., 2019). The authors identified both 5-HT_{2A} dependent and 5-HT_{2A} independent changes in effective connectivity in cortico-striatal-thalamo-cortical network activity following LSD. In addition to highlighting an effect of 5-HT_{2A} agonism on the cortico-striatal circuit, this study also highlights the benefit of using more selective agonists at the 5-HT_{2A} receptor given that some of the changes induced by LSD were independent of 5-HT_{2A} activity.

Figure 5.11: Nucleus Accumbens as a functional analogue to striatum

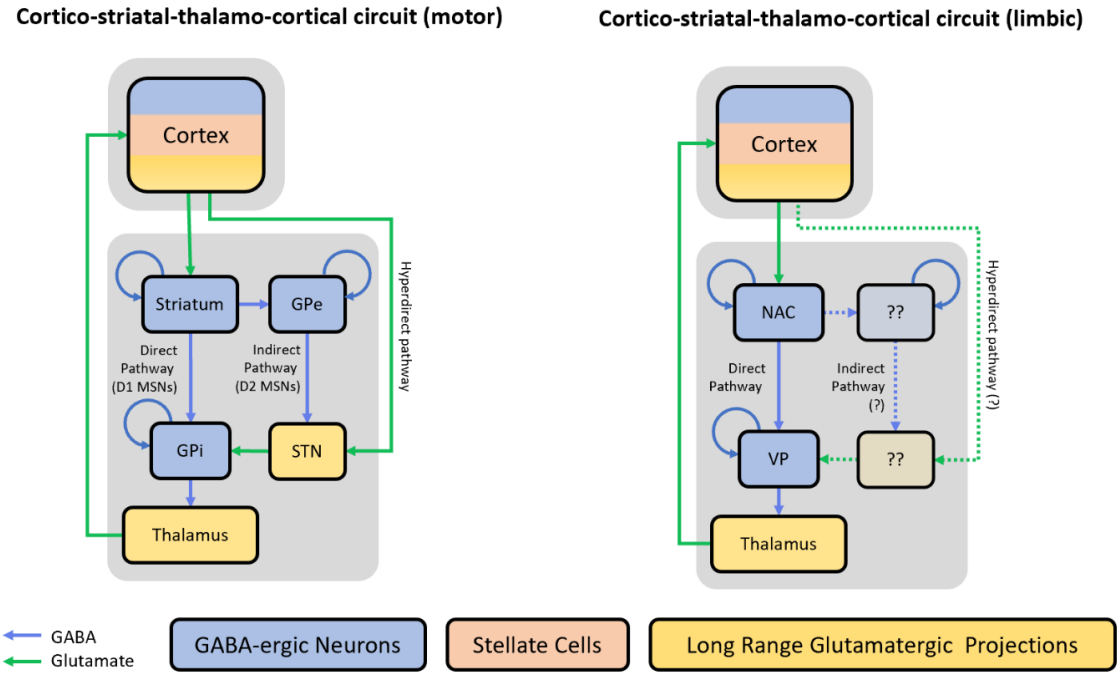

Comparison between architecture of the motor and limbic loops of the cortico-striatal-thalamo-cortical circuits. A DCM model of the motor circuit of has previously been described (Moran et al., 2011). NAC and striatum show functional similarity, however the direct and indirect pathways are ill-defined in the limbic circuit. For further discussion see indirect and direct pathways in decision making (Macpherson et al., 2014). VP, Ventral Pallidum; GPe, Globus pallidus externa; GPi, Globus pallidus interna; STN, Subthalamic nucleus.

Chapter 6. Discussion

6.1. Key findings

Despite limitations with respect to statistical power, preliminary conclusions about the effects of 5-HT_{2A} agonism on distributed network activity can be reasonably drawn, supported by the convergence of distinct analyses and consistency with findings reported in the wider literature. The spectral analysis presented in chapter 4 demonstrated that 5-HT_{2A} agonism induces HFO in the prefrontal cortex, with functional connectivity analyses supporting the NAC as the likely source of HFO in the cortico-striatal circuit. In the cortico-limbic circuit, functional connectivity analysis suggests that IL acts as the source for HFO, with the cortico-striatal data suggesting that IL is in turn driven by NAC.

Despite different methodologies and approaches, the functional connectivity and effective connectivity analyses of the cortico-limbic experiments converged on two key findings:

- Firstly, 25I results in increases in coupling, and top-down influence from the prefrontal cortex to the amygdala, a change that potentially has therapeutic implications in the treatment of anxiety and depressive disorders.
- Secondly, 25I results in suppression of cortico-hippocampal drive and disruption of the normal communication between these regions. This finding suggests similarities between the effects of 5-HT_{2A} agonists and the NMDA antagonist ketamine which may contribute to the psychotomimetic qualities of psychedelic drugs.

6.2. Further characterisation is needed of the pharmacokinetics and pharmacodynamics of 25I

Direct comparison of the findings in this thesis with the existing literature is complicated by the use of non-selective agonists in most of the published literature, and by variation in pharmacokinetics and pharmacodynamics of 5-HT_{2A} agonists. In human studies, the duration of subjective effects from intravenous DMT is less than 20 minutes with an immediate onset (Timmermann et al., 2019). In contrast, the duration of subjective effects from LSD is approximately 9-10 hours irrespective of the route of administration, with onset varying from immediate with intravenous administration to 45 minutes for oral administration (Passie et al., 2008). Other agents such as DOI have even longer durations with subjective effects from oral DOI reported to last up to 30 hours (Shulgin and Shulgin, 1990). The pharmacodynamics and pharmacokinetics of i.p. 25I in rats have not yet been established, although the changes in

spectral power described in Chapter 4 persisted at the end of recording sessions over 90 minutes post-injection. Characterisation of the dose-response, rate of onset and duration of drug effects following 25I should be performed alongside subsequent studies and could be assessed using automated measurement of the HTR (de la Fuente Revenga et al., 2019).

6.3. Appraisal of the analysis pipeline

In this thesis, I have established a pipeline for the characterisation of the effects of pharmacological agents on the behaviour, functional connectivity, and effective connectivity in freely behaving rats with chronically implanted LFP electrodes. The main limitation of the analysis pipeline developed over the course of this thesis stemmed from the limitations of the dataset available. Analysis and interpretation would have been simplified by combining the cortico-striatal and cortico-limbic recording sites into a single experiment with a greater number of animals. Due to the use of multiple significance testing and the requirement to use non-parametric statistics for the Granger causality analysis, larger sample sizes should be used in future studies.

6.3.1. Refinement of behavioural analysis

Throughout the analysis in Chapters 3, 4, and 5, changes in behaviour and neurophysiology were seen in both the 25I and control condition. The extent of changes in the control condition was unanticipated and reduced the power of the study to identify statistically significant behavioural changes. Changes in the control condition may be in response to the injection or reflect gradual changes (decreases) in arousal as the animals habituated to the arena. In human research the effects of psychedelics appear to be state variant; that is the same dose of a substance can result in either clinical improvements in mood, or fear and anxiety in an outside setting depending on the mental state at the time of ingestion and the setting in which the substance is used (Russ et al., 2019, Carhart-Harris et al., 2018b). Consideration of alternative routes of administration, and/or wireless recording of LFP in the home cage over the full duration of the 5-HT_{2A} agonist may be beneficial in future work.

Whilst the tracking data analysed in Chapter 3 provides some behavioural insights, the recent development of video-based automated open-source approaches to quantifying behaviour provide scope for considerably more nuanced analysis of behaviour. As part of the work relating to this thesis, I explored the use of DeepLabCut (Mathis et al., 2018) on sample video footage, however, I was unable to develop this approach with the experimental data as the original video footage was not available. Automated analysis of behaviour using high-speed

high-resolution video recorded with an infra-red camera would enable greater characterisation of behaviour and arousal and enable visualisation of the HTR as a measure of 5-HT_{2A} agonism (Halberstadt and Geyer, 2013). Once encoded, behavioural states of interest could be used to identify epochs for functional and effective connectivity analysis across predefined behavioural states.

6.3.2. Refinement of approaches to time series data

Neural activity is organised temporally and fluctuates as attention and cognitive processes shift, with dynamic changes in measures of functional connectivity forming the basis of resting state fMRI studies (Smith et al., 2013). Similar patterns of network activation and association are likely to be present across implanted electrode arrays, with the effects of pharmacological agents varying depending on the state of the network at a given time.

In the analyses presented in Chapters 4 and 5, the effect of 25I over time was described by discrete early and late post-drug periods. The functional connectivity analysis reported in Chapter 4 was effective over relatively short epochs (2-10 seconds) demonstrating scope to explore drug effects on functional connectivity as a continuous process. The PEB approach used in Chapter 5 can be used to describe linear changes in effective connectivity parameters with respect to time, however, linear models are unlikely to be adequate to describe the changes caused by 5-HT_{2A} agonism, given the combination of pharmacodynamics and pharmacokinetics, across multiple sites of action. Proof of concept in describing non-linear dynamics in effective connectivity has been developed by combining PEB analysis with temporal basis sets, however, this adds substantial complexity to computation (Van de Steen et al., 2019).

6.4. Future directions

The apparent similarities between the actions of ketamine and 5-HT_{2A} agonists suggest that a follow up study combining ketamine, 25I and control conditions in the same animals, with sufficient washout between sessions, would be beneficial to determine whether there are shared pharmacological mechanisms that underlie their action as rapid acting antidepressants. Similarly, given the persistent nature of antidepressant effects of 5-HT_{2A} agonists (Carhart-Harris et al., 2018) follow-up recording sessions following of the acute effects of drug would be beneficial in understanding the therapeutic mechanism of these drugs. The inclusion of a recording electrode in the olfactory bulb would be beneficial given evidence supporting this as a potential source of HFO downstream to NAC (Hunt et al., 2019).

Historically the common practice for this type of research was to use male rats, as used in this study. PET imaging data suggests variability in 5-HT_{2A} receptor binding between male and female healthy controls across a range of brain regions including medial prefrontal cortex (Soloff et al., 2010). In future studies the inclusion of male and female animals would therefore be beneficial to ensure findings are broadly translatable when considering implications for the treatment of disease in humans.

Since the experimental work used for these studies was conducted there have been significant advances in recording electrode technology for example the development of high density Neuropixel probes, enabling chronic recording of LFP and spike data from hundreds of recording sites along the length of the probe (Hong and Lieber, 2019). Integration of spike data from individual neurons may help to answer mechanistic questions relating to the generation of HFOs and provide insights into changes in coupling at the level of individual neurons alongside the insights of functional and effective connectivity at the level of neuronal populations. Data from individual neurons may also be beneficial in validating mechanistic hypotheses generated from the DCM models used in the analysis of effective causality.

6.5. Conclusions

The combination of approaches used in this thesis facilitated an in-depth description of the effects of 5-HT_{2A} agonists on network activity in freely behaving rats, identifying changes in cortico-limbic and cortico-striatal circuits. To inform and develop psychiatric drug development translation is required from animal models to human disease, with communication in both directions between human and animal researchers (Markou et al., 2009).

Translational studies are necessary to interpret the clinical relevance of HFO described in this thesis. Measurement of HFO in human prefrontal cortex following treatment with 5-HT_{2A} agonists and ketamine, and characterisation of the associations between HFO and the clinical response of depression, would be an important step towards understanding the clinical importance of HFO. MEG has recently been demonstrated to have the capability to record high frequency oscillations suggesting this would be feasible (Leiken et al., 2014). Likewise, pharmacological findings from human studies such as reduced coupling between prefrontal cortex and amygdala on fMRI (Siegle et al., 2007), can be described in animal models using the approaches in this thesis, increasing understanding of how correlated changes in BOLD signal relate to changes in neural oscillations or functional connectivity.

Computational approaches have shown significant promise in translational neuroscience (Flagel et al., 2019). Computational approaches may involve application of models with

shared features across human and animal data enabling comparison of the effects of interventions on parameters, or generate hypotheses that can in turn be tested in human or animal subjects (Flagel et al., 2019). The functional and effective connectivity analysis presented in this thesis showed convergence with findings from human MEG and fMRI studies of 5-HT_{2A} agonists, demonstrating the potential of these approaches to identify translational mechanistic insights into disease processes and treatments at network, cellular and synaptic-resolutions.

References

Adams, L. M. & Geyer, M. A. 1985. A proposed animal model for hallucinogens based on LSD's effects on patterns of exploration in rats. *Behav Neurosci,* 99 (5)**,** 881-900.

Adams, R. A., Stephan, K. E., Brown, H. R., Frith, C. D. & Friston, K. J. 2013. The computational anatomy of psychosis. *Frontiers in psychiatry,* 4 47-47.

Aertsen, A. & Preissl, H. 1991. Dynamics of activity and connectivity in physiological neuronal networks. *Nonlinear Dynamics and Neuronal Networks*.

Andersen, K. a. A., Carhart-Harris, R., Nutt, D. J. & Erritzoe, D. 2020. Therapeutic effects of classic serotonergic psychedelics: A systematic review of modern-era clinical studies. *Acta Psychiatr Scand*.

Appel, J. B., West, W. B. & Buggy, J. 2004. LSD, 5-HT (serotonin), and the evolution of a behavioral assay. *Neuroscience & Biobehavioral Reviews,* 27 (8)**,** 693-701.

Asgari, K., Body, S., Bak, V. K., Zhang, Z. Q., Rickard, J. F., Glennon, J. C., Fone, K. C., Bradshaw, C. M. & Szabadi, E. 2006. Effects of 5-HT2A receptor stimulation on the discrimination of durations by rats. *Behav Pharmacol,* 17 (1)**,** 51-9.

Bacqué-Cazenave, J., Bharatiya, R., Barrière, G., Delbecque, J.-P., Bouguiyoud, N., Di Giovanni, G., Cattaert, D. & De Deurwaerdère, P. 2020. Serotonin in Animal Cognition and Behavior. *International journal of molecular sciences,* 21 (5)**,** 1649.

Banks, S. J., Eddy, K. T., Angstadt, M., Nathan, P. J. & Phan, K. L. 2007. Amygdala–frontal connectivity during emotion regulation. *Social Cognitive and Affective Neuroscience,* 2 (4)**,** 303-312.

Barnes, N. M. & Sharp, T. 1999. A review of central 5-HT receptors and their function. *Neuropharmacology,* 38 (8)**,** 1083-152.

Barnett, L., Muthukumaraswamy, S. D., Carhart-Harris, R. L. & Seth, A. K. 2020. Decreased directed functional connectivity in the psychedelic state. *NeuroImage,* 209 116462.

Barnett, L. & Seth, A. K. 2011. Behaviour of Granger causality under filtering: Theoretical invariance and practical application. *Journal of Neuroscience Methods,* 201 (2)**,** 404-419.

Barnett, L. & Seth, A. K. 2014. The MVGC multivariate Granger causality toolbox: A new approach to Granger-causal inference. *Journal of Neuroscience Methods,* 223 50-68.

Bastos, A. M. & Schoffelen, J.-M. 2016. A Tutorial Review of Functional Connectivity Analysis Methods and Their Interpretational Pitfalls. *Frontiers in Systems Neuroscience,* 9 (175).

Bastos, A. M., Usrey, W. M., Adams, R. A., Mangun, G. R., Fries, P. & Friston, K. J. 2012. Canonical microcircuits for predictive coding. *Neuron,* 76 (4)**,** 695-711.

Beliveau, V., Ganz, M., Feng, L., Ozenne, B., Højgaard, L., Fisher, P. M., Svarer, C., Greve, D. N. & Knudsen, G. M. 2017. A High-Resolution In Vivo Atlas of the Human Brain's Serotonin System. *J Neurosci,* 37 (1)**,** 120-128.

Benjamini, Y. & Hochberg, Y. 1995. Controlling the False Discovery Rate: A Practical and Powerful Approach to Multiple Testing. *Journal of the Royal Statistical Society. Series B (Methodological),* 57 (1)**,** 289-300.

Benjamini, Y. & Yekutieli, D. 2001. The control of the false discovery rate in multiple testing under dependency. *Ann. Statist.,* 29 (4)**,** 1165-1188.

Berger, M., Gray, J. A. & Roth, B. L. 2009. The expanded biology of serotonin. *Annual review of medicine,* 60 355-366.

Bokil, P. M. H. 2008. *Observed Brain Dynamics,* New York, Oxford University Press.

Buchborn, T., Schröder, H., Dieterich, D. C., Grecksch, G. & Höllt, V. 2015. Tolerance to LSD and DOB induced shaking behaviour: Differential adaptations of frontocortical 5-HT2A and glutamate receptor binding sites. *Behavioural Brain Research,* 281 62-68.

Buzsáki, G. 2002. Theta oscillations in the hippocampus. *Neuron,* 33 (3)**,** 325-40.

Buzsáki, G., Anastassiou, C. A. & Koch, C. 2012. The origin of extracellular fields and currents--EEG, ECoG, LFP and spikes. *Nature reviews. Neuroscience,* 13 (6)**,** 407-420.

Buzsáki, G. & Wang, X. J. 2012. Mechanisms of gamma oscillations. *Annu Rev Neurosci,* 35 203-25.

Canal, C. E. & Morgan, D. 2012. Head-twitch response in rodents induced by the hallucinogen 2,5-dimethoxy-4-iodoamphetamine: a comprehensive history, a re-evaluation of mechanisms, and its utility as a model. *Drug testing and analysis,* 4 (7-8)**,** 556-576.

Carhart-Harris, R. L., Bolstridge, M., Day, C. M. J., Rucker, J., Watts, R., Erritzoe, D. E., Kaelen, M., Giribaldi, B., Bloomfield, M., Pilling, S., Rickard, J. A., Forbes, B., Feilding, A., Taylor, D., Curran, H. V. & Nutt, D. J. 2018a. Psilocybin with psychological support for treatment-resistant depression: six-month follow-up. *Psychopharmacology,* 235 (2)**,** 399-408.

Carhart-Harris, R. L., Bolstridge, M., Rucker, J., Day, C. M. J., Erritzoe, D., Kaelen, M., Bloomfield, M., Rickard, J. A., Forbes, B., Feilding, A., Taylor, D., Pilling, S., Curran, V. H. & Nutt, D. J. 2016a. Psilocybin with psychological support for treatment-resistant depression: an open-label feasibility study. *The Lancet Psychiatry,* 3 (7)**,** 619-627.

Carhart-Harris, R. L., Kaelen, M., Bolstridge, M., Williams, T. M., Williams, L. T., Underwood, R., Feilding, A. & Nutt, D. J. 2016b. The paradoxical psychological effects of lysergic acid diethylamide (LSD). *Psychological Medicine,* 46 (7)**,** 1379-1390.

Carhart-Harris, R. L., Muthukumaraswamy, S., Roseman, L., Kaelen, M., Droog, W., Murphy, K., Tagliazucchi, E., Schenberg, E. E., Nest, T., Orban, C., Leech, R., Williams, L. T., Williams, T. M., Bolstridge, M., Sessa, B., Mcgonigle, J., Sereno, M. I., Nichols, D., Hellyer, P. J., Hobden, P., Evans, J., Singh, K. D., Wise, R. G., Curran, H. V., Feilding, A. & Nutt, D. J. 2016c. Neural correlates of the LSD experience revealed by multimodal neuroimaging. *Proceedings of the National Academy of Sciences,* 201518377.

Carhart-Harris, R. L. & Nutt, D. J. 2017. Serotonin and brain function: a tale of two receptors. *Journal of psychopharmacology (Oxford, England),* 31 (9)**,** 1091-1120.

Carhart-Harris, R. L., Roseman, L., Haijen, E., Erritzoe, D., Watts, R., Branchi, I. & Kaelen, M. 2018b. Psychedelics and the essential importance of context. *J Psychopharmacol,* 32 (7)**,** 725-731.

Carola, V., D'olimpio, F., Brunamonti, E., Mangia, F. & Renzi, P. 2002. Evaluation of the elevated plus-maze and open-field tests for the assessment of anxiety-related behaviour in inbred mice. *Behavioural Brain Research,* 134 (1)**,** 49-57.

Celada, P., Puig, M. V., Díaz-Mataix, L. & Artigas, F. 2008. The hallucinogen DOI reduces low-frequency oscillations in rat prefrontal cortex: reversal by antipsychotic drugs. *Biol Psychiatry,* 64 (5)**,** 392-400.

Daunizeau, J., David, O. & Stephan, K. E. 2011. Dynamic causal modelling: A critical review of the biophysical and statistical foundations. *NeuroImage,* 58 (2)**,** 312-322.

David, O. & Friston, K. J. 2003. A neural mass model for MEG/EEG: coupling and neuronal dynamics. *Neuroimage,* 20 (3)**,** 1743-55.

David, O., Guillemain, I., Saillet, S., Reyt, S., Deransart, C., Segebarth, C. & Depaulis, A. 2008. Identifying Neural Drivers with Functional MRI: An Electrophysiological Validation. *PLOS Biology,* 6 (12)**,** e315.

Davis, A. K., Barrett, F. S., May, D. G., Cosimano, M. P., Sepeda, N. D., Johnson, M. W., Finan, P. H. & Griffiths, R. R. 2020. Effects of Psilocybin-Assisted Therapy on Major Depressive Disorder: A Randomized Clinical Trial. *JAMA Psychiatry*.

De La Fuente Revenga, M., Shin, J. M., Vohra, H. Z., Hideshima, K. S., Schneck, M., Poklis, J. L. & González-Maeso, J. 2019. Fully automated head-twitch detection system for the study of 5-HT(2A) receptor pharmacology in vivo. *Sci Rep,* 9 (1)**,** 14247.

Dilgen, J., Tejeda, H. A. & O'donnell, P. 2013. Amygdala inputs drive feedforward inhibition in the medial prefrontal cortex. *Journal of neurophysiology,* 110 (1)**,** 221-229.

Dimpfel, W., Spüler, M. & Nichols, D. E. 1989. Hallucinogenic and stimulatory amphetamine derivatives: fingerprinting DOM, DOI, DOB, MDMA, and MBDB by spectral analysis of brain field potentials in the freely moving rat (Tele-Stereo-EEG). *Psychopharmacology,* 98 (3)**,** 297-303.

Dolleman-Van Der Weel, M. J., Griffin, A. L., Ito, H. T., Shapiro, M. L., Witter, M. P., Vertes, R. P. & Allen, T. A. 2019. The nucleus reuniens of the thalamus sits at the nexus of a hippocampus and medial prefrontal cortex circuit enabling memory and behavior. *Learn Mem,* 26 (7)**,** 191-205.

Dong, M., Xia, L., Lu, M., Li, C., Xu, K. & Zhang, L. 2019. A failed top-down control from the prefrontal cortex to the amygdala in generalized anxiety disorder: Evidence from resting-state fMRI with Granger causality analysis. *Neurosci Lett,* 707 134314.

Ettrup, A., Da Cunha-Bang, S., Mcmahon, B., Lehel, S., Dyssegaard, A., Skibsted, A. W., Jørgensen, L. M., Hansen, M., Baandrup, A. O., Bache, S., Svarer, C., Kristensen, J. L., Gillings, N., Madsen, J. & Knudsen, G. M. 2014. Serotonin 2A receptor agonist binding in the human brain with [^{11}C]Cimbi-36. *J Cereb Blood Flow Metab,* 34 (7)**,** 1188-96.

Ettrup, A., Hansen, M., Santini, M. A., Paine, J., Gillings, N., Palner, M., Lehel, S., Herth, M. M., Madsen, J., Kristensen, J., Begtrup, M. & Knudsen, G. M. 2011. Radiosynthesis and in vivo evaluation of a series of substituted 11C-phenethylamines as 5-HT2A agonist PET tracers. *European Journal of Nuclear Medicine and Molecular Imaging,* 38 (4)**,** 681-693.

Everitt, B. J. & Robbins, T. W. 2016. Drug Addiction: Updating Actions to Habits to Compulsions Ten Years On. *Annual Review of Psychology,* 67 (1)**,** 23-50.

Felix-Ortiz, Ada c., Beyeler, A., Seo, C., Leppla, Christopher a., Wildes, C. P. & Tye, Kay m. 2013. BLA to vHPC Inputs Modulate Anxiety-Related Behaviors. *Neuron,* 79 (4)**,** 658-664.

Fitzgerald, P. J. & Watson, B. O. 2018. Gamma oscillations as a biomarker for major depression: an emerging topic. *Translational psychiatry,* 8 (1)**,** 177-177.

Flagel, S. B., Gordon, J. A. & Paulus, M. P. 2019. Editorial: bridging the gap with computational and translational psychopharmacology. *Psychopharmacology,* 236 (8)**,** 2291-2294.

Forsyth, L. H., Witton, J., Brown, J. T., Randall, A. D. & Jones, M. W. 2012. In Vitro and In Vivo Recording of Local Field Potential Oscillations in Mouse Hippocampus. *Curr Protoc Mouse Biol,* 2 (3)**,** 273-94.

Freidlin, B., Miao, W. & Gastwirth, J. L. 2003. On the Use of the Shapiro-Wilk Test in Two-Stage Adaptive Inference for Paired Data from Moderate to Very Heavy Tailed Distributions. *Biometrical Journal,* 45 (7)**,** 887-900.

Fries, P. 2009. Neuronal Gamma-Band Synchronization as a Fundamental Process in Cortical Computation. *Annual Review of Neuroscience,* 32 (1)**,** 209-224.

Friston, K., Brown, H. R., Siemerkus, J. & Stephan, K. E. 2016. The dysconnection hypothesis (2016). *Schizophrenia research,* 176 (2-3)**,** 83-94.

Friston, K., Moran, R. & Seth, A. K. 2013. Analysing connectivity with Granger causality and dynamic causal modelling. *Curr Opin Neurobiol,* 23 (2)**,** 172-8.

Friston, K. & Penny, W. 2011. Post hoc Bayesian model selection. *NeuroImage,* 56 (4)**,** 2089-2099.

Friston, K. J. 2011. Functional and effective connectivity: a review. *Brain Connect,* 1 (1)**,** 13-36.

Friston, K. J., Bastos, A., Litvak, V., Stephan, K. E., Fries, P. & Moran, R. J. 2012. DCM for complex-valued data: cross-spectra, coherence and phase-delays. *Neuroimage,* 59 (1)**,** 439-55.

Fujisawa, S. & Buzsáki, G. 2011. A 4 Hz oscillation adaptively synchronizes prefrontal, VTA, and hippocampal activities. *Neuron,* 72 (1)**,** 153-65.

Gabbott, P. L., Warner, T. A. & Busby, S. J. 2006. Amygdala input monosynaptically innervates parvalbumin immunoreactive local circuit neurons in rat medial prefrontal cortex. *Neuroscience,* 139 (3)**,** 1039-48.

Gardner, W. A. 1992. A unifying view of coherence in signal processing. *Signal Processing,* 29 (2)**,** 113-140.

Geiger, H. A., Wurst, M. G. & Daniels, R. N. 2018. DARK Classics in Chemical Neuroscience: Psilocybin. *ACS Chemical Neuroscience,* 9 (10)**,** 2438-2447.

Goda, S. A., Piasecka, J., Olszewski, M., Kasicki, S. & Hunt, M. J. 2013. Serotonergic hallucinogens differentially modify gamma and high frequency oscillations in the rat nucleus accumbens. *Psychopharmacology,* 228 (2)**,** 271-282.

Godsil, B. P., Kiss, J. P., Spedding, M. & Jay, T. M. 2013. The hippocampal-prefrontal pathway: the weak link in psychiatric disorders? *Eur Neuropsychopharmacol,* 23 (10)**,** 1165-81.

González-Maeso, J., Weisstaub, N. V., Zhou, M., Chan, P., Ivic, L., Ang, R., Lira, A., Bradley-Moore, M., Ge, Y., Zhou, Q., Sealfon, S. C. & Gingrich, J. A. 2007. Hallucinogens Recruit Specific Cortical 5-HT2A Receptor-Mediated Signaling Pathways to Affect Behavior. *Neuron,* 53 (3)**,** 439-452.

González-Maeso, J., Yuen, T., Ebersole, B. J., Wurmbach, E., Lira, A., Zhou, M., Weisstaub, N., Hen, R., Gingrich, J. A. & Sealfon, S. C. 2003. Transcriptome fingerprints distinguish hallucinogenic and nonhallucinogenic 5-hydroxytryptamine 2A receptor

agonist effects in mouse somatosensory cortex. *The Journal of neuroscience : the official journal of the Society for Neuroscience,* 23 (26)**,** 8836-8843.

Gould, T. D., Dao, D. T. & Kovacsics, C. E. 2009. The open field test. *Mood and anxiety related phenotypes in mice: Characterization using behavioral tests.* Totowa, NJ, US: Humana Press.

Granger, C. W. J. 1969. Investigating Causal Relations by Econometric Models and Cross-spectral Methods. *Econometrica,* 37 (3)**,** 424-438.

Halberstadt, A. L. & Geyer, M. A. 2013. Characterization of the head-twitch response induced by hallucinogens in mice: detection of the behavior based on the dynamics of head movement. *Psychopharmacology (Berl),* 227 (4)**,** 727-39.

Hanks, J. B. & González-Maeso, J. 2013. Animal models of serotonergic psychedelics. *ACS chemical neuroscience,* 4 (1)**,** 33-42.

Hansen, M., Phonekeo, K., Paine, J. S., Leth-Petersen, S., Begtrup, M., Bräuner-Osborne, H. & Kristensen, J. L. 2014. Synthesis and Structure–Activity Relationships of N-Benzyl Phenethylamines as 5-HT2A/2C Agonists. *ACS Chemical Neuroscience,* 5 (3)**,** 243-249.

Hawkins, M. F., Uzelac, S. M., Baumeister, A. A., Hearn, J. K., Broussard, J. I. & Guillot, T. S. 2002. Behavioral responses to stress following central and peripheral injection of the 5-HT(2) agonist DOI. *Pharmacol Biochem Behav,* 73 (3)**,** 537-44.

Heald, A. H., Stedman, M., Davies, M., Livingston, M., Taylor, D. & Gadsby, R. 2020. Antidepressant Prescribing in England: Patterns and Costs. *Prim Care Companion CNS Disord,* 22 (2).

Hong, G. & Lieber, C. M. 2019. Novel electrode technologies for neural recordings. *Nature Reviews Neuroscience,* 20 (6)**,** 330-345.

Hornung, J. P. 2003. The human raphe nuclei and the serotonergic system. *J Chem Neuroanat,* 26 (4)**,** 331-43.

Howe, T., Blockeel, A. J., Taylor, H., Jones, M. W., Bazhenov, M. & Malerba, P. 2020. NMDA receptors promote hippocampal sharp-wave ripples and the associated coactivity of CA1 pyramidal cells. *Hippocampus,* 30 (12)**,** 1356-1370.

Hsu, L. M., Liang, X., Gu, H., Brynildsen, J. K., Stark, J. A., Ash, J. A., Lin, C. P., Lu, H., Rapp, P. R., Stein, E. A. & Yang, Y. 2016. Constituents and functional implications of the rat default mode network. *Proc Natl Acad Sci U S A,* 113 (31)**,** E4541-7.

Hübner, C., Bosch, D., Gall, A., Lüthi, A. & Ehrlich, I. 2014. Ex vivo dissection of optogenetically activated mPFC and hippocampal inputs to neurons in the basolateral amygdala: implications for fear and emotional memory. *Front Behav Neurosci,* 8 64.

Hunt, M. J., Adams, N. E., Średniawa, W., Wójcik, D. K., Simon, A., Kasicki, S. & Whittington, M. A. 2019. The olfactory bulb is a source of high-frequency oscillations (130–180 Hz) associated with a subanesthetic dose of ketamine in rodents. *Neuropsychopharmacology,* 44 (2)**,** 435-442.

Hunt, M. J., Raynaud, B. & Garcia, R. 2006. Ketamine dose-dependently induces high-frequency oscillations in the nucleus accumbens in freely moving rats. *Biol Psychiatry,* 60 (11)**,** 1206-14.

Insausti, R., Herrero, M. T. & Witter, M. P. 1997. Entorhinal cortex of the rat: cytoarchitectonic subdivisions and the origin and distribution of cortical efferents. *Hippocampus,* 7 (2)**,** 146-83.

Ji, G. & Neugebauer, V. 2012. Modulation of medial prefrontal cortical activity using in vivo recordings and optogenetics. *Mol Brain,* 5 36.

Ji, G., Sun, H., Fu, Y., Li, Z., Pais-Vieira, M., Galhardo, V. & Neugebauer, V. 2010. Cognitive Impairment in Pain through Amygdala-Driven Prefrontal Cortical Deactivation. *The Journal of Neuroscience,* 30 (15)**,** 5451.

Kahan, J. & Foltynie, T. 2013. Understanding DCM: ten simple rules for the clinician. *Neuroimage,* 83 542-9.

Krebs-Thomson, K., Paulus, M. P. & Geyer, M. A. 1998. Effects of hallucinogens on locomotor and investigatory activity and patterns: influence of 5-HT2A and 5-HT2C receptors. *Neuropsychopharmacology,* 18 (5)**,** 339-51.

Krebs, K. M. & Geyer, M. A. 1994. Cross-tolerance studies of serotonin receptors involved in behavioral effects of LSD in rats. *Psychopharmacology,* 113 (3)**,** 429-437.

Kupferschmidt, D. A. & Gordon, J. A. 2018. The dynamics of disordered dialogue: Prefrontal, hippocampal and thalamic miscommunication underlying working memory deficits in schizophrenia. *Brain Neurosci Adv,* 2.

Kuś, R., Kamiński, M. & Blinowska, K. J. 2004. Determination of EEG activity propagation: pair-wise versus multichannel estimate. *IEEE Trans Biomed Eng,* 51 (9)**,** 1501-10.

Lambe, E. K. & Aghajanian, G. K. 2006. Hallucinogen-induced UP states in the brain slice of rat prefrontal cortex: role of glutamate spillover and NR2B-NMDA receptors. *Neuropsychopharmacology,* 31 (8)**,** 1682-9.

Lambe, E. K. & Aghajanian, G. K. 2007. Prefrontal cortical network activity: Opposite effects of psychedelic hallucinogens and D1/D5 dopamine receptor activation. *Neuroscience,* 145 (3)**,** 900-910.

Leamer, E. E. 1985. Vector autoregressions for causal inference? *Carnegie-Rochester Conference Series on Public Policy,* 22 255-304.

Leiken, K., Xiang, J., Zhang, F., Shi, J., Tang, L., Liu, H. & Wang, X. 2014. Magnetoencephalography detection of high-frequency oscillations in the developing brain. *Frontiers in human neuroscience,* 8 969-969.

Lewis, D. A., Hashimoto, T. & Volk, D. W. 2005. Cortical inhibitory neurons and schizophrenia. *Nat Rev Neurosci,* 6 (4)**,** 312-24.

Li, Z., Chen, Z., Fan, G., Li, A., Yuan, J. & Xu, T. 2018. Cell-Type-Specific Afferent Innervation of the Nucleus Accumbens Core and Shell. *Frontiers in Neuroanatomy,* 12 (84).

Likhtik, E., Stujenske, J. M., A Topiwala, M., Harris, A. Z. & Gordon, J. A. 2014. Prefrontal entrainment of amygdala activity signals safety in learned fear and innate anxiety. *Nature Neuroscience,* 17 (1)**,** 106-113.

Little, S. & Brown, P. 2014. The functional role of beta oscillations in Parkinson's disease. *Parkinsonism Relat Disord,* 20 Suppl 1 S44-8.

López-Giménez, J. F. & González-Maeso, J. 2018. Hallucinogens and Serotonin 5-HT(2A) Receptor-Mediated Signaling Pathways. *Current topics in behavioral neurosciences,* 36 45-73.

Macpherson, T., Morita, M. & Hikida, T. 2014. Striatal direct and indirect pathways control decision-making behavior. *Frontiers in Psychology,* 5 (1301).

Madsen, M. K., Fisher, P. M., Burmester, D., Dyssegaard, A., Stenbæk, D. S., Kristiansen, S., Johansen, S. S., Lehel, S., Linnet, K., Svarer, C., Erritzoe, D., Ozenne, B. & Knudsen, G. M. 2019. Psychedelic effects of psilocybin correlate with serotonin 2A receptor occupancy and plasma psilocin levels. *Neuropsychopharmacology,* 44 (7)**,** 1328-1334.

Marek, G. J. & Aghajanian, G. K. 1996. LSD and the phenethylamine hallucinogen DOI are potent partial agonists at 5-HT2A receptors on interneurons in rat piriform cortex. *J Pharmacol Exp Ther,* 278 (3)**,** 1373-82.

Markou, A., Chiamulera, C., Geyer, M. A., Tricklebank, M. & Steckler, T. 2009. Removing obstacles in neuroscience drug discovery: the future path for animal models. *Neuropsychopharmacology,* 34 (1)**,** 74-89.

Markowitz, J., Gillis, W., Beron, C., Neufeld, S., Robertson, K., Bhagat, N., Peterson, R., Peterson, E., Hyun, M., Linderman, S., Sabatini, B. & Datta, S. 2018. The Striatum Organizes 3D Behavior via Moment-to-Moment Action Selection. *Cell,* 174.

Marreiros, A. C., Kiebel, S. J., Daunizeau, J., Harrison, L. M. & Friston, K. J. 2009. Population dynamics under the Laplace assumption. *Neuroimage,* 44 (3)**,** 701-14.

Martin, E. I., Ressler, K. J., Binder, E. & Nemeroff, C. B. 2009. The neurobiology of anxiety disorders: brain imaging, genetics, and psychoneuroendocrinology. *The Psychiatric clinics of North America,* 32 (3)**,** 549-575.

Mathis, A., Mamidanna, P., Cury, K. M., Abe, T., Murthy, V. N., Mathis, M. W. & Bethge, M. 2018. DeepLabCut: markerless pose estimation of user-defined body parts with deep learning. *Nature Neuroscience,* 21 (9)**,** 1281-1289.

Mckenzie, S., Nitzan, N. & English, D. F. 2020. Mechanisms of neural organization and rhythmogenesis during hippocampal and cortical ripples. *Philosophical Transactions of the Royal Society B: Biological Sciences,* 375 (1799)**,** 20190237.

Mijnster, M. J., Raimundo, A. G., Koskuba, K., Klop, H., Docter, G. J., Groenewegen, H. J. & Voorn, P. 1997. Regional and cellular distribution of serotonin 5-hydroxytryptamine2a receptor mRNA in the nucleus accumbens, olfactory tubercle, and caudate putamen of the rat. *J Comp Neurol,* 389 (1)**,** 1-11.

Millan, M. J., Marin, P., Bockaert, J. & Mannoury La Cour, C. 2008. Signaling at G-protein-coupled serotonin receptors: recent advances and future research directions. *Trends in Pharmacological Sciences,* 29 (9)**,** 454-464.

Mitchell, D. J., Mcnaughton, N., Flanagan, D. & Kirk, I. J. 2008. Frontal-midline theta from the perspective of hippocampal "theta". *Prog Neurobiol,* 86 (3)**,** 156-85.

Mitra Lab. *Chronux Web Page* [Online]. Available: http://chronux.org/ [Accessed 28th September 2020].

Mochcovitch, M. D., Da Rocha Freire, R. C., Garcia, R. F. & Nardi, A. E. 2014. A systematic review of fMRI studies in generalized anxiety disorder: Evaluating its neural and cognitive basis. *Journal of Affective Disorders,* 167 336-342.

Montgomery, S. M., Betancur, M. I. & Buzsáki, G. 2009. Behavior-Dependent Coordination of Multiple Theta Dipoles in the Hippocampus. *The Journal of Neuroscience,* 29 (5)**,** 1381.

Moran, R., Pinotsis, D. A. & Friston, K. 2013. Neural masses and fields in dynamic causal modeling. *Front Comput Neurosci,* 7 57.

Moran, R. J., Jones, M. W., Blockeel, A. J., Adams, R. A., Stephan, K. E. & Friston, K. J. 2015. Losing control under ketamine: suppressed cortico-hippocampal drive following acute ketamine in rats. *Neuropsychopharmacology : official publication of the American College of Neuropsychopharmacology,* 40 (2)**,** 268-277.

Moran, R. J., Mallet, N., Litvak, V., Dolan, R. J., Magill, P. J., Friston, K. J. & Brown, P. 2011. Alterations in Brain Connectivity Underlying Beta Oscillations in Parkinsonism. *PLOS Computational Biology,* 7 (8)**,** e1002124.

Moreno, J. L., Holloway, T., Albizu, L., Sealfon, S. C. & González-Maeso, J. 2011. Metabotropic glutamate mGlu2 receptor is necessary for the pharmacological and behavioral effects induced by hallucinogenic 5-HT2A receptor agonists. *Neuroscience letters,* 493 (3)**,** 76-79.

Mueller, F., Musso, F., London, M., De Boer, P., Zacharias, N. & Winterer, G. 2018. Pharmacological fMRI: Effects of subanesthetic ketamine on resting-state functional connectivity in the default mode network, salience network, dorsal attention network and executive control network. *NeuroImage. Clinical,* 19 745-757.

Müller, F., Holze, F., Dolder, P., Ley, L., Vizeli, P., Soltermann, A., Liechti, M. E. & Borgwardt, S. 2020. MDMA-induced changes in within-network connectivity contradict the specificity of these alterations for the effects of serotonergic hallucinogens. *Neuropsychopharmacology*.

Muller, J. F., Mascagni, F. & Mcdonald, A. J. 2006. Pyramidal cells of the rat basolateral amygdala: synaptology and innervation by parvalbumin-immunoreactive interneurons. *The Journal of comparative neurology,* 494 (4)**,** 635-650.

Muthukumaraswamy, S. D., Carhart-Harris, R. L., Moran, R. J., Brookes, M. J., Williams, T. M., Errtizoe, D., Sessa, B., Papadopoulos, A., Bolstridge, M., Singh, K. D., Feilding, A., Friston, K. J. & Nutt, D. J. 2013. Broadband Cortical Desynchronization Underlies the Human Psychedelic State. *The Journal of Neuroscience,* 33 (38)**,** 15171-15183.

Muthuswamy, J. & Thakor, N. V. 1998. Spectral analysis methods for neurological signals. *J Neurosci Methods,* 83 (1)**,** 1-14.

Nic Dhonnchadha, B. A., Bourin, M. & Hascoët, M. 2003. Anxiolytic-like effects of 5-HT2 ligands on three mouse models of anxiety. *Behav Brain Res,* 140 (1-2)**,** 203-14.

Nichols, D. E. 2004. Hallucinogens. *Pharmacology & Therapeutics,* 101 (2)**,** 131-181.

Nugent, A. C., Ballard, E. D., Gould, T. D., Park, L. T., Moaddel, R., Brutsche, N. E. & Zarate, C. A., Jr. 2019. Ketamine has distinct electrophysiological and behavioral effects in depressed and healthy subjects. *Mol Psychiatry,* 24 (7)**,** 1040-1052.

Oostenveld, R., Fries, P., Maris, E. & Schoffelen, J.-M. 2011. FieldTrip: Open Source Software for Advanced Analysis of MEG, EEG, and Invasive Electrophysiological Data. *Computational Intelligence and Neuroscience,* 2011 156869.

Ouagazzal, A. M., Grottick, A. J., Moreau, J. L. & Higgins, G. A. 2001. Effect of LSD on Prepulse Inhibition and Spontaneous Behavior in the Rat: A Pharmacological Analysis and Comparison between Two Rat Strains. *Neuropsychopharmacology,* 25 (4)**,** 565-575.

Padilla-Coreano, N., Bolkan, S. S., Pierce, G. M., Blackman, D. R., Hardin, W. D., Garcia-Garcia, A. L., Spellman, T. J. & Gordon, J. A. 2016. Direct Ventral Hippocampal-

Prefrontal Input Is Required for Anxiety-Related Neural Activity and Behavior. *Neuron,* 89 (4)**,** 857-66.

Páleníček, T., Fujáková, M., Brunovský, M., Horáček, J., Gorman, I., Balíková, M., Rambousek, L., Syslová, K., Kačer, P., Zach, P., Bubeníková-Valešová, V., Tylš, F., Kubešová, A., Puskarčíková, J. & Höschl, C. 2013. Behavioral, neurochemical and pharmaco-EEG profiles of the psychedelic drug 4-bromo-2,5-dimethoxyphenethylamine (2C-B) in rats. *Psychopharmacology (Berl),* 225 (1)**,** 75-93.

Pallavicini, C., Vilas, M. G., Villarreal, M., Zamberlan, F., Muthukumaraswamy, S., Nutt, D., Carhart-Harris, R. & Tagliazucchi, E. 2019. Spectral signatures of serotonergic psychedelics and glutamatergic dissociatives. *Neuroimage,* 200 281-291.

Park, L. T., Falodun, T. B. & Zarate, C. A., Jr. 2019. Ketamine for Treatment-Resistant Mood Disorders. *Focus (Am Psychiatr Publ),* 17 (1)**,** 8-12.

Pasquini, L., Palhano-Fontes, F. & Araujo, D. B. 2020. Subacute effects of the psychedelic ayahuasca on the salience and default mode networks. *J Psychopharmacol,* 34 (6)**,** 623-635.

Passie, T., Halpern, J. H., Stichtenoth, D. O., Emrich, H. M. & Hintzen, A. 2008. The Pharmacology of Lysergic Acid Diethylamide: A Review. *CNS Neuroscience & Therapeutics,* 14 (4)**,** 295-314.

Paxinos, G. & Watson, C. 2007. *The Rat Brain in Stereotaxic Coordinates. ,* San Diego, Academic Press.

Penny, W. D., Stephan, K. E., Daunizeau, J., Rosa, M. J., Friston, K. J., Schofield, T. M. & Leff, A. P. 2010. Comparing Families of Dynamic Causal Models. *PLOS Computational Biology,* 6 (3)**,** e1000709.

Petri, G., Expert, P., Turkheimer, F., Carhart-Harris, R., Nutt, D., Hellyer, P. J. & Vaccarino, F. 2014. Homological scaffolds of brain functional networks. *J R Soc Interface,* 11 (101)**,** 20140873.

Pompeiano, M., Palacios, J. M. & Mengod, G. 1994. Distribution of the serotonin 5-HT2 receptor family mRNAs: comparison between 5-HT2A and 5-HT2C receptors. *Molecular Brain Research,* 23 (1)**,** 163-178.

Preller, K. H., Razi, A., Zeidman, P., Stämpfli, P., Friston, K. J. & Vollenweider, F. X. 2019. Effective connectivity changes in LSD-induced altered states of consciousness in humans. *Proceedings of the National Academy of Sciences,* 116 (7)**,** 2743-2748.

Prerau, M. J., Brown, R. E., Bianchi, M. T., Ellenbogen, J. M. & Purdon, P. L. 2016. Sleep Neurophysiological Dynamics Through the Lens of Multitaper Spectral Analysis. *Physiology,* 32 (1)**,** 60-92.

Puig, M. V., Celada, P., Díaz-Mataix, L. & Artigas, F. 2003. In vivo modulation of the activity of pyramidal neurons in the rat medial prefrontal cortex by 5-HT2A receptors: relationship to thalamocortical afferents. *Cereb Cortex,* 13 (8)**,** 870-82.

Puig, M. V., Watakabe, A., Ushimaru, M., Yamamori, T. & Kawaguchi, Y. 2010. Serotonin Modulates Fast-Spiking Interneuron and Synchronous Activity in the Rat Prefrontal Cortex through 5-HT_{1A} and 5-HT_{2A} Receptors. *The Journal of Neuroscience,* 30 (6)**,** 2211.

R Core Team 2019. R: A Language and Environment for Statistical Computing. Vienna, Austria: R Foundation for Statistical Computing.

Riba, J., Anderer, P., Jané, F., Saletu, B. & Barbanoj, M. J. 2004. Effects of the South American psychoactive beverage ayahuasca on regional brain electrical activity in humans: a functional neuroimaging study using low-resolution electromagnetic tomography. *Neuropsychobiology,* 50 (1)**,** 89-101.

Riba, J., Anderer, P., Morte, A., Urbano, G., Jané, F., Saletu, B. & Barbanoj, M. J. 2002. Topographic pharmaco-EEG mapping of the effects of the South American psychoactive beverage ayahuasca in healthy volunteers. *British journal of clinical pharmacology,* 53 (6)**,** 613-628.

Riga, M. S., Lladó-Pelfort, L., Artigas, F. & Celada, P. 2018. The serotonin hallucinogen 5-MeO-DMT alters cortico-thalamic activity in freely moving mice: Regionally-selective involvement of 5-HT(1A) and 5-HT(2A) receptors. *Neuropharmacology,* 142 219-230.

Root, D. H., Melendez, R. I., Zaborszky, L. & Napier, T. C. 2015. The ventral pallidum: Subregion-specific functional anatomy and roles in motivated behaviors. *Progress in neurobiology,* 130 29-70.

Rosa, M. J., Friston, K. & Penny, W. 2012. Post-hoc selection of dynamic causal models. *Journal of neuroscience methods,* 208 (1)**,** 66-78.

Rosenbaum, D. M., Rasmussen, S. G. F. & Kobilka, B. K. 2009. The structure and function of G-protein-coupled receptors. *Nature,* 459 (7245)**,** 356-363.

Rosenberg, J. R., Halliday, D. M., Breeze, P. & Conway, B. A. 1998. Identification of patterns of neuronal connectivity--partial spectra, partial coherence, and neuronal interactions. *J Neurosci Methods,* 83 (1)**,** 57-72.

Russ, S. L., Carhart-Harris, R. L., Maruyama, G. & Elliott, M. S. 2019. Replication and extension of a model predicting response to psilocybin. *Psychopharmacology (Berl),* 236 (11)**,** 3221-3230.

Sadzot, B., Baraban, J. M., Glennon, R. A., Lyon, R. A., Leonhardt, S., Jan, C. R. & Titeler, M. 1989. Hallucinogenic drug interactions at human brain 5-HT2 receptors: implications for treating LSD-induced hallucinogenesis. *Psychopharmacology (Berl),* 98 (4)**,** 495-9.

Scofield, M. D., Heinsbroek, J. A., Gipson, C. D., Kupchik, Y. M., Spencer, S., Smith, A. C. W., Roberts-Wolfe, D. & Kalivas, P. W. 2016. The Nucleus Accumbens: Mechanisms of Addiction across Drug Classes Reflect the Importance of Glutamate Homeostasis. *Pharmacological reviews,* 68 (3)**,** 816-871.

Seibenhener, M. L. & Wooten, M. C. 2015. Use of the Open Field Maze to measure locomotor and anxiety-like behavior in mice. *Journal of visualized experiments : JoVE,* (96)**,** e52434-e52434.

Seth, A. K., Barrett, A. B. & Barnett, L. 2015. Granger Causality Analysis in Neuroscience and Neuroimaging. *The Journal of Neuroscience,* 35 (8)**,** 3293.

Shoelson, B. 2020. createCirclesMask.m. MATLAB Central File Exchange.

Shulgin, A. & Shulgin, A. 1990. *Pihkal: A Chemical Love Story.,* Berkeley, CA, USA, Transform Press.

Siapas, A. G., Lubenov, E. V. & Wilson, M. A. 2005. Prefrontal Phase Locking to Hippocampal Theta Oscillations. *Neuron,* 46 (1)**,** 141-151.

Siegel, M., Donner, T. H. & Engel, A. K. 2012. Spectral fingerprints of large-scale neuronal interactions. *Nat Rev Neurosci,* 13 (2)**,** 121-34.

Siegle, G. J., Thompson, W., Carter, C. S., Steinhauer, S. R. & Thase, M. E. 2007. Increased amygdala and decreased dorsolateral prefrontal BOLD responses in unipolar depression: related and independent features. *Biol Psychiatry,* 61 (2)**,** 198-209.

Sirota, A., Montgomery, S., Fujisawa, S., Isomura, Y., Zugaro, M. & Buzsáki, G. 2008. Entrainment of Neocortical Neurons and Gamma Oscillations by the Hippocampal Theta Rhythm. *Neuron,* 60 (4)**,** 683-697.

Smith, S. M., Vidaurre, D., Beckmann, C. F., Glasser, M. F., Jenkinson, M., Miller, K. L., Nichols, T. E., Robinson, E. C., Salimi-Khorshidi, G., Woolrich, M. W., Barch, D. M., Uğurbil, K. & Van Essen, D. C. 2013. Functional connectomics from resting-state fMRI. *Trends in Cognitive Sciences,* 17 (12)**,** 666-682.

Soloff, P. H., Price, J. C., Mason, N. S., Becker, C. & Meltzer, C. C. 2010. Gender, personality, and serotonin-2A receptor binding in healthy subjects. *Psychiatry research,* 181 (1)**,** 77-84.

Stephan, K. E., Penny, W. D., Daunizeau, J., Moran, R. J. & Friston, K. J. 2009. Bayesian model selection for group studies. *NeuroImage,* 46 (4)**,** 1004-1017.

Stephan, K. E., Penny, W. D., Moran, R. J., Den Ouden, H. E. M., Daunizeau, J. & Friston, K. J. 2010. Ten simple rules for dynamic causal modeling. *NeuroImage,* 49 (4)**,** 3099-3109.

Studerus, E., Gamma, A. & Vollenweider, F. X. 2010. Psychometric Evaluation of the Altered States of Consciousness Rating Scale (OAV). *PLOS ONE,* 5 (8)**,** e12412.

Stujenske, J. M., Likhtik, E., Topiwala, M. A. & Gordon, J. A. 2014. Fear and safety engage competing patterns of theta-gamma coupling in the basolateral amygdala. *Neuron,* 83 (4)**,** 919-933.

Sullivan, L. C., Clarke, W. P. & Berg, K. A. 2015. Atypical antipsychotics and inverse agonism at 5-HT2 receptors. *Current pharmaceutical design,* 21 (26)**,** 3732-3738.

Swanson, L. W. 1981. A direct projection from Ammon's horn to prefrontal cortex in the rat. *Brain Res,* 217 (1)**,** 150-4.

Thierry, A. M., Gioanni, Y., Dégénétais, E. & Glowinski, J. 2000. Hippocampo-prefrontal cortex pathway: anatomical and electrophysiological characteristics. *Hippocampus,* 10 (4)**,** 411-9.

Thomson, D. J. 1982. Spectrum estimation and harmonic analysis. *Proceedings of the IEEE,* 70 (9)**,** 1055-1096.

Tierney, P. L., Dégenètais, E., Thierry, A.-M., Glowinski, J. & Gioanni, Y. 2004. Influence of the hippocampus on interneurons of the rat prefrontal cortex. *European Journal of Neuroscience,* 20 (2)**,** 514-524.

Timmermann, C., Roseman, L., Schartner, M., Milliere, R., Williams, L. T. J., Erritzoe, D., Muthukumaraswamy, S., Ashton, M., Bendrioua, A., Kaur, O., Turton, S., Nour, M. M., Day, C. M., Leech, R., Nutt, D. J. & Carhart-Harris, R. L. 2019. Neural correlates of the DMT experience assessed with multivariate EEG. *Sci Rep,* 9 (1)**,** 16324.

Timmermann, C., Spriggs, M. J., Kaelen, M., Leech, R., Nutt, D. J., Moran, R. J., Carhart-Harris, R. L. & Muthukumaraswamy, S. D. 2018. LSD modulates effective connectivity and neural adaptation mechanisms in an auditory oddball paradigm. *Neuropharmacology,* 142 251-262.

Unakafova, V. A. & Gail, A. 2019. Comparing Open-Source Toolboxes for Processing and Analysis of Spike and Local Field Potentials Data. *Frontiers in Neuroinformatics,* 13 (57).

Vahid-Ansari, F., Zhang, M., Zahrai, A. & Albert, P. R. 2019. Overcoming Resistance to Selective Serotonin Reuptake Inhibitors: Targeting Serotonin, Serotonin-1A Receptors and Adult Neuroplasticity. *Frontiers in neuroscience,* 13 404-404.

Van De Steen, F., Almgren, H., Razi, A., Friston, K. & Marinazzo, D. 2019. Dynamic causal modelling of fluctuating connectivity in resting-state EEG. *NeuroImage,* 189 476-484.

Van Wijk, B. C. M., Cagnan, H., Litvak, V., Kühn, A. A. & Friston, K. J. 2018. Generic dynamic causal modelling: An illustrative application to Parkinson's disease. *NeuroImage,* 181 818-830.

Vertes, R. P. 1991. A PHA-L analysis of ascending projections of the dorsal raphe nucleus in the rat. *J Comp Neurol,* 313 (4)**,** 643-68.

Vollenweider, F. X., Vollenweider-Scherpenhuyzen, M. F., Bäbler, A., Vogel, H. & Hell, D. 1998. Psilocybin induces schizophrenia-like psychosis in humans via a serotonin-2 agonist action. *Neuroreport,* 9 (17)**,** 3897-902.

Wang, L., Zhao, Y., Edmiston, E. K., Womer, F. Y., Zhang, R., Zhao, P., Jiang, X., Wu, F., Kong, L., Zhou, Y., Tang, Y. & Wei, S. 2020. Structural and Functional Abnormities of Amygdala and Prefrontal Cortex in Major Depressive Disorder With Suicide Attempts. *Frontiers in psychiatry,* 10 923-923.

Weber, E. T. & Andrade, R. 2010. Htr2a Gene and 5-HT(2A) Receptor Expression in the Cerebral Cortex Studied Using Genetically Modified Mice. *Frontiers in neuroscience,* 4 36.

Wilcoxon, F. 1945. Individual Comparisons by Ranking Methods. *Biometrics Bulletin,* 1 (6)**,** 80-83.

Willins, D. L., Deutch, A. Y. & Roth, B. L. 1997. Serotonin 5-HT2A receptors are expressed on pyramidal cells and interneurons in the rat cortex. *Synapse,* 27 (1)**,** 79-82.

Willins, D. L. & Meltzer, H. Y. 1997. Direct injection of 5-HT2A receptor agonists into the medial prefrontal cortex produces a head-twitch response in rats. *J Pharmacol Exp Ther,* 282 (2)**,** 699-706.

Wiltschko, A. B., Johnson, M. J., Iurilli, G., Peterson, R. E., Katon, J. M., Pashkovski, S. L., Abraira, V. E., Adams, R. P. & Datta, S. R. 2015. Mapping Sub-Second Structure in Mouse Behavior. *Neuron,* 88 (6)**,** 1121-1135.

Witter, M. P. 2007. The perforant path: projections from the entorhinal cortex to the dentate gyrus. *Prog Brain Res,* 163 43-61.

Wood, J., Kim, Y. & Moghaddam, B. 2012. Disruption of prefrontal cortex large scale neuronal activity by different classes of psychotomimetic drugs. *J Neurosci,* 32 (9)**,** 3022-31.

Wróbel, J., Średniawa, W., Jurkiewicz, G., Żygierewicz, J., Wójcik, D. K., Whittington, M. A. & Hunt, M. J. 2020. Nasal respiration is necessary for ketamine-dependent high frequency network oscillations and behavioral hyperactivity in rats. *Scientific reports,* 10 (1)**,** 18981-18981.

Zacharias, N., Musso, F., Müller, F., Lammers, F., Saleh, A., London, M., De Boer, P. & Winterer, G. 2020. Ketamine effects on default mode network activity and vigilance:

A randomized, placebo-controlled crossover simultaneous fMRI/EEG study. *Human Brain Mapping,* 41 (1)**,** 107-119.

Zeidman, P., Jafarian, A., Seghier, M. L., Litvak, V., Cagnan, H., Price, C. J. & Friston, K. J. 2019. A guide to group effective connectivity analysis, part 2: Second level analysis with PEB. *NeuroImage,* 200 12-25.